Spring 2016

Thorium-based mixed oxide fuel in a pressurized water reactor: A feasibility analysis with MCNP

Lucas Powelson Tucker

Department: Mining and Nuclear Engineering

Recommended Citation

Tucker, Lucas Powelson, "Thorium-based mixed oxide fuel in a pressurized water reactor: A feasibility analysis with MCNP" (2016). *Doctoral Dissertations*. 2492.
https://scholarsmine.mst.edu/doctoral_dissertations/2492

THORIUM-BASED MIXED OXIDE FUEL IN A PRESSURIZED WATER REACTOR: A FEASIBILITY ANALYSIS WITH MCNP

by

LUCAS POWELSON TUCKER

A DISSERTATION

Presented to the Graduate Faculty of the

MISSOURI UNIVERSITY OF SCIENCE AND TECHNOLOGY

In Partial Fulfillment of the Requirements for the Degree

DOCTOR OF PHILOSOPHY

in

NUCLEAR ENGINEERING

2016

Approved by:
Shoaib Usman, Advisor
Ayodeji Alajo
Carlos Castaño
Hyoung Koo Lee
G. Ivan Maldonado

PUBLICATION DISSERTATION OPTION

This dissertation consists of the following four articles, which either have been published, have been submitted for publication, or will be submitted for publication:

Paper I, entitled "Portable Spectroscopic Fast Neutron Probe and ^{3}He Detector Dead-time Measurements" and presented from page 10 to 29 in this dissertation, was submitted to *Progress in Nuclear Energy* on 23 January 2016 and is under review.

Paper II, entitled "Characterization of Best Candidate Isotopes for Burnup Analysis and Monitoring of Irradiated Fuel" and presented from page 30 to 64 in this dissertation, was published in *Annals of Nuclear Energy* Volume 69, pages 278-291, in 2014.

Paper III, entitled "Thorium-based Mixed Oxide Fuel in a Pressurized Water Reactor: A Beginning of Life Feasibility Analysis with MCNP" and presented from page 65 to 92 in this dissertation, was published in *Annals of Nuclear Energy* Volume 76, pages 323-334, in 2015.

Paper IV, entitled "Thorium-based Mixed Oxide Fuel in a Pressurized Water Reactor: A Burnup Analysis with MCNP" and presented from page 93 to 123 in this dissertation, will be submitted to *Annals of Nuclear Energy* for publication.

ABSTRACT

This dissertation investigates techniques for spent fuel monitoring, and assesses the feasibility of using a thorium-based mixed oxide fuel in a conventional pressurized water reactor for plutonium disposition. Both non-paralyzing and paralyzing dead-time calculations were performed for the Portable Spectroscopic Fast Neutron Probe (N-Probe), which can be used for spent fuel interrogation. Also, a Canberra ^{3}He neutron detector's dead-time was estimated using a combination of subcritical assembly measurements and MCNP simulations. Next, a multitude of fission products were identified as candidates for burnup and spent fuel analysis of irradiated mixed oxide fuel. The best isotopes for these applications were identified by investigating half-life, photon energy, fission yield, branching ratios, production modes, thermal neutron absorption cross section and fuel matrix diffusivity. ^{132}I and ^{97}Nb were identified as good candidates for MOX fuel on-line burnup analysis. In the second, and most important, part of this work, the feasibility of utilizing ThMOX fuel in a pressurized water reactor (PWR) was first examined under steady-state, beginning of life conditions. Using a three-dimensional MCNP model of a Westinghouse-type 17x17 PWR, several fuel compositions and configurations of a one-third ThMOX core were compared to a 100% UO_2 core. A blanket-type arrangement of 5.5 wt% PuO_2 was determined to be the best candidate for further analysis. Next, the safety of the ThMOX configuration was evaluated through three cycles of burnup at several using the following metrics: axial and radial nuclear hot channel factors, moderator and fuel temperature coefficients, delayed neutron fraction, and shutdown margin. Additionally, the performance of the ThMOX configuration was assessed by tracking cycle length, plutonium destroyed, and fission product poison concentration.

ACKNOWLEDGMENTS

I could not have completed this project without the tremendous support I received from faculty, staff, family, and friends. My advisor, Dr. Shoaib Usman, guided me through the process of choosing a project, executing it, presenting it, and staying funded. His help was invaluable.

I also need to thank Dr. Ayodeji Alajo and Dr. Ivan Maldonado, whose insights added depth and breadth to my results. And the remaining members of my thesis committee, Dr. Hyoung Lee and Dr. Carlos H. Castaño, also deserve thanks for their interest. Dr. Arvind Kumar, the former chair of the Nuclear Engineering Department, and after him, Dr. Lee, were instrumental in maintaining support for me and my project with teaching and research assistantships throughout my many years at Missouri S&T. The Missouri University of Science and Technology Reactor staff also must be acknowledged for their contribution. Bill Bonzer, the reactor manager, and Craig Reisner, the assistant reactor manager helped complete the N-Probe detector dead time measurements. I must acknowledge the sources of my funding: the U.S. Nuclear Regulatory Commission and the Missouri University of Science and Technology Chancellor’s Fellowship.

My friends and family have also contributed a great deal. Dr. Tayfun Akyurek was my frequent collaborator. Without him, the first two papers in this dissertation would not exist. I have shared many late night discussions and pots of coffee with Dr. Edwin Grant and Dr. Chrystian Posada, and I appreciated their encouragement, assistance, and opinions. After Dr. Grant and Dr. Posada graduated and moved on, a new crop of graduate students moved in to Fulton 230 with me. Ashish Avachat, Manish Sharma, and Edward Norris made my last years in Rolla much more enjoyable.

Last, and far from least, I thank my family. My wife, Erica, encouraged, listened, edited, typed, and provided the love and companionship I needed to complete my doctorate. Her contribution to this work is greater than I have words for. I can only imagine how much I’ll enjoy spending the rest of my life with her. I also owe her an apology (she knows why). My parents, Tim and Dr. Stephanie Powelson, provided a place for Erica and I to live while I completed my dissertation. They have supported me in every endeavor I have undertaken throughout my life, and I would have accomplished very little without them.

TABLE OF CONTENTS

SECTION

LIST OF ILLUSTRATIONS

PAPER I | Page

PAPER III

PAPER IV

LIST OF TABLES

PAPER I Page

PAPER II

PAPER III

PAPER IV

SECTION

1. INTRODUCTION

1.1 SPENT FUEL INTERROGATION USING PHOTONS AND NEUTRONS

Non-destructive analysis (NDA) techniques have long been used for monitoring spent uranium dioxide (UO_2) fuel. There are two groups of NDA techniques available: passive techniques measure delayed neutrons and gamma rays emitted after radioactive decay, while active techniques interrogate fuel by first bombarding it with a neutron source and then monitoring gamma and/or neutron emissions [1]. With the resurgence of interest in mixed oxide (MOX) in the United States, NDA techniques for monitoring spent MOX fuel need to be investigated.

Commercial nuclear fuel reprocessing was banned by the United States government, interrupting the U.S. reprocessing industry between 1977 and 1981, but France embraced reprocessing technology and incorporated mixed oxide (MOX) fuel into their nuclear fuel cycle. France has demonstrated that MOX fuel can be integrated into a Uranium fueled core without risking the safety of the plant or the proliferation of nuclear weapons. Recently, the U.S. nuclear power industry has been reconsidering MOX fuel. The successful disposition of Russian highly enriched uranium through the Megatons to Megawatts program has encouraged interest in a similar program for plutonium disposition in MOX fuel [2]. Therefore, better tools and techniques are necessary for burnup analysis and spent fuel monitoring of MOX fuel.

Using the NDA technique of passive gamma measurement, photons emitted by irradiated fuel assemblies can be analyzed to determine parameters such as burnup, cooling time, and irradiation history [3]. Willman et al., have discriminated MOX fuel from LEU fuel using ^{134}Cs, ^{137}Cs, and ^{154}Eu isotopes as cooling time and irradiation history indicators [4]. Dennis and Usman reported on ^{106}Ru as another potential burnup indicator [5].

Another NDA technique for spent fuel interrogation is neutron measurement. When ^{238}U is exposed to substantial neutron fluence (as with reactor fuel), ^{244}Cm is produced. Spontaneous fission of ^{244}Cm provides a source of delayed neutrons. Since the half-life of ^{244}Cm is 18.1 years – much longer than the amount of time fuel spends in a power reactor

– neutron intensity from ^{244}Cm can be used as a measure of burnup [6]. However, this technique is highly sensitive to cooling time, and initial enrichment.

Destructive techniques, such as chemical assay with a mass spectrometer, have historically been applied to determine isotopic composition of spent nuclear fuel. But these techniques require fuel sample destruction and can take a long time for sample analysis and results [7].

The Missouri University of Science and Technology research reactor (MSTR) is a pool-type reactor licensed by the NRC to operate up to 200 kW thermal power. The research reactor was the first nuclear reactor in Missouri and its core contains low enriched uranium (LEU) fuel. Facilities at the reactor allow for non-destructive burnup analysis and discrimination of fuel elements based on plutonium and uranium content using gamma and delayed neutron measurements. All radiation measurements need to be corrected using either non-paralyzing dead-time or paralyzing dead-time model depending on detector behavior.

1.2 THORIUM AS A NUCLEAR FUEL

Thorium represents a vast, largely untapped source of nuclear energy. Its abundance in the earth's crust is roughly three times greater than uranium [8]. Though ^{232}Th – the only naturally occurring isotope of thorium – is not fissile, it is fertile. After absorbing a neutron to become ^{233}Th and decaying to ^{233}Pa, it ultimately decays to ^{233}U [9]. Thorium-based fuels offer several potential advantages over uranium fuels: higher fissile conversion rate, higher thermal fission factor (η), lower capture-to-fission ratio, low actinide production, plutonium reduction, chemical stability, proliferation resistance [10, 11, 12, 13]. Because of these advantages, several methods for utilizing thorium fuels have been explored.

Most thorium utilization schemes require the development of advanced reactor designs. In a molten salt reactor (MSR) thorium and uranium fluorides are dissolved with the fluorides of beryllium and lithium [14]. MSRs offer some distinct advantages: they have a strongly negative temperature coefficient and allow for online refueling [14]. Also, two MSRs were designed, built, and operated at Oak Ridge National Laboratory, proving the concept and providing valuable experimental data [15, 16].

High temperature gas cooled reactors (HTGRs) are another option for thorium utilization. HTGRs would use TRISO fuel composed of pellets of thorium oxide or carbide blended with pellets of uranium oxide or carbide and coated with several layers of carbon and silicon carbide; the TRISO particles are combined in a graphite matrix and formed into either prisms or pebbles 10. Several countries (Germany, Japan, the Russian Federation, the United Kingdom, and the United States) have built HTGRs and loaded them with thorium fuel 10; and Tsinghua University in China is currently designing a 500 MW(th) pebble bed reactor demonstration plant [17]. HTGRs could be adapted to several fuel cycles without modification of the core or plant, but several technical hurdles remain before the technology is commercially viable 10.

An accelerator driven system is a unique reactor design in which a proton accelerator is used to produce enough spallation neutrons to bring an otherwise subcritical core to criticality 12. Such a system would use only natural uranium and thorium fuels, eliminating the need for enrichment technology, and reducing proliferation concerns, while also achieving high burnup [18]. India has been pursuing this technology, but the design is still in the conceptual stages, and the amount of power required to operate the accelerator casts doubt on the economic viability of such a system [18, 13].

Perhaps the most expedient scheme for exploiting the world's thorium resources is incorporating it into the current reactor fuel supply. Numerous publications have demonstrated a number of ways thorium could enhance the operation of boiling water reactors (BWRs), pressurized water reactors (PWRs), and heavy water reactors (HWRs) [10, 11, 19, 20, 21].

Thor Energy, a Norwegian company, is developing and testing thorium-plutonium BWR fuel pellets and assemblies for plutonium destruction [22, 23]. Xu, Downar, Takahashi, and Rohatgi are also studying the potential for plutonium disposition in BWRs [24] as are Mac Donald and Kazimi [25]. Francois et al. have investigated replacing all of the uranium fuel in a BWR with a thorium-uranium fuel blend [26].

Similar research on Th-Pu and Th-U fuels has been conducted for PWRs as well. Shwageraus, Hejzlar, and Kazimi have investigated the use of Th-Pu fuel in PWRs for both the destruction of plutonium [27] and improved economics [28]. Bjork et al. studied the use of Th-Pu fuel for extending the operating cycle of a PWR [29]. Trellue, Bathke, and

Sadasivan have used MCNP and MCNPX to compare the reactivity safety characteristics and Pu destruction capabilities of conventional MOX fuel to those of Th-MOX fuel [30]. Their work is complemented by that of Tsige-Tamirat, who also used Monte Carlo techniques to study the effect of Th-MOX fuel on a PWR's reactivity safety characteristics [31]. Burnup analyses of Th-MOX fuel for Pu disposition in PWRs have been performed by others: Fridman and Kliem [32].

Research on thorium utilization in HWRs has focused on both incorporating thorium rods into existing CANDU reactors [33], and, in India, developing advanced heavy water reactors specifically designed to burn thorium fuel [34].

1.3 RESEARCH OBJECTIVES

The primary objective of this work was to investigate the feasibility of incorporating a Th-Pu MOX fuel into the fuel supply of a conventional PWR for plutonium disposition. In pursuit of this objective, it was helpful to identify the best candidate isotopes for online burnup analysis and spent fuel monitoring of MOX fuel, and develop a non-destructive technique for discriminating plutonium and uranium. Therefore, the following tasks were accomplished:

Investigate the half-lives, decay photon energies, fission yields, branching ratios, production modes, thermal neutron absorption cross sections, and fuel matrix diffusivities of fission products to determine the best isotopes for online burnup analysis, spent fuel monitoring, and historical fuel monitoring of MOX fuel.

Use non-destructive techniques to interrogate the MSTR's spent fuel elements and calculate the uranium fuel burnup values. Record fast delayed neutron energy spectra for spent and fresh fuel elements. Measure delayed neutron emission rates to calculate plutonium conversion.

Use MCNP to model a conventional UO_2-fueled PWR at beginning of life. Identify the ThMOX fuel configuration which best matches the neutronic characteristics of the conventional UO_2-fueled PWR configuration. Simulate three cycles of burnup for both configurations. Compare the ThMOX configuration to the UO_2 configuration using the following safety metrics: axial and radial nuclear hot channel factor, moderator and fuel temperature coefficient, delayed neutron fraction, fission product poison concentration, and shutdown margin. Assess the plutonium destruction capability of the ThMOX configuration.

1.4 DISSERTATION ORGANIZATION

This dissertation is organized into three sections: the first section is an introduction to the areas under investigation; the second section is comprised of four papers which either have been published, have been submitted for publication, or will be submitted for publication; the third section summarizes the conclusions drawn from the papers presented in the second section and proposes future work.

In Paper I, both non-paralyzing and paralyzing dead-time calculations were obtained for a fast neutron detector used for spent fuel interrogations. The dead-time for another neutron detector (^{3}He) was also calculated using measurements collected in a subcritical assembly. An MCNP model of the subcritical assembly experiment was developed for comparison.

In Paper II, a multitude of fission products identified as candidates for burnup and spent fuel analysis were scrutinized for their suitability. From this list of candidates, the best isotopes for analysis were identified by investigating half-life, fission yield, branching ratios, production modes, thermal neutron absorption cross section and fuel matrix diffusivity.

In Paper III, the feasibility of utilizing ThMOX fuel in a pressurized water reactor was examined under steady-state, beginning of life conditions. With a three-dimensional MCNP model of a Westinghouse-type 17x17 PWR, many possibilities for replacing one-third of the UO_2 assemblies with ThMOX assemblies were considered. The excess reactivity, critical boron concentration, and centerline axial and radial flux profiles for several configurations and compositions of a one-third ThMOX core were compared to a 100% UO_2 core. A blanket-type arrangement of 5.5 wt% PuO_2 was determined to be the best candidate for further analysis. Therefore, this configuration was compared to a 100% UO_2 core using the following parameters: delayed neutron fraction, temperature coefficient, shutdown margin, and axial and radial nuclear hot channel factors.

In Paper IV, a burnup analysis was performed using the UO_2 configuration and the ThMOX configuration identified and examined in Paper III. The safety of the ThMOX configuration was compared to that of the UO_2 configuration at several time steps of interest within each cycle (beginning of cycle, peak excess reactivity of cycle, and end of cycle) with the following metrics: axial and radial nuclear hot channel factors, moderator and fuel temperature coefficients, delayed neutron fraction, and shutdown margin. Additionally, the performance of the ThMOX configuration was assessed by tracking cycle lengths, the amount of plutonium destroyed, and fission product poison concentration.

REFERENCES

[1] T. Akyurek et al. “Characterization of Best Candidate Isotopes for Burnup Analysis and Monitoring of Irradiated Fuel” Annals of Nuclear Energy, 69, 278-291. 2014.

[2] United States Enrichment Corporation. “Megatons to Megawatts Program” http://www.usec.com/news/megatons-megawatts-program-recycles-450-metric-tons-weapons-grade-uranium-commercial-nuclear-fu, accessed on 13 April, 2013, created on 9 July 2012.

[3] A. Håkansson, et al. “Results of spent-fuel NDA with HRGS” Proceedings of the 15th Annual Esarda Meeting. Rome, Italy. 1993.

[4] C. Willman, et al. “A nondestructive method for discriminating MOX fuel from LEU fuel for safeguards purpose” Annals of Nuclear Energy, 33, 766-773. 2006.

[5] M.L. Dennis, S. Usman. “Feasibility of ^{106}Ru peak measurement for MOX fuel burnup analysis” Nuclear Engineering and Design, 240, 3687-3696. 2010.

[6] K.A. Jordan, G. Perret. “A delayed neutron technique for measuring induced fission rates in fresh and burnt LWR fuel” Nuclear Instruments and Methods in Physics Research A, 634, 91-100. 2011.

[7] K. Inoue et al. “Burnup determination of Nuclear Fuel” Mass Spectroscopy, 17, 830-842. 1969.

[8] B.S. Van Gosen, V.S. Gillerman, T.J. Armbrustmacher. “Thorium Deposits of the United States—Energy Resources for the Future?” U.S. Geological Survey Circular 1336. 2009.

[9] E.M. Baum, H.D. Knox, T.R. Miller. “Nuclides and Isotopes: Chart of Nuclides, 16th Ed.” Lockheed Martin Distribution Services. 2002.

[10] F. Sokolov, K. Fukuda, H.P. Nawada. “Thorium Fuel Cycle – Potential Benefits and Challenges” IAEA-TECDOC-1450. IAEA. Vienna, 2005.

[11] “Role of Thorium to Supplement Fuel Cycles of Future Nuclear Energy Systems” IAEA Nuclear Energy Series No. NF-T-2.4. IAEA. Vienna, 2012.

[12] S. Peggs, W. Horak, T. Roser, et al. “Thorium Energy Futures” Proceedings of IPAC2012. New Orleans, 2012.

[13] K. Hesketh, A. Worrall. “The Thorium Fuel Cycle: An independent assessment by the UK National Nuclear Laboratory” National Nuclear Laboratory Position Paper. 2010.

[14] J.A. Lane “Fluid Fuel Reactors” Addison-Wesley Pub. Co. 1958.

[15] P.N. Haubenreich, J.R. Engel. “Experience with the Molten-Salt Reactor Experiment” Nuclear Applications and Technology. 1970.

[16] D.E. Holcomb, G.F. Flanagan, B.W. Patton, J.C. Gehin, R.L. Howard, T.J. Harrison, “Fast Spectrum Molten Salt Reactor Options” ORNL Report ORNL/TM-2011/105. 2011.

[17] Zuoyi Zhang, Zongxin Wu, Dazhong Wang, Yuanhui Xu, Yuliang Sun, Fu Li, Yujie Dong. “Current Status and Technical Description of Chinese 2 x 250 MWth HTR-PM Demonstration Plant” Nuclear Engineering and Design, 239, 1212-1219. July 2009.

[18] S. Banerjee. “Towards a Sustainable Nuclear Energy Future” 35th World Nuclear Association Symposium. London, 2010.

[19] P. Bromley, et al. “LWR-Based Transmutation of Nuclear Waste An Evaluation of Feasibility of Light Water Reactor (LWR) Based Actinide Transmutation Concepts-Thorium-Based Fuel Cycle Options” BNL-AAA-2002-001. 2002.

[20] K.D. Weaver, J.S. Herring. “Performance of Thorium-Based Mixed Oxide Fuels for the Consumption of Plutonium in Current and Advanced Reactors” Nucl. Tech., 143, 22-36. 2002.

[21] M. Todosow, G. Raitses. “Thorium Based Fuel Cycle Options for PWRs” Proceedings of ICAPP ’10, 1891-1900. June 13-17, 2010.

[22] K.I. Bjork. “A BWR Fuel Assembly Design for Efficient Use of Plutonium in Thorium-Plutonium Fuel” Progress in Nuclear Energy, 65, 56-63. 2013.

[23] K.I. Bjork, V. Fhager, C. Demaziere. “Comparison of Thorium-Based Fuels with Different Fissile Components in Existing Boiling Water Reactors” Progress in Nuclear Energy, 53, 618-625. 2011.

[24] Yunlin Xu, T.J. Downar, H. Takahashi, U.S. Rohatgi. “Neutronics Design and Fuel Cycle Analysis of a High Conversion BWR with Pu-Th Fuel” ICAPP. Florida, 2002.

[25] P. Mac Donald, M.S. Kazimi. “Advanced Proliferation Resistant, Lower Cost, Uranium-Thorium Dioxide Fuels for Light Water Reactors” NERI Annual Report, INEEL/EXT-2000-01217. 2000.

[26] J.L. Francois, A. Nuñez-Carrera, G. Espinosa-Paredes, C. Martin-del-Campo. “Design of a Boiling Water Reactor Equilibrium Core Using Thorium-Uranium Fuel” Americas Nuclear Energy Sumposium 2004. Miami Beach, FL, 2004.

[27] E. Shwageraus, P. Hejzlar, M.S. Kazimi. “Use of Thorium for Transmutation of Plutonium and Minor Actinides in PWRs” Nucl. Tech., 147, 53-68. 2004.

[28] E. Shwageraus, P. Hejzlar, M.J. Driscoll, M.S. Kazimi. “Optimization of Micro-Heterogeneous Uranium-Thorium Dioxide PWR Fuels for Economics and Enhanced Proliferation Resistance”, MIT-NFC-TR-046, MIT, Nucl. Eng. Dep, 2002.

[29] K.I. Bjork, C.W. Lau, H. Nylen, U. Sandberg. “Study of Thorium-Plutonium Fuel for Possible Operating Cycle Extension in PWRs” Science and Technology of Nuclear Installations. 2013.

[30] H.R. Trellue, C.G. Bathke, P. Sadasivan. “Neutronics and Material Attractiveness for PWR Thorium Systems Using Monte Carlo Techniques” Progress in Nuclear Energy, 53, 698-707. 2011.

[31] H. Tsige-Tamirat. “Neutronics Assessment of the Use of Thorium Fuels in Current Pressurized Water Reactors” Progress in Nuclear Energy, 53, 717-721. 2011.

[32] E. Fridman, S. Kliem. “Pu Recycling in a full Th-MOX PWR Core. Part I: Steady State Analysis” Nucl. Eng. and Design, 241, 193-202. 2011.

[33] P.G. Boczar, G.R. Dyck, P.S.W. Chan, D.B. Buss. “Recent Advances in Thorium Fuel Cycles for CANDU Reactors” Thorium Fuel Utilization: Options and Trends, IAEA-TECDOC-1319, 104-122. IAEA, Vienna, 2002.

[34] R.K. Sinha, A. Kakodar. “Design and Development of the AHWR – the Indain Thorium Fuelled Innovative Nuclear Reactor” Nucl. Eng. and Design, 236, 683-700. 2006.

PAPER

I. PORTABLE SPECTROSCOPIC FAST NEUTRON PROBE AND ^{3}HE DETECTOR DEAD-TIME MESUREMENTS

T. Akyurek[a, b,1], L. P. Tucker[b], X. Liu[b], S. Usman[b]

[a] Department of Physics, Faculty of Art and Science, Marmara University,
34722, Kadikoy, Istanbul, TURKEY

[b] Department of Mining and Nuclear Engineering, Missouri University of Science &
Technology, Rolla, MO, 65401, USA

Abstract

This paper presents dead-time calculations for the Portable Spectroscopic Fast Neutron Probe (N-Probe) using a combination of the attenuation law, MCNP (Monte Carlo N-particle Code) simulations and the assumption of ideal paralyzing and non-paralyzing dead-time models. The N-Probe contains an NE-213 liquid scintillator detector and a spherical ^{3}He detector. For the fast neutron probe, non-paralyzing dead-time values were higher than paralyzing dead-time values, as expected. Paralyzing dead-time was calculated to be 37.6 µs and non-paralyzing dead-time was calculated to be 43.7 µs for the N-Probe liquid scintillator detector. A Canberra ^{3}He neutron detector (0.5NH1/1K) dead-time value was also estimated using a combination of subcritical assembly measurements and MCNP simulations. The paralyzing dead-time was estimated to be 14.5 µs, and the non-paralyzing dead-time was estimated to be 16.4 µs for ^{3}He gas filled detector. These results are consistent with the dead-time values reported for helium detectors.

---

[1] Marmara Üniversitesi Fen Edebiyat Fakültesi Fizik Bolumu, Göztepe Kampüsü, Istanbul, TURKEY, 34722, Email: tayfun.akyurek@marmara.edu.tr, Phone: +90 216 345 1186- Ext:1175

1. Introduction

Many techniques have been developed for detecting and measuring the uncharged neutron since its discovery in 1932. One of the most prevalent neutron detectors is the organic liquid scintillation detector (e.g., NE-213). These detectors are frequently used in nuclear experiments for their good energy resolution and high detection efficiency for neutrons and photons [1, 2]. Using pulse shape discrimination (PSD) techniques, liquid scintillation detectors allow for the separation of the neutron and photon signals. The techniques are based on the difference in scintillator response to neutron and photon events [1]. Since the neutron is not a charged particle, it does not ionize the scintillation material directly. It can be generally detected through nuclear interactions that produce energetic charged particles. Fast neutron detection relies on the production and detection of protons from (n,p) reactions within the detector. Therefore, hydrogen-rich materials are typically used as the detector material [1]. The most commonly used scintillator for fast neutron detection and spectroscopy is the NE-213 liquid scintillator produced by Nuclear Enterprises Limited. The most significant advantage of this scintillator is its excellent pulse-shape discrimination properties compared to other scintillators [1].

^{3}He gas proportional counters are common neutron detectors best suited for the detection of thermal neutrons since the $^3He(n, p)$ reaction is attractive for thermal neutron detection. ^{3}He counters are not suitable for operation in the Geiger-Müller region since there is no capability to discriminate the pulses produced by photon interactions [1]. The neutrons are captured by the $^3He(n, p)^3H$ reaction, producing a proton and a triton with a reaction Q-value of 764 keV. The energy dependent cross section of this reaction is one of the well-known standards in neutron measurements. Since the proton and triton are charged ions, both will usually be registered by the proportional counter [1]. Another widely used detector for thermal neutrons is the BF_3 proportional detector. Boron trifluoride behaves as a proportional gas and the target for thermal neutron conversion into secondary particles. Enriching the ^{10}B in the gas can make the detector up to five times more efficient [1].

Bubble Technology Industries (BTI) has manufactured a portable neutron scintillation spectrometer (N-Probe) with potential applications at nuclear reactor facilities, spent fuel storage areas, and waste processing operations [1]. Fig. (1) shows the N-Probe spectrometer which contains a 5 cm by 5 cm NE-213 liquid scintillator detector to measure fast neutrons between 800 keV and 20 MeV, as well as a spherical ^{3}He detector to measure low energy neutrons from 0 to 1.5 MeV [1]. Sophisticated proprietary pulse-shape discrimination is used to remove undesirable photon counts for the NE-213 liquid scintillator detector. These two detectors work simultaneously and pulse-height distributions from both are shown during the measurements. The detector's software merges information from the two detectors to generate a single neutron energy spectrum. One of the significant advantages of the N-Probe is that it provides both the neutron energy spectrum and the total neutron counts for fast neutrons and thermal neutrons.

Scientists have been working on dead-time problems for radiation detectors since the 1940s. In any detector system, a minimum amount of time must separate two events before they can be measured independently. This minimum time separation is referred to as the counting system's dead-time [1]. The intrinsic properties of the detector and the pulse processing circuitry's characteristics are the sources of dead-time. Researchers have been working on improving a detector dead-time model that can implicitly characterize a detection system's behavior while reducing counting errors [1, 2].

Fig. 1. N-Probe fast and thermal neutron spectrometer [9].

There are two commonly known dead-time models: the "Paralyzing" and the "Non-paralyzing" models. In reality, detection systems fit neither of these idealized models perfectly, instead falling somewhere between the two models [1]. The paralyzing model is mathematically expressed by Eq. (1), where *m* is the measured count rate, *n* is the true count rate and τ is dead-time. This model assumes that each event during the dead-time will reset it to a fixed duration, thus extending the dead-time. The dead-time extension depends on the count rate.

$$m = ne^{-n\tau} \tag{1}$$

According to the non-paralyzing model, dead-time is fixed after each detected event, and all events occurring during dead-time are lost. The fraction of time during which an apparatus is sensitive is 1-$m\tau$. Therefore, the fraction of the true number of events can be recorded as seen in Eq. (2) [14].

$$m = \frac{n}{1+n\tau} \tag{2}$$

The dead-time of the N-Probe detector is not provided by the manufacturer; BTI, and there is no other dead-time study published on the N-Probe detector. In this study, the dead-time of the BTI N-Probe (NE-213 Liquid scintillation) was examined using different thicknesses of Plexiglas at the Missouri University of Science and Technology Research Reactor (MSTR). Furthermore, the dead-time of the Canberra 10 mm diameter ^{3}He tube detector [1] was calculated by comparing measured counts from different locations in the subcritical assembly at MSTR with MCNP simulations. The dead-time calculations are provided for both the paralyzing and non-paralyzing models for the fast neutron detector (N-Probe) and the Canberra 10 mm diameter ^{3}He tube detector.

During all experiments, the reactor operated at 5 kW power for a standardized neutron flux from the beam port. The macroscopic cross section of Plexiglas was calculated for fast neutrons using the fast neutron detector (N-Probe). For the total macroscopic cross section measurements, the flux was low, and hence the effect of the detector dead-time can have assumed to be negligible at 5 kW reactor power. The neutrons were attenuated by different thicknesses of Plexiglas and counted by the detector in front of MSTR beam port.

For ^{3}He detector dead-time calculations, the MSTR Subcritical Assembly was filled with water and its plutonium-beryllium (PuBe) neutron source was used for measurements.

The MSTR Subcritical Assembly was also simulated using MCNP code for all positions. Using the combination of measurement and simulation results, the dead-time of ^{3}He detector was calculated.

2. Experimental Design

2.1 Dead-time Experiment for N-Probe Fast Neutron Detector

The MSTR is a swimming pool type reactor licensed to operate at 200 kW. The beam port, which is 15.24 cm in diameter and 6.45 m long, was used to take fast neutron measurements [1]. A special 2-cm-diameter collimator was used for the neutron beam from the beam port to the Plexiglas. During the experiment, the operation of the detector and measurement was controlled remotely by a computer to avoid any radiation exposure. Fig. (2) shows the experimental set-up of the system to measure fast neutrons with N-Probe detector in the beam port room of the MSTR. This set-up allowed for a beam of neutron with post moderation energy distribution to be available for measurement.

Fig. 2. Illustration of experimental setup

Fast neutron measurements were first taken with no plexiglass. A 0.5-cm-thick layer of plexiglass was then placed between the detector and collimator. The neutron measurements were taken from 0 to 3.0-cm-thick layers of plexiglass using thickness intervals of 0.5 cm. Measurements with and without plexiglass were taken for ten minutes with a constant flux/beam intensity at 5 kW power. With the reactor still at 5 kW, the beam port was closed to replace the plexiglass after each measurement.

Since neutrons are neutral particles, they interact weakly with matter; it is for this reason that they have the potential to penetrate deeper. Light atoms (e.g, hydrogen, oxygen) can interact with neutrons with a high interaction probability. If a narrow beam attenuation experiment is implimented for neutrons, as shown in Fig. (2), the number of neutrons will decrease exponentially with absorber thickness. The relationship between incoming neutron beam and transmitted beam is given as

$$I = I_0 . e^{-\Sigma_{TOT} . x} \tag{3}$$

where Σ_{TOT} is the total macroscopic cross section -- the probability per unit path length that an interaction will take place -- and x is the thickness of the absorber [1]. The above equation is valid for thin shielding thicknesses; when there is no build-up. The total macroscopic cross section is given as

$$\Sigma_{TOT} = \Sigma_a + \Sigma_s + .. \tag{4}$$

where Σ_a is the absorption cross section and Σ_s is the scattering cross section. So, under the assumption of thin shield all neutron going through either absorption or scattering interaction with the shielding are lost from the beam. Fig. (3) illustrates the neutron capture and scattering interaction probabilities and assumes that only those neutrons which do not interact with matter will arrive at the detector.

Assuming the incident number of true neutrons (n_0) is equal to the intensity of incident neutrons (I_0), then the transmitted number of true neutrons (n_1) can be expressed as

$$n_1 = n_0 . e^{-\Sigma_{TOT} . x} \tag{5}$$

The total neutron macroscopic cross section under thin shield assumption can be calculated as

$$\Sigma_{TOT} = -\frac{1}{x}\ln(\frac{n_1}{n_0}) \tag{6}$$

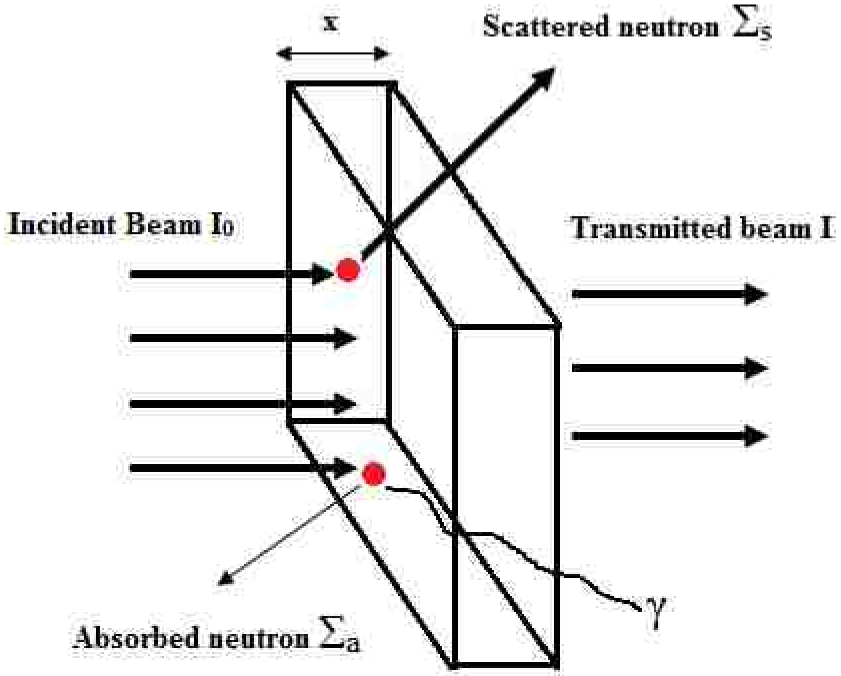

Fig. 3. Neutron capture and scrattering interaction probabilities

With no Plexiglas between the detector and collimator, the non-paralyzing measured count rate can be written as the following:

$$m_0 = \frac{n_0}{1+n_0\tau} \tag{7}$$

where m_0 is the measured count rate and n_0 is the true count rate with no shielding or absorber between the detector and collimator. With the addition of shielding and/or absorber between the detector and collimator, the non-paralyzing model becomes;

$$m_1 = \frac{n_1}{1+n_1\tau} \tag{8}$$

If another layer of shielding and/or absorber were added between the detector and collimator, then m_1 and n_1 would become m_2 and n_2, respectively. The ratio between m_0 and m_1 is given as

$$\frac{m_0}{m_1} = (\frac{n_0}{1+n_0\tau}).(\frac{1+n_1\tau}{n_1}) \tag{9}$$

where n_1 is shown in Eq. (5). Substituting this into Eq. (9) provides the following ratio:

$$\frac{m_0}{m_1} = \left[\frac{1+n_0\tau e^{-\Sigma_{TOT}.x}}{(1+n_0\tau).e^{-\Sigma_{TOT}.x}}\right] \tag{10}$$

If there were a second shielding layer, Eq. (10) would become

$$\frac{m_0}{m_2} = \left[\frac{1+n_0\tau e^{-\Sigma_{TOT}.2x}}{(1+n_0\tau).e^{-\Sigma_{TOT}.2x}}\right] \tag{11}$$

From Eqs. (10) and (11), it is evident that the $n_0\tau$ parameters are the same for both equations. The $n_0\tau$ parameter from Eq. (10) is;

$$n_0\tau = \left[\frac{\frac{m_0}{m_1}e^{-\Sigma_{TOT}.x} - 1}{e^{-\Sigma_{TOT}.x} - \frac{m_0}{m_1}e^{-\Sigma_{TOT}.x}}\right] \tag{12}$$

The only unknown in Eq. (12) is the total macroscopic cross section (Σ_{TOT}) of Plexiglas. Plugging all known parameters into Eq. (12) will give the total macroscopic cross section. It is important to recognize that during the experiment the beam of neutron available from the reactor was not mono-energetic. Hence, one would expect macroscopic cross section dependence on energy. However, since the detector only see fast neutron (800 keV to 20 MeV) and cross section variability with energy is minimum for such high energy neutron [1], use of a single cross section for this beam with a spectrum of fast neutron is a reasonable approximation. With this approximation of a single cross section for high energy neutrons one can make use of Eq. (12) to calculate $n_0\tau$. Once the total macroscopic cross section is found, Eq. (12) can be used to find the $n_0\tau$ parameter, which in turn can be used in Eq. (7) to find the true count rate (n_0) for the non-paralyzing model. Using the true count rate (n_0) and measured count rate (m_0) in Eq. (7) will give the detector's dead-time for the non-paralyzing model.

Using the same ratio technique demonstrated with the non-paralyzing method equations, the ratio of m_0 and m_1 can be calculated for the paralyzing model. This ratio is shown in Eq. (13).

$$\ln\left(\frac{m_0}{m_1}\right) = -n_0\tau + \Sigma_{TOT}.x + n_0\tau.e^{-\Sigma_{TOT}.x} \tag{13}$$

If there were a second shielding layer, Eq. (13) would become the following:

$$\ln\left(\frac{m_0}{m_2}\right) = -n_0\tau + \Sigma_{TOT}.2x + n_0\tau.e^{-\Sigma_{TOT}.2x} \tag{14}$$

As evidenced by Eqs. (13) and (14), the $n_0\tau$ parameters are the same for both equations. The $n_0\tau$ from Eq. (13) is

$$n_0\tau = \frac{\ln\left(\frac{m_0}{m_1}\right) - \Sigma_{TOT}.x}{e^{-\Sigma_{TOT}.x} - 1} \tag{15}$$

Once total macroscopic cross section is available for non-paralyzing model one can use the same in these equations to obtain the $n_0\tau$ factor using Eq. (15) which can subsequently be used to calculate the dead-time using Eq. (16).

$$m_0 = n_0 e^{-n_0\tau} \tag{16}$$

2.2 Dead-time Experiment for Canberra ^{3}He Detector

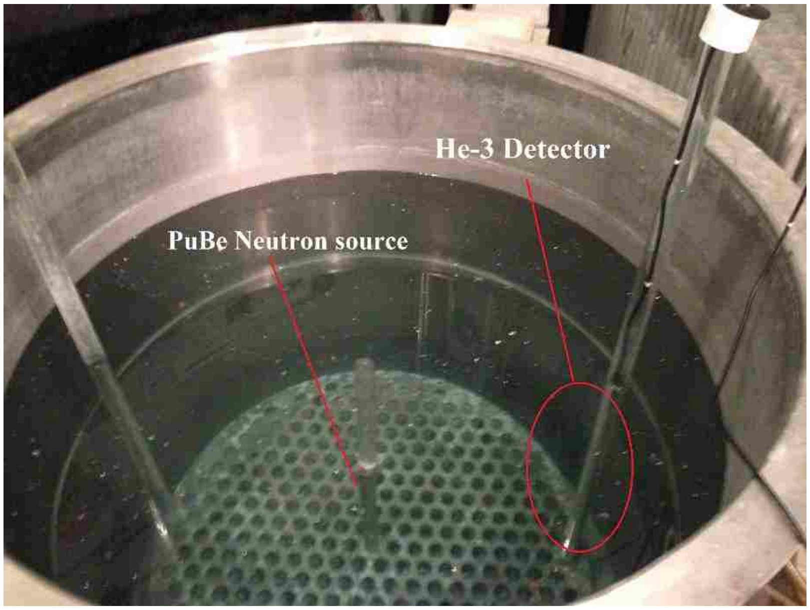

Fig. 4. Picture of ^{3}He detector neutron measurements in subcritical assembly

The following procedure was used to calculate the dead-time of a gas-filled Canberra ^{3}He detector. The Missouri University of Science and Technology (Missouri S&T) Subcritical Assembly was filled with water and its plutonium-beryllium (PuBe) neutron source was placed in the center position (see Fig. 4). The Canberra ^{3}He detector was suspended inside an acrylic tube (to protect it from the water) and placed in the grid plate position A1 (5.08 cm center-to-center). A five-minute count was taken and the detector was moved to the second position, A2, 10.16 cm from the source. This process was repeated for the remaining seven positions on the A axis and again along each of the five other axes – B, C, D, E, and F. This layout, which was also used for the MCNP simulations, can be seen in Fig. (5).

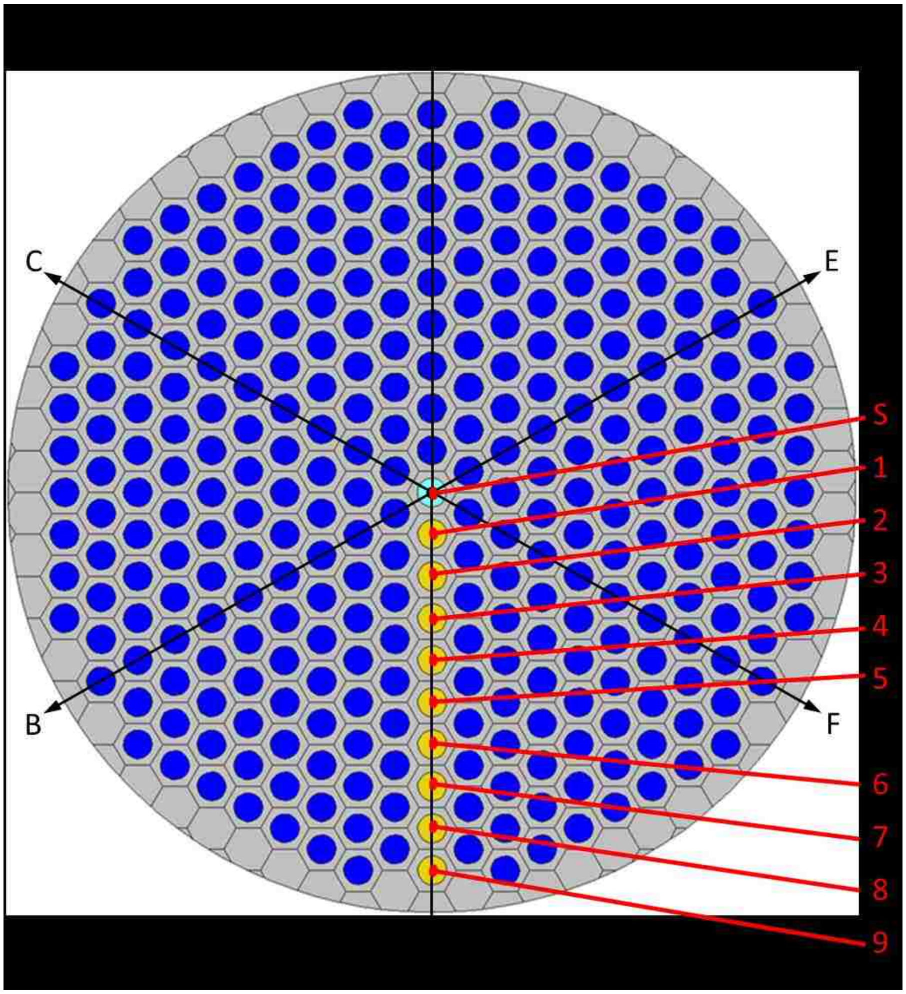

Fig. 5. MCNP simulation layout. The Pu-Be neutron source (S) was placed in the center-most position of the subcritical assembly. Nine MCNP simulations and nine measurements were performed in the numbered locations on axis A. Five more sets of measurements, repeating those made on axis A, were made on the five remaining axes.

The Canberra Lynx Digital Signal Analyzer was used to supply power to the detector and record counts [18]. An MCNP model of the Missouri S&T Subcritical Assembly was used to simulate the measurements. The model was developed by Tucker [15] and it was experimentally validated. Nine simulations were performed with the detector modeled in each of the nine detector locations along axis A. The water-filled cells between the source and the detector were given higher importance to ensure usable statistics. One hundred million histories were used for detector locations A1 through A6. One hundred fifty million histories were used for locations A7 through A9. Cell-averaged neutron flux (neutrons per square centimeter per source particle) was tallied over the detector gas portion of the modeled detector.

Measurements of a plutonium-beryllium (Pu-Be) neutron source were taken from nine distances with the Canberra ^{3}He Detector in the Missouri S&T Subcritical Assembly. These measurements were compared to the results from MCNP simulations. The difference between the measured and simulated values were attributed to dead-time losses and was used to estimate the detector's dead time.

3. Results

The dead time measurement for N-Probe was conducted using the beam port of MSTR and only fast neutron probe was used for this set of measurements. The fast neutron measurements were first taken without a Plexiglas layer, and then with six different thicknesses of Plexiglas layers. Data collection for each step was 10 minutes. The Plexiglas thickness changed from 0 cm to 3 cm with increments of 0.5 cm. The measurements are tabulated in Table 1 at 5 kW constant power for each thickness.

Table 1. The fast neutron measurements using N-Probe at 5 kW power

Plexiglas thickness (cm)	N-Probe Fast Neutrons counts	Count rates
0.0	2077857	3463.09 ± 58.85
0.5	2035029	3391.71 ± 58.24
1.0	1986735	3311.22 ± 57.54
1.5	1938566	3230.94 ± 56.84
2.0	1893107	3155.17 ± 56.17
2.5	1842570	3070.95 ± 55.42
3.0	1797494	2995.82 ± 54.73

Fig. (6) shows the plot of the neutron count rate with different thicknesses of Plexiglas. Errors were propagated based on one standard deviation (1σ) and are included on the graphs. The first count without any Plexiglas for fast neutrons using the N-Probe spectrometer was 3463.09 per second and the counts decreased with increments of Plexiglas thickness. The last count for fast neutron measurement with 3 cm thickness of Plexiglas was 2995.82 per second.

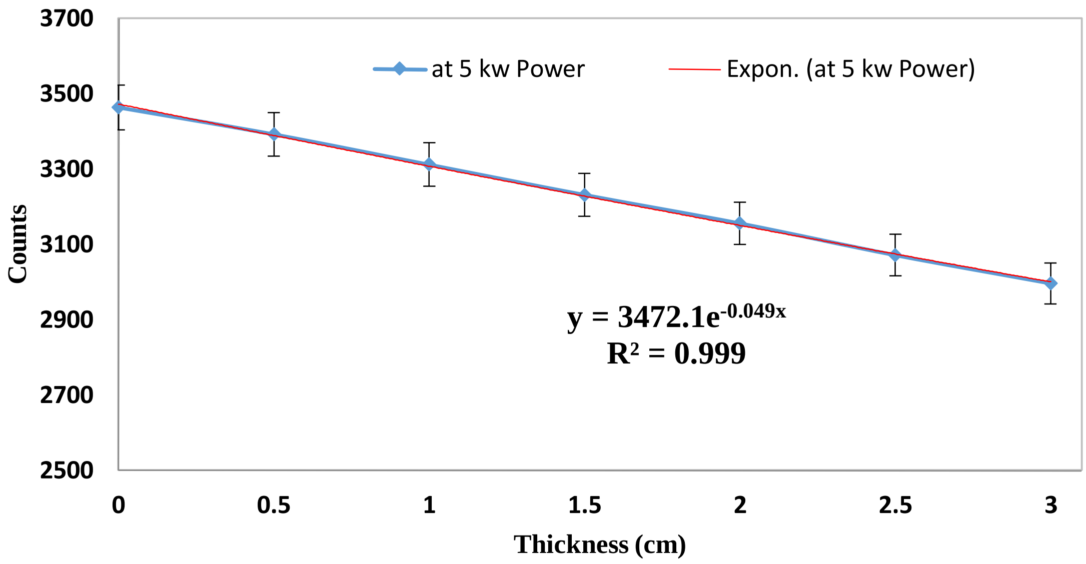

Fig. 6. Fast neutron count rates with different thickness of Plexiglass at 5 kw power.

Exponential trend line in Fig. (6) provides the total macroscopic cross section, 0.049 cm^{-1}, needed for both non-paralyzing and paralyzing dead-time calculations. The total macroscopic cross section for average neutrons are tabulated in Table 2. The total macroscopic cross sections were calculated based on total counts of fast neutrons (fast neutrons vary from 800 keV to 20 MeV) for the N-Probe. The total absorption cross section of Plexiglas can be calculated for a specific neutron energy using the same method.

The average macroscopic cross section of Plexiglas using the N-Probe liquid scintillator (Fast probe) was calculated to be 0.049 cm^{-1} for the non-paralyzing model using 0.5 cm and 1 cm thicknesses. Same macroscopic cross section can be used for the paralyzing model since the same Plexiglas thicknesses were used for dead-time calculations for paralyzing dead-time model.

Table 2. Total macroscopic cross section (Σ_{TOT}) for Plexiglas using all counts

Plexiglas Thickness (cm)	ΣTOT (1/cm) Non-Paralyzing Method	ΣTOT (1/cm) Paralyzing Method
0.5	0.049	0.049
1	0.049	0.049

Based on a combination of the attenuation law and non-paralyzing and paralyzing dead-time models, the dead-time of the fast probe (N-Probe detector) was calculated. Eqs. (7), (10) and (12) were used to calculate dead-time for the non-paralyzing model while Eqs. (13), (15) and (16) were used to calculate dead-time for the paralyzing model. Table 3 shows the dead-time calculations for the N-Probe detector. Non-paralyzing dead-time of the detector was found to be 43.7 µs with an error of ± 5.24 and paralyzing dead-time of the detector was found to be 37.6 µs with an error of ± 5.33. As was expected, dead-time based on non-paralyzing assumption for the detector was higher than paralyzing dead-time. Error propagations (S_τ) of dead-time measurements for both idealized models were calculated using Eq. (17). s_m and s_n are individual errors of measured counts and true counts.

$$S_\tau^2 = (s_m \frac{\partial \tau}{\partial m})^2 + (s_n \frac{\partial \tau}{\partial n})^2 \tag{17}$$

Table 3. Dead-time calculations of N-Probe for two ideal models

Plexiglas thickness (cm)	Non-Paralyzing Dead-time (µs)	Errors	Paralyzing Dead-time (µs)	Errors
0.5	43.7	± 5.24	37.6	± 5.34
1	43.7	± 5.22	37.6	± 5.33

It is important to notice that the above technique assumes that the build-up of neutron flux is insignificant for the geometry with half and one cm Plexiglas.

After calculating the dead-time of the detector, a high count rate experiment was conducted and the count rates were corrected using non-paralyzing and paralyzing dead-times (see Fig. 7). As count rate increases, the dead-time effect of the detector increases. The dead-time effect is almost negligible at low count rates. In the experiment, fast neutron counts were high at around 900 keV and the dead-time effect is observable and the two model seems to be separating the predictions significantly.

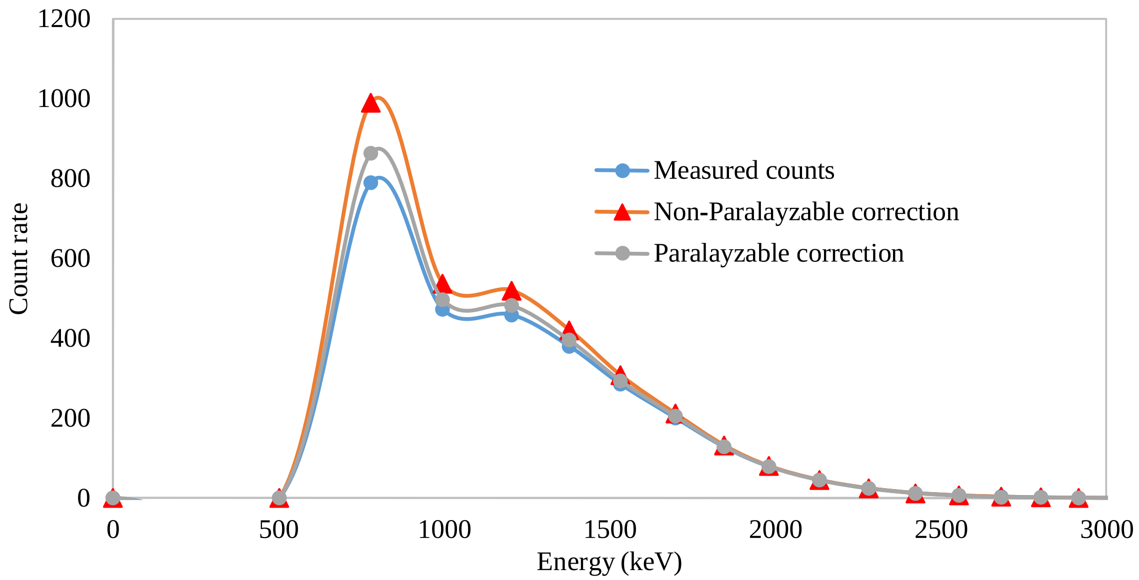

Fig. 7. Fast neutron count rates with different thickness of Plexiglass at 5 kw power.

For the Canberra ^{3}He detector (0.5NH1/1K) subcritical assembly was used to calculate the detector dead time. Measurements of a plutonium-beryllium (PuBe) neutron source were taken from nine distances with the Canberra ^{3}He detector in the Missouri S&T Subcritical Assembly. These measurements were compared to results from well calibrated MCNP model simulation results. The difference between the measured and simulated values was attributed to dead time losses. Using this difference dead time was estimated for the detector. The results of the measurements are provided in Table 4.

The results of the measurements (counts per second) and simulations (n cm^{-2} sp^{-1}) cannot be directly compared so both sets of data were normalized to their smallest value (see Fig. 8) for which dead time effects were considered to be negligible. In order to calculate detector dead time, the true and measured count rates must be known. The collection of the measured count rate has already been discussed. The MCNP results were used to generate the true count rate. To do this, each tally result generated by MCNP was divided by the tally result for the ninth detector position (45.72 cm from the source) and multiplied by the measured value at the ninth detector position as seen in Eq. (18).

$$True\ Count\ Rate = \frac{S_i}{S_9} M_9 \tag{18}$$

Table 4. Neutron measurements from the Canberra ^{3}He Detector in the Subcritical Assembly

Distance from PuBe neutron source (cm)	Count rate (counts s-1)
5.08	12661.98 ± 156.32
10.16	7522.19 ± 53.33
15.24	2935.79 ± 56.30
20.32	1101.94 ± 26.70
25.40	439.10 ± 30.23
30.48	174.85 ± 5.29
35.56	74.17 ± 2.06
40.64	33.18 ± 0.68
45.72	15.44 ± 0.52

Table 5. Results of MCNP simulations of Canberra ^{3}He neutron detector in the Subcritical Assembly

Distance from PuBe neutron source (cm)	Cell-averaged Flux Tally Result (n cm-2 sp-1)
5.08	2.40851E-03 ± 4.09447E-
10.16	1.43884E-03 ± 3.02156E-
15.24	5.57542E-04 ± 1.95140E-
20.32	2.01799E-04 ± 1.10989E-
25.40	7.43707E-05 ± 6.76773E-
30.48	2.98034E-05 ± 4.26189E-
35.56	1.21184E-05 ± 2.13284E-
40.64	5.59834E-06 ± 1.45557E-
45.72	2.32741E-06 ± 9.12345E-

Where S represents the tally result from MCNP and M represents the measured value. Eq. (18) was applied to the results for the eight closest detector distances and the dead-time at each location was calculated according to both the paralyzing and non-paralyzing models. The ninth location was excluded because this position was used for normalization process and cannot be used to calculate a dead-time using Eq. (18). The results of the simulations are provided in Table 5. The paralyzing dead-time was calculated to be 14.5 µs, and the non-paralyzing dead-time was calculated to be 16.4 µs.

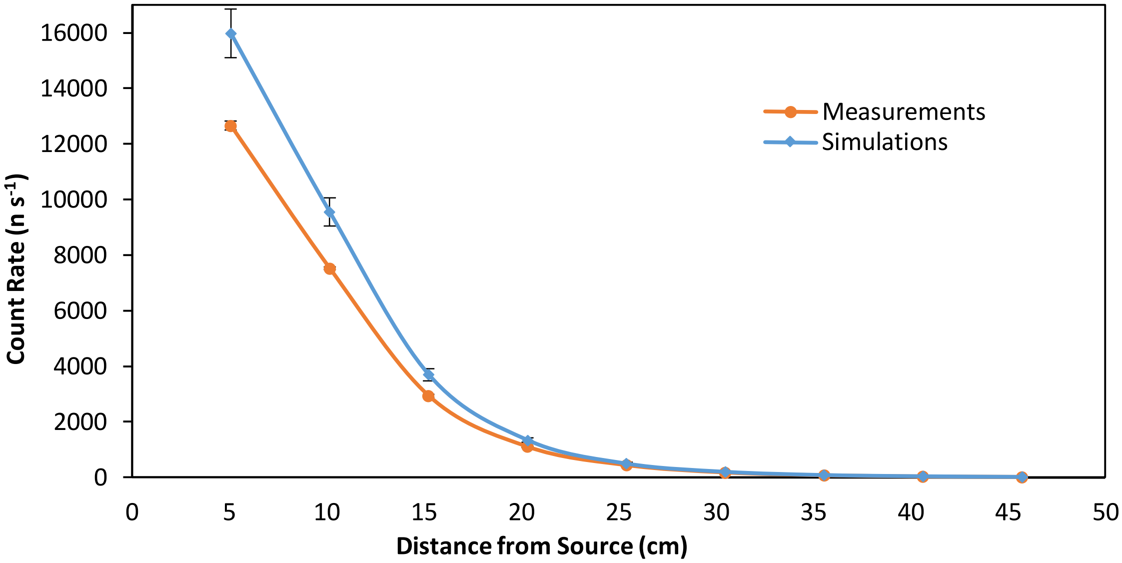

Fig. 8. The results of the measurements and simulations, normalized to their lowest values for comparison.

4. Conclusion

The N-Probe utilizes two different spectroscopic techniques for providing neutron spectrum. From 800 keV to 20 MeV, the fast neutron energy region is measured by a liquid scintillator combined with a photon discriminator (fast probe). From 0 to 800 keV, the thermal neutron energy region is measured by a spherical ^{3}He detector. The dead-time of the fast probe was determined via the combination of the attenuation law and idealized dead-time models. All measurements were taken in front of the beam port at the Missouri S&T Research Reactor (MSTR) while at 5 kW constant power. The paralyzing dead-time value of N-Probe Liquid scintillator detector was found to be 37.6 ± 5.34 µs, while the non-paralyzing dead-time value was found to be 43.7 ± 5.24 µs. At this point we were not able to compare the dead-time value of N-Probe liquid scintillator detector with BTI N-Probe detector manual since the company strictly protecting this information. Dead-time values for the fast probe were higher than expected since average liquid scintillator dead-time is 1 to 10 µs [6]. The same method was used to calculate the dead-time of the N-Probe thermal neutron probe at 5 kW power (constant flux). However, some fast neutrons thermalized when the layers of Plexiglas was placed in front of detector. These thermalized neutrons affect the dead-time calculations and result in negative dead-time values.

The dead-time of a tube-type Canberra ^{3}He gas-filled detector was calculated for both non-paralyzing and paralyzing dead-time models using subcritical assembly measurements and MCNP simulations. The paralyzing dead-time was calculated to be 14.5 µs, and the non-paralyzing dead-time was calculated to be 16.4 µs for ^{3}He gas filled detector. The dead-time of gas-filled proportional (especially GM counters) detectors generally lies between 100 and 300 µs [6]. However, Hashimoto and Ohya [20] used a variance to mean method to calculate the dead-time of a ^{3}He proportional counter and its dead-time was found to be approximately 10 µs. Calculated dead-time value of ^{3}He gas filled detector is agreed with their result in the order of magnitude.

References

[1] V. V. Verbinski, et al., Calibration of an organic scintillator for neutron spectrometry. Nucl. Instrum. Methods 65, 8–25, (1968).

[2] J. A. Harvey, and N. W/ Hill, Scintillation detectors for fast neutron physics, Nucl. Instrum. Meth. 162, 507, (1979).

[3] I. Yousuke, et al., "Deterioration of pulse-shape discrimination in liquid organic scintillator at high energies". Nuclear Science Symposium Conference Record, 1,219–221, (2000).

[4] G. F. Knoll, Radiation Detection and Measurement. 4th Edition, p.573, 2010, John Willey & Sons Inc, USA.

[5] M. Karlsson, Absolute efficiency calibration of NE-213 liquid scintillator using a 252Cf source, Department of Nuclear Physics in Lund University, Sweden, 1997.

[6] N. Tsoulfanidis, S. Landsberger, Measurement and Detection of Radiation. 3th Edition, 2011, CRC Press. Taylor & Francis Group. New York.

[7] T. W. Krane, and M. N. Baker, Neutron Detectors Chapter 13, http://www.lanl.gov/orgs/n/n1/panda/00326408.pdf (Accessed, September 2014).

[8] G. F. Knoll, Radiation Detection and Measurement. 4th Edition, p.523, 2010, John Willey & Sons Inc, USA.

[9] H. Ing, et al., Portable Spectroscopic Neutron Probe, Radiation Protection Dosimetry, 126, 238-243, (2007).

[10] Mobile Microspec Operational Manual, Bubble Technology Industries Inc (BTI), Revised: October 30, 2009.

[11] J.W. Muller, Dead-time problems. Nuclear Instruments and Methods. 112, 47-57, (1973).

[12] J.W. Muller, Generalized Dead Times, Nuclear Instruments and Methods, 301,543-551, (1991).

[13] H. G. Stever, The discharge mechanism of fast G-M counters from the dead-time experiment, Phys. Rev. 61, 38-52, (1942).

[14] W. Feller, On probability problems in the theory of counters, in R. Courant Anniversary volume, Studies and Essays. Interscience. New York. 105-115, (1948).

[15] L. P. Tucker, Upgrade and simulation of the subcritical assembly at Missouri University of Science and Technology, Master's Thesis, Missouri University of Science and Technology. Rolla, MO. 2011.

[16] "Missouri S&T Nuclear Reactor" Missouri University of Science and Technology Nuclear Engineering Department. http://nuclear.mst.edu/research/reactor/ (2016).

[17] J. R. Lamarsh, Introduction to Nuclear Engineering, 3rd Edition, p. 57, 2001, Prentice Hall, New Jersey, USA.

[18] Canberra Industries, Inc., Lynx Digital Signal Analyzer Data Sheet, Meriden, Conn., 2012.

[19] D. J. Loaiza, High-efficiency ^{3}He proportional counter for detection of delayed neutrons, Nuclear Instuments and Methods in Physics Research A, 422, (1999), 43-46.

[20] K. Hashimoto and K. Ohya, Dead-time measurement for radiation counters by variance to mean method, Journal of Nuclear Science and Technology, 33, 863-868, (1996).

II. CHARACTERIZATION OF BEST CANDIDATE ISOTOPES FOR BURNUP ANALYSIS AND MONITORING OF IRRADIATED FUEL

T. Akyurek, L.P. Tucker, and S. Usman

Department of Mining and Nuclear Engineering, Missouri University of
Science & Technology, Rolla, MO 65409, USA

Abstract

This research is an extension of feasibility study of MOX fuel online burnup analysis. A multitude of fission products identified as candidates have been scrutinized for their suitability of burnup analysis and spent fuel analysis. Best isotopes obtained for analysis by investigating half-life, fission yield, branching ratios, production modes, thermal neutron absorption cross section and fuel matrix diffusivity. ^{132}I and ^{97}Nb are identified as good isotope candidates for on-line burnup analysis. ^{132}I is also a good candidate for plutonium/uranium discrimination due to the large difference in the fission yield of the isotope. For interim storage monitoring the well-established cesium isotopes appears to be the best choices unless the data gaps are addressed. Only alternate for cesium for interim monitoring is ^{131}I at the present time. For the long-term storage monitoring ^{94}Nb is the most attractive candidate. It has a low diffusion rate of ~10^{-11} cm^2/s, an almost zero neutron absorption cross section making it burnup history independent and decent gamma yield of 1.44E-09. In addition, the paper also identifies the data gaps for developing a robust burnup analysis tool using gamma spectroscopy.

1. Introduction

Between 1977 and 1981 commercial reprocessing was banned by the United States government, interrupting the U.S. reprocessing industry. The U.S. moratorium on 88 reprocessing did not, however, discourage European countries such as France from developing the technology and incorporating Mixed OXide (MOX) fuel into their nuclear fuel cycle. While other nations pursued reprocessing, the U.S. chose to invest in the Yucca Mountain Nuclear Waste Repository. However, with Yucca Mountain no longer under consideration, the U.S. is reconsidering its fuel cycle options, and taking a second look at reprocessing and MOX fuel [1, 2].

Decades of operation in France have demonstrated that MOX fuel can be incorporated into a UO_2 fueled core without risking the safety of the plant or increasing the risk of proliferation [3]. Now the U.S. power industry is investigating the fuel. In 2005, Duke Energy commissioned AREVA to build four MOX fuel assemblies for the Catawba Nuclear Station. The Megatons to Megawatts program is another major commitment by the U.S to incorporate MOX into the fuel cycle. This program is an agreement between the United States and Russia to dispose of approximately 35 metric tons (MT) of weapons-grade plutonium by converting it into MOX fuel to be burned in commercial nuclear power plants. The MOX fuel assemblies will be manufactured at the Department of Energy's Savannah River Site through a contract with Duke COGEMA Stone & Webster. As of July 2012, this program has converted 450 MT of weapons-grade uranium to low-enriched fuel for power reactors [4].

Thorium fueled reactors are also under consideration because of the advantages of the thorium fuel cycle. Thorium is abundant in the earth's crust. With roughly four times the concentration of uranium, it can be found across the globe. And because ^{238}U is not usually present in thorium fuel there are fewer transuranic elements in the spent fuel [5]. Thorium-based fuels can also be used for plutonium destruction. As there is no plutonium created during use all the plutonium burned is gone for good. The only downside is that fissile ^{233}U is produced, which has many of the same proliferation concerns.

Regardless of how the U.S. fuel cycle changes, better tools and techniques for measuring burnup and monitoring spent fuel will be required. One attractive option for non-destructively examining spent fuel is gamma spectroscopy. In this work, a multitude of fission products identified as candidates for burnup analysis and spent fuel monitoring, as proposed by Dennis and Usman [6], are scrutinized for their suitability for such a program. Consideration is given to half-life, fission yield, branching ratios, thermal neutron absorption cross section, production modes and fuel matrix diffusivity. Based on these parameters, the best isotopes for non-destructive burnup analysis and spent fuel monitoring have been identified.

2. Traditional Tools, Techniques and Conventional Isotopes for Burnup Analysis

A report was published by US Nuclear Regulatory Commission [7] discussing various aspects of spent fuel monitoring and the requirements of the measurements system. There are two broad groups of techniques available; “passive” measurement of delayed neutrons and gamma and “active” interrogation by either a pulsed neutron source or a weak steady state source and subsequently monitoring the gamma and/or neutron emissions. For safe transportation of spent nuclear fuel it is critical to have a reliable and efficient monitoring system capable of on-site, accurate measurement of the spent fuel to ensure compliance with the safety criteria. Gamma measurement is one non-destructive technique (NDA) for spent fuel monitoring, analyzing the radiation emitted by irradiated nuclear fuel assemblies to determine parameters such as burnup, cooling time, and a qualitative verification of the irradiation history [8]. These parameters can be calculated with the help of flux measurements in the core and following the path of the fuel assembly as it proceeds with its burnup cycle. These calculations can be experimentally verified by the above mentioned techniques. Willman and co-workers [9] have investigated ^{137}Cs ($T_{1/2}$ = 30.1 years), ^{134}Cs ($T_{1/2}$ = 2.1 years) and ^{154}Eu ($T_{1/2}$ = 8.6 years) as indictors of cooling time and irradiation history since these isotopes dominate the gamma spectrum of spent fuel after five years of cooling time [7]. Moreover, the isotope has very small neutron absorption cross sections and hence negligible burnup history dependence and its fission yields from ^{235}U and ^{239}Pu is approximately the same. Willman and co-worker [10] has reported the success of using ^{154}Eu while Dennis and Usman [11] reported the potential of using ^{106}Ru. Because of their relatively long half-lives, these isotopes are most useful for analyzing used fuel after about 10 years of cooling. Focus of this manuscript is to analyze new isotopes for their suitability as a burnup indicator. The conventional fission isotopes (^{137}Cs, ^{154}Eu, ^{106}Ru etc.) already considered for burnup analysis are not included in this discussion with the exception of ^{134}Cs which is included for comparison. Interested reader may refer to literature [8-11] for discussion on the conventional burnup isotopes.

Another NDA technique for power reactor released spent fuel is based on neutron measurements. A series of neutron absorptions in ^{238}U leads to the production of ^{244}Cm. Spontaneous fission of ^{244}Cm provides a source of “delayed neutron”. Since the half-life of ^{244}Cm is 18.1 years, neutrons from ^{244}Cm are a measure of burnup. This technique is sensitive to cooling time, and initial enrichment for the spent fuel. Additional information on neutron measurement based burnup calculation is available in the literature [12].

Additionally, chemical assay with mass spectroscopic techniques [13] have historically been applied to determine isotopic composition of spent nuclear fuel but these techniques requires fuel sample destruction and can take a long time for sample analysis 91 and results. Recent new attempts for spent nuclear fuel analysis include use of digital measurement of Cherenkov [14]. A patent is also been filed by Dowdy and co-workers [15] on the application of Cherenkov radiation for irradiated fuel monitoring.

Focus of this manuscript is to compare the advantages of various isotopes for gamma emission based spent fuel measurement. While other techniques are available gamma measurement based spent fuel monitoring is the most commonly used technique.

3. Important Indicators for Burnup Analysis and Spent Fuel Monitoring

Burnup measurement are useful for a number of applications including; pre-transportation compliance certification, monitoring of spent fuel for Special Nuclear Material (SNM) accountability and proliferation deterrence, monitoring during storage for historic burnup analysis and online burnup measurement for next generation reactors for fuel cycle optimization. Additional spent fuel monitoring is required during reprocessing operation. For each of these application one or more of the techniques described in the previous section is better suited than others.

Half-life of the burnup indicator isotope is one characteristic that can dramatically impact its suitability for different applications; online applications, interim storage and long-term storage. A nuclide with a half-life between minutes and days is ideal for online burnup determination but useless for historical data collection. For interim storage-pool monitoring, the indicator’s half-life should be between a few days and a few years. Burnup indicators for long-term storage applications should have half-lives greater than few years.

Another desirable characteristic for burnup and used fuel monitoring indicators is a simple production mode and a simple decay chain. Generally, it is significantly more complicated to track the decay of a candidate isotope with multiple decay modes and multiple production modes, which via direct fission and by decay of several fission products. However, in certain situations this can be an advantage. A single production path (production from single parent nuclide or direct production from fission) coupled with a high fission yield ensures that a detectable amount of the isotope would be present. Since the emitted gamma rays must potentially penetrate several layers of fuel, cladding, and moderator, a high energy gamma ray (on the order of MeV) with a high branching ratio is also necessary for detectability.

It is also important for the indicator isotope to remain in the fuel where it was created after it is produced. Therefore, the neutron capture cross-section must be as low as possible and must not exceed more than a few barns so that product atoms density is independent of burnup history. Small neutron absorption cross section also ensures that burnup indicator isotope generated from fission is not subsequently consumed by parasitic neutron absorption. Low fission product migration at high temperatures is another desirable characteristic. The fission product must ideally remain where it was created. Any migration of fission products will skew the burnup profile of the assembly [16].

4. Candidate Isotopes

^{137}Cs, ^{134}Cs and ^{154}Eu are commonly used isotopes for burnup analysis and fuel monitoring. Recently Willman et al. investigated two correlations between burnup and the intensity of these isotopes. They proposed a linear correlation between burnup and the intensity of the 661.7 keV ^{137}Cs peak while they found that ^{154}Eu and ^{134}Cs is related to the 93 square of burnup [9]. Hawari and co-workers [17] have considered gamma spectrometry of Cs-137 and Eu-154 for online burnup monitoring of pebble bed reactors. Jansson and co-workers [18] provide corroborating evidence that there is a correlation between ^{137}Cs intensity and burnup for Pressurized Water Reactor (PWR) assemblies [18]. Dennis and Usman [11] proposed ^{106}Ru isotope for MOX fuel burnup analysis. They studied the feasibility of using ^{106}Ru as a burnup indicator for UO_2 fuel and as a means for discriminating between MOX and UO_2 fuel. Their ORIGEN-ARP (Oak Ridge Isotope Generation and Depletion Code – Automatic Rapid Processing) simulations showed a linear correlation between primary photopeak intensity and MOX fuel assembly burnup for ^{137}Cs and ^{106}Ru. They relied on using peak ratios rather than raw peak counts to normalize and remove the burnup history dependence.

This paper analyzes the list of candidate isotopes proposed by Dennis and Usman [6] for their suitability for burnup analysis application. These isotopes are listed in Table 1. To complete the analysis, data was collected on the half-life, fission yield, branching ratios, diffusivity, and neutron absorption cross section for each of the candidate isotope. Some nuclides lacked data for some of these characteristics, leaving room for additional research. However, based on an analysis of the data that was available, the best isotopes for burnup analysis and irradiated fuel monitoring have been identified.

There are some isotopes in Table 1 that decay with virtually identical photon energies. For example, ^{137m}Ba, ^{98}Tc, and ^{132}Cs have almost same photon energy and emission probability values. It would be difficult to distinguish these isotopes based on gamma spectroscopy alone. However, their half-lives differ by orders of magnitude. ^{137m}Ba has a half-life of 2.55 min, which will decay quickly. The half-life of ^{98}Tc is 4.2 million years, making it practically stable. ^{132}Cs has half-life of 6.48 days. For these situations one may consider using an unfolding technique to determine correct apportionment of summed peak and separating say ^{137m}Ba from ^{98}Tc.

Table 1. Reference isotopes for burnup analysis and spent fuel monitoring [6]

Simulation Energy (keV)	**Potential Isotope**	**Energy (MeV)**	**Photon Emission Probablity**	**Simulation Energy (keV)**	**Potential Isotope**	**Energy (MeV)**	**Photon Emission Probablity**
76.6110	^{243}Am	0.07467	0.66	617.82	^{108m}Ag	0.61437	0.90393
	^{206}Bi	0.074969	0.54146		^{43}K	0.61749	0.80514
	^{61}Co	0.067412	0.85		^{190m}Os	0.61608	0.9862
	^{73}Se	0.067	0.7729601		^{144}Pm	0.61801	0.98597
	^{44}Ti	0.07838	0.97619	626.15	^{43}K	0.61749	0.80514
93.2640	^{49}Cr	0.090639	0.532		^{144}Pm	0.61801	0.98597
101.5900	^{67}Ga	0.93311	0.357		^{148m}Pm	0.62997	0.88998
134.9000	^{99m}Tc	0.14051	0.8907	659.46	^{137m}Ba	0.66165	0.8998
143.2200	^{99m}Tc	0.14051	0.8907		^{132}Cs	0.66769	0.97423
	^{85m}Kr	0.15118	0.75278		^{130}I	0.66854	0.96129
159.8700	^{52}Fe	0.016868	0.966		^{132}I	0.66769	0.987

Table 1 continued.

	^{56}Ni	0.15838	0.98795		^{97}Nb	0.6579	0.9809
176.5300	^{52}Fe	0.016868	0.966		^{126}Sb	0.66633	0.99619
	^{111}Ln	0.17128	0.9024	667.78	^{137m}Ba	0.66165	0.8998
193.1800	^{90}Y	0.20251	0.96631		^{98}Tc	0.65241	0.99745
	^{166m}Ho	0.18442	0.726		^{132}Cs	0.66799	0.97423
	^{190m}Os	0.18673	0.702		^{130}I	0.66854	0.96129
226.4900	^{85m}Sr	0.23169	0.84725		^{132}I	0.66769	0.987
	^{132}Te	0.22816	0.88	692.76	^{97}Nb	0.6579	0.9809
276.4400	^{203}Hg	0.27919	0.773		^{126}Sb	0.66633	0.99619
	^{203}Pb	0.27919	0.768		^{94}Nb	0.70293	1
318.0800	^{192}Ir	0.31651	0.82853	717.74	^{144}Pm	0.69649	0.99492
	^{5}1Ti	0.32008	0.929		^{126}Sb	0.695	0.99619
	^{157}Dy	0.32616	0.938		^{108m}Ag	0.72295	0.90499
326.4000	^{194m}Ir	0.32845	0.929	751.05	^{166m}Ho	0.71169	0.54087
	^{51}Ti	0.32008	0.929		^{126}Sb	0.7205	0.53794
	^{157}Dy	0.32616	09.38		^{244}Am	0.746	0.67
359.71	^{73}Se	0.3611	0.965		^{52}Mn	0.74421	0.9
	^{190m}Os	0.36109	0.9488		^{97m}Nb	0.74336	0.9796
	^{131}I	0.36448	0.81164	759.37	^{98}Tc	0.74535	0.99819
376.36	^{43}K	0.37276	0.87273		^{95}Zr	0.75671	0.55345
	^{204m}Pb	0.89915	0.99164		^{95}Nb	0.76579	0.99808
	^{200}Tl	0.36794	0.873	767.7	^{95}Tc	0.76579	0.9382
434.64	^{108m}Ag	0.43393	0.89881		^{95}Zr	0.75671	0.55345
	^{202}Tl	0.43956	0.915		^{82}Br	0.77649	0.8331
	^{69m}Zn	0.43863	0.94889		^{132}I1	0.77261	0.76196
484.6	^{181}Hf	0.48203	0.825	792.68	^{95}Nb	0.76579	0.99808
	^{194m}Ir	0.48286	0.97		^{95}Tc	0.76579	0.9382
	^{87}Y	0.4847	0.9394	809.33	^{134}Cs	0.79584	0.854
	^{90m}Y	0.47953	0.9099		^{210}Tl	0.7997	0.9896
492.93	^{190}Os	0.50255	0.9778		^{206}Bi	0.8031	0.9889
	^{103}Ru	0.49708	0.889		^{58}Co	0.81076	0.9943
	^{87}Y	0.4847	0.9394		^{136}Cs	0.8185	0.997
534.56	^{130}I	0.53609	0.99		^{166m}Ho	0.81031	0.57136
	^{133}I	0.52987	0.8632		^{56}Ni	0.81185	0.85996
	^{135m}Xe	0.52656	0.80997	1592	^{96}Tc	0.81254	0.81803
601.17	^{134}Cs	0.6047	0.976		^{210}Tl	0.7997	0.9896
	^{124}Sb	0.60271	0.978001		^{140}La	1.5965	0.9549

Table 2 lists the candidate isotopes from Table 1 with their half-lives and divides them into groups based on their usefulness for online burnup analysis, interim storage monitoring, and long-term or historical data applications. A cut off of ten minutes was used as the lower limit for online measurement system. This choice is based on the fact that at least 2-3 minutes would be required to transport the irradiated fuel to location where it can be measured. And a minimum of one minute count might be necessary for good statistics of the peak counts. However, if there is a slight uncertainty in the cooling/transport time the quality of measurement can be adversely impacted for a short lived isotope. Therefore, a ten minute lower limit is set for half-life for online burnup application. Hence, radioisotopes with half-lives less than ten minutes are not considered useful for any of these applications. This choice of ten minutes is also to ensure that during the measurement time (that is one min count) the activity is only going to reduce by less than 7%. Four isotopes are placed in Group 0 with half-lives less than 10 minutes and therefore minimum to no usefulness. There are 21 isotopes in Group 1 having half-lives between 10 minutes and 24 hours. Nuclides in Group 1 are suitable for online burnup analysis. For online measurement too long half-life is not useful either. The upper limit for online burnup applications half live is set at 24 hours. These choices are somewhat arbitrary. There are 30 isotopes in Group 2 with half-lives between 24 hours and 5 years. Group 2 nuclides are ideal for interim-storage pool monitoring applications. Group 3 encompasses potential tracers for long-term storage applications. There are six isotopes in Group 3 with half-life of 5 years or more. These isotopes are possibly best suited for historical data validations and long-term spent fuel monitoring.

a) Online burnup analysis – Candidate Isotopes

For the three applications in mind, next step is to evaluate the best isotopes for each application in regards to their physical properties; fission yield, branching ratio and gamma energies, neutron absorption cross section and diffusion parameters. Group 1 is candidate isotopes for online monitoring. Table 3 provides half-lives, emission probabilities (branching ratio), the corresponding gamma energies and fission yields (thermal neutron fission yield from uranium and plutonium) for all candidate isotopes for group 1. The last column in the table lists gamma yield (PxFY) which is the product of fission yield and emission probability and can be used as a figure of merits for an isotope's suitability as a burnup indicator. PxFY is in fact number of discrete energy gammas released per fission. Higher the PxFY is better suited the isotope would be for burnup applications. Table 3 also lists the ratio of the fission yield for ^{235}U and ^{239}Pu. This ratio is an indicator of the isotope's usefulness to be used as a discriminator between ^{235}U and ^{239}Pu.

Table 2. Candidate isotopes grouped by half-life for burnup analysis [19]

	NOT USEFUL (GROUP 0)		**ONLINE ANALYSIS (GROUP 1)**		**INTERIM STORAGE ANALYSIS (GROUP 2)**		**LONG-TERM STORAGE (GROUP 3)**	
	Less than 9 min	**($T_{1/2}$) (min)**	**10 min – 24 hours**	**($T_{1/2}$) (min)**	**24 hours- 5 years**	**($T_{1/2}$) (days)**	**5 years- more**	**($T_{1/2}$) (year)**
1	^{97m}Nb	0.9683	^{190m}Os	9.9	^{200}Tl	1.088	^{44}Ti	58.9
2	^{210}Tl	1.3	^{49}Cr	42.3	^{82}Br	1.47	^{108m}Ag	418
3	^{137m}Ba	2.55	^{204m}Pb	67.2	^{140}La	1.6785	^{166m}Ho	1200
4	^{51}Ti	5.77	^{85m}Sr	67.63	^{203}Pb	2.163	^{243}Am	7390
5			^{97}Nb	72.1	^{90}Y	2.67	^{94}Nb	20300
6			^{61}Co	99	^{111}In	2.8	^{98}Tc	4200000
7			^{132}I	137.7	^{132}Te	3.20		
8			^{90m}Y	191.4	^{67}Ga	3.26		
9			^{85m}Kr	268.8	^{87}Y	3.35		
10			^{99m}Tc	360	^{96}Tc	4.28		
11			^{73}Se	429	^{52}Mn	5.59		
12			^{157}Dy	488.4	^{56}Ni	6.075		
13			^{52}Fe	496.5	^{206}Bi	6.243		
14			^{244}Am	606	^{132}Cs	6.48		
15			^{130}I	741.6	^{131}I	8.0252		
16			^{69m}Zn	825.6	^{202}Tl	12.31		
17			^{135m}Xe	917.4	^{126}Sb	12.35		
18			^{95}Tc	1200	^{136}Cs	13.16		
19			^{133}I	1248	^{95}Nb	34.985		
20			^{43}K	1338	^{103}Ru	39.247		
21			^{200}Tl	1566	^{148m}Pm	41.3		
22					^{181}Hf	42.38		
23					^{203}Hg	46.594		
24					^{124}Sb	60.2		
25					^{95}Zr	64.032		
26					^{58}Co	70.86		
27					^{192}Ir	73.828		
28					^{194m}Ir	170		
29					^{144}Pm	363		
30					^{134}Cs	753.725		

Table 3. Group 1 fission product and decay characteristics [20, 21, 22, 23]
(Potential candidates for online measurements)

Isotope	**Half-life (mins)**	**Emission Probability (%)**	**Energy (keV)**	**^{235}U Th. Fiss. Yield**	**^{239}Pu Th. Fiss. Yield**	**FY Ratio (^{235}U/^{239}Pu)**	**PxFY (^{235}U) Gamma yield**
^{43}K	1338	86.8 79.16 11.85	372.76 617.49 396.86	N/A	N/A	N/A	N/A
^{49}Cr	42.3	53.2 30.32 16.39	90.64 152.93 62.29	N/A	N/A	N/A	N/A
^{52}Fe	496.5	99.18 1.64 0.21	168.69 377.75 1727.57	N/A	N/A	N/A	N/A
^{61}Co	99	84.67 0.79 3.62	67.42 841.7 909.2	N/A	N/A	N/A	N/A
^{69m}Zn	825.6	94.8 100.0	438.63 573.9	1.0604E-11	7.0227E-10	0.01509976	1.0053E-11 1.0604E-11
^{73}Se	429	69.84 97.0 0.27	67.07 361.2 510	5.1100E-17	2.0330E-19	251.352680	3.5688E-17 4.9567E-17 1.3797E-19
^{85m}Kr	268.8	75 0.300 0.01 14	151.195 129.81 451.0 304.87	5.8987E-05	2.3275E-05	2.53440460	4.424E-05 1.7696E-07 5.8987E-09 8.2582E-06
^{85m}Sr	67.63	96.0 97.49 1.12 0.11 0.32	151.19 231.86 129.82 731.80 238.78	1.4735E-13	2.1241E-11	0.00693691	1.4145E-13 1.4365E-13 1.6503E-15 1.6208E-16 4.7150E-16
^{90m}Y	191.4	100. 97.25 90.74 0.32	2318.97 202.53 479.51 681.8	5.2570E-08	1.1327E-06	0.04641017	5.2570E-08 5.1125E-08 4.7702E-08 1.6822E-10
^{95}Tc	1200	1.95 3.74 93.82	947.67 1073.71 765.79	8.2435E-17	2.6280E-16	0.31367960	1.6075E-18 3.0831E-18 7.7341E-17
^{97}Nb	72.1	1.09 0.15 98.23	1024.4 1268.62 657.94	1.0704E-04	6.5215E-04	0.16413044	1.1667E-06 1.5056E-07 1.0514E-04
^{99m}Tc	360	88.5 0.023	140.511 142.683	2.8512E-10	2.7839E-08	0.010241823	2.5233E-10 6.5577E-14
^{130}I	741.6	99. 96.03 82.17	536.07 668.54 739.51	1.5510E-06	3.2879E-05	0.04717187	1.5354E-06 1.4894E-06 1.2744E-06
^{132}I	137.7	98.7 75.6 17.57	667.71 772.60 954.55	1.0393E-04	1.5148E-03	0.068611905	1.0258E-04 7.8574E-05 1.8261E-05

Table 3 continued.

^{133}I	1248	0.356 0.309 1.81 0.539 0.645 1.49 0.457 1.23 4.47 0.551 1.49 2.33 86.3	262.70 422.903 510.530 617.978 680.252 706.575 768.360 856.278 875.328 1052.39 1236.44 1298.22 529.870	1.0232E-03	6.8765E-03	0.14880330	3.6427E-06 3.1618E-06 1.8521E-05 5.5153E-06 6.5999E-06 1.5246E-05 4.6762E-06 1.2586E-05 4.5739E-05 5.6381E-06 1.5246E-05 2.3841E-05 8.8306E-04
^{135m}Xe	917.4	1.47 0.1 0.07 80.8	786.9 1133.0 1358.0 526.56	1.8117E-03	7.5384E-03	0.24032192	2.6631E-05 1.8117E-06 1.2682E-06 1.4638E-03
^{157}Dy	488.4	93 0.26 1.33	326.34 83.04 182.42	2.6950E-18	1.6595E-15	0.0016239	2.5064E-18 7.0070E-21 3.5844E-20
^{190m}Os	9.9	94.88 97.79 98.62	361.2 502.5 616.5	N/A	N/A	N/A	N/A N/A N/A
^{200}Tl	1566	87.0 13.75 29.93	367.94 579.30 1205.75	N/A	N/A	N/A	N/A
^{204m}Pb	67.2	94.2 99.17 91.5	374.76 899.15 911.74	N/A	N/A	N/A	N/A
^{244}Am	606	66. 28 16.4	743.97 897.85 153.86	N/A	N/A	N/A	N/A

We have somewhat arbitrarily selected a lower limit of gamma yield per fission of 10^{-6} to identify the most attractive isotopes for burnup interrogation. For online application since the cooling time is small isotopes an isotope with lower than 10^{-6} gamma yield may still be useful, therefore we have set the gamma yield usefulness limit to 10^{-8}. At this point it is important to notice the data gaps, for many isotopes (marked as N/A – not available). For these isotopes fission yield information is either not available at all or is available with large discrepancies between the sources of information. Therefore additional work is required to evaluate the effectiveness of these isotopes as burnup indicator.

Some of the isotopes, such as ^{73}Se, ^{85m}Sr are not suited for burnup analysis because their low gamma yields (PxFY). Some of the isotopes such as ^{190m}Os have no fission yield (and hence gamma yield) available in the literature. Candidate isotopes without gamma yield values or with values below 10^{-8} are not considered suitable for online burnup analysis. ^{130}I emits a 668.54 keV photon with an emission probability of 96.03%, while ^{132}I emits a 667.1 keV photon with an emission probability of 98.7%. Because of their similar photon emission energies, distinguishing them from one another would be difficult even with high resolution spectroscopy. However, the fission yield for ^{132}I is two orders of magnitude higher than that of ^{130}I, therefore most of the gamma in this case would come from for ^{132}I (note that the emission yields of the gammas of interest are very similar). In cases where the fission yield difference is not as large, but there is significant difference in the half-lives (for example, half-life of ^{130}I is almost five times longer than ^{132}I) one would rely on standard unfolding techniques to separate the contribution from the individual peaks.

Table 4 lists thermal neutron absorption cross sections and number of production paths for group 1 candidate isotopes. Thermal neutron cross section is an important parameter for a candidate burnup analysis isotope. A large neutron cross section would mean that the isotope will exhibit large burnup history dependence. Therefore a low thermal neutron absorption cross section is desired. Moreover, any burnup indicator with large thermal neutron cross section will be lost by neutron absorption. Therefore at 2.65E+06 b, the thermal absorption cross section of ^{135m}Xe is much too high to be used as a tracer for online burnup analyses. On the other hand, ^{97}Nb and ^{132}I have an absorption cross section of 0 b; the lowest of the isotopes in Group 1 therefore making them a very attractive candidate for burnup analysis.

Table 4. Group 1 candidate isotopes thermal absorption cross section and production mode for online burnup analysis [24]

Isotope	Thermal Absorption Cross Section (barns)	Number of Production Modes
^{132}I	0.00E+00	1
^{97}Nb	0.00E+00	1
^{49}Cr	1.72E-02	2
^{61}Co	1.73E-02	1
^{85m}Kr	2.35E-02	1

Table 4 continued.

^{43}K	1.18E+00	1
^{52}Fe	1.74E+00	2
^{190m}Os	3.90E+00	1
^{90m}Y	6.50E+00	1
^{69m}Zn	7.24E+00	1
^{133}I	9.69E+00	1
^{95}Tc	1.41E+01	1
^{130}I	1.80E+01	1
^{85m}Sr	1.91E+01	1
^{200}Tl	1.95E+01	1
^{73}Se	2.18E+01	1
^{99m}Tc	2.29E+01	1
^{157}Dy	1.17E+02	1
^{244}Am	6.00E+02	1
^{204m}Pb	7.03E+02	1
^{135m}Xe	2.65E+06	1

The ideal online burnup tracer would only be produced by fission. However, two isotopes in Group 1, ^{49}Cr and ^{52}Fe, are also produced by the decay of other fission products, making them less than ideal candidates. Any burnup analysis algorithm based on an isotope with multiple production modes will show cooling time and burnup history dependence and therefore should be avoided.

Table 5 shows the diffusion properties of the Group 1 isotopes. Where possible the diffusion coefficient in UO_2 is provided, but for many candidates this information is not readily available. High diffusion rates would lead to significant migration of the isotope from its original location of birth to other areas. This migration will skew the measurement results, and will make certain sections of high burnup fuel not to be recorded appropriately. Therefore, high diffusion rates are not desirable for isotopes being considered for burnup analysis. There are significant knowledge gaps in regards to diffusion coefficients of fission isotopes. Ideally these diffusion coefficients must be measured in MOX and UO_2 fuel matrix separately at the elevated temperature comparable to fuel operating temperatures. Much of this information is missing. There is limited data on uranium diffusion and none on MOX. When UO_2 diffusion data was missing, to provide predictive data as a helpful tool diffusion coefficient in other materials is listed in table 5. For example, there is no diffusion coefficient for Os in fuel material is available, however diffusion coefficient of 1.07x10-9 cm^2/s (at 1100 ^0C) is reported in pyrrhotite ($OsPO_5$) which too varies with temperatures [25]. Reference cited in the table may be a good starting point for an interested reader to explore additional information. Needless to say that more work is needed in the area of isotope diffusion rates for many isotopes of interest. It is also difficult to predict the diffusive characteristics of MOX fuel without experimental data and how it would compare with UO_2.

Table 5. Diffusion coefficients of candidate isotopes for online burnup analysis

Isotopes	**DIFFUSION**	**Isotopes**	**DIFFUSION**
^{43}K	K in melilite : $D=1.22x10^{-16}$ cm^2/s at 900 ^0C [26]	^{99m}Tc	Tc in dense Bentonite : $D=8x10^{-7}$ cm^2/s Tc in dense metalic Molybdenum : $D=5.1x10^{-13}$ cm^2/s at 600 ^0C [44,27]
^{49}Cr	Cr in β-Uranium : $D=3.6x10^{-10}$ cm^2/s at 670 ^0C $D=6.45x10^{-11}$ cm^2/s at 680 ^0C $D=3.80x10^{-10}$ cm^2/s at 695.8 ^0C $D=5.36x10^{-10}$ cm^2/s at 712.7 ^0C [30]	^{130}I	Iodine in UO_2 : $D=5.0x10^{-14}$ cm^2/s at 1650 ^0C $D=3.0x10^{-15}$ cm^2/s at 1400 ^0C [28]
^{52}Fe	Fe in Fe_3O_4: $D=1.63x10^{-8}$ cm^2/s at 1199 ^0C $D=1.59x10^{-9}$ cm^2/s at 1200 ^0C [29]	^{132}I	Iodine in UO_2 : $D=5.0x10^{-14}$ cm^2/s at 1650 ^0C $D=3.0x10^{-15}$ cm^2/s at 1400 ^0C [28]
^{61}Co	Co in β-Uranium : $D=9.3x10^{-9}$ cm^2/s at 691.5 ^0C $D=1.16x10^{-8}$ cm^2/s at 706.3 ^0C $D=1.33x10^{-8}$ cm^2/s at 717.0 ^0C $D=1.90x10^{-8}$ cm^2/s at 741.0 ^0C [30]	^{133}I	Iodine in UO_2 : $D=5.0x10^{-14}$ cm^2/s at 1650 ^0C $D=3.0x10^{-15}$ cm^2/s at 1400 ^0C [28]
^{69m}Zn	Zn in $LiTaO_3$: $D=3.055x10^{-14}$ cm^2/s at 900 ^0C Zn in $CuInSe_2$ bulk crystal: $D=5.0x10^{-11}$ cm^2/s at 550 ^0C [31,32]	^{135m}Xe	Xe in UO_2: $D=2.5x10^{-14}$ cm^2/s at 1400 ^0C [33]

Table 5 continued.

^{73}Se	Se in PbSe : D=0.5x10^{-13} cm^{2}/s at 400 ^{0}C D=1x10^{-12} cm^{2}/s at 500 ^{0}C D=0.8x10^{-10} cm^{2}/s at 800 ^{0}C Se in Carbon steel : D=2x10^{-32} cm^{2}/s [34,35]	^{157}Dy	Dy on the W(111) facet : D=5.0x10^{-8} cm^{2}/s at 827 ^{0}C [36]
^{85m}Sr	Sr in $Bi_2Sr_2CuO_4$: D=3.4x10^{-13} cm^{2}/s at 775 ^{0}C D=1.1x10^{-11} cm^{2}/s at 800 ^{0}C Sr in Carbon steel : D=9.7x10^{-8} cm^{2}/s [34,37]	^{190m}Os	Os in Pyrrhotite($OsPO_5$) : D=1.07x10^{-9} cm^{2}/s at 1100 ^{0}C [25]
^{85m}Kr	Kr in crushed UO_2 : D=6.7x10^{-17} cm^{2}/s at 900 ^{0}C D=8.3x10^{-15} cm^{2}/s at 1100 ^{0}C [38]	^{200}Tl	Tl in KCl: D=0.8x10^{-11} m^{2}/s at 300 ^{0}C Tl in Tl Amalgam : D=0.98x10^{5} cm^{2}/s at 1200 ^{0}C [39,40]
^{90m}Y	Y in UO_2 : D=6.8x10^{-8} cm^{2}/s at 1150-1450 ^{0}C [41]	^{204m}Pb	Pb in Zircon : D=1.77x10^{-16} m^{2}/s at 1251 ^{0}C Pb in solid PbTl 50%Pb : D=1.86x10^{-12} cm^{2}/s at 206 ^{0}C [42,43]
^{95}Tc	Tc in dense Bentonite : D=8x10^{-7} cm^{2}/s Tc in dense metallic Molybdenum : D=5.1x10^{-17} m^{2}/s at 600 ^{0}C [35,44]	^{244}Am	Am in UO_2: D=4.5x10^{-11} cm^{2}/s for high O potential D=6.0x10^{-10} cm^{2}/s for low O potential [45]
^{97}Nb	Nb in UO_2: D=7.99x10^{-11} cm^{2}/s at 1096 ^{0}C D=4.82x10^{-11} cm^{2}/s at 1380 ^{0}C [41]		

b) Interim Storage (short term monitoring) – Candidate Isotopes

For interim storage analysis isotopes from third column of table 2 were selected for further analysis. Table 6 displays half-lives, emission probabilities (branching ratio), the corresponding gamma energies for all candidate isotopes for group 2. Similar to group 1, the last column in the table lists gamma yield which is the product of fission yield and emission probability and the other two columns list the ratio of the fission yield for ^{235}U and ^{239}Pu and fission yields (thermal neutron fission yield from uranium and plutonium). The data in Table 6 is used in conjunction with the data in Tables 7 and 8 to evaluate usefulness of these isotopes for spent fuel monitoring program. The criteria for isotopes in Group 2 are similar to those used for Group 1. If a candidate's gamma yield (PxFY) value is less than 10^{-8}, it is considered as unsuitable tracer for spent fuel monitoring. Several candidates were eliminated from Group 2 because of their low gamma yield (PxFY) values for example, ^{67}Ga, ^{111}In, and ^{148m}Pm. Candidate isotopes were also excluded if their gamma yield could not be determined due to lack of data, for example; ^{56}Ni and ^{203}Hg.

Table 6. Group 2 fission product and decay data [20,21,22,23]

Isotope	**Half-life (days)**	**Emission Prob. (%)**	**Energy (keV)**	**^{235}U Th. Fiss. Yield**	**^{239}Pu Th. Fiss. Yield**	**FY Ratio (^{235}U/^{239}Pu)**	**PxFY (^{235}U)**
^{52}Mn	5.59	90.0 94.5 100.0	744.23 935.54 1434.09	N/A	N/A	N/A	N/A
^{56}Ni	6.075	98.8 49.5 86. 0	158.38 749.95 811.85	N/A	N/A	N/A	N/A
^{58}Co	70.86	30.0 99.45 0.69 0.52	511.0 810.759 863.00 1674.72	N/A	N/A	N/A	N/A
^{67}Ga	3.26	38.81 21.41 16.64	93.31 184.58 300.22	1.1934E-17	2.91553E-16	0.040932523	4.6316E-18 2.5551E-18 1.9858E-18
^{82}Br	1.470	71.06 43.53 83.4	554.35 619.11 776.52	3.82137E-07	8.99942E-06	4.24624E-02	2.7155E-07 1.6634E-07 3.1870E-07
^{87}Y	3.35	82.2 89.84	388.53 484.81	3.52878E-15	1.01775E-12	0.003467237	2.9007E-15 3.1738E-15
^{90}Y	2.67	N/A 0.000001	1760.70 2186.24	3.69872E-08	7.96964E-07	0.046410126	N/A 3.6987E-16
^{95}Zr	64.032	0.27 44.27 54.38	235.69 724.193 756.729	1.27051E-03	1.25467E-03	1.01262E+00	3.4304E-06 5.6245E-04 6.9090E-04
^{95}Nb	34.985	0.03 0.01 99.808	204.12 561.88 765.803	1.06041E-06	5.65875E-06	1.87393E-01	3.1812E-10 1.0604E-10 1.0584E-06

Table 6 continued.

^{96}Tc	4.28	99.76 82.00 97.57	778.22 812.54 849.86	N/A	N/A	N/A	N/A
^{103}Ru	39.247	0.071 0.384 0.289 0.344 91.31 0.855 5.78	39.76 53.275 294.98 443.80 497.08 557.04 610.33	2.35624E-07	1.26480E-05	0.018629349	1.6729E-10 9.0480E-10 6.8095E-10 8.1055E-10 2.1515E-07 2.0146E-09 1.3619E-08
^{111}In	2.8	0.003 90.65 94.09	150.81 171.28 245.35	2.9712E-15	1.6524E-12	0.001798112	8.9136E-20 2.6934E-15 2.7956E-15
^{124}Sb	60.2	98.3 7.46 1.360 2.287 10.81 0.743 1.892 1.841 1.588 1.043 2.623 1.222 0.675 47.79 5.51	602.727 645.853 709.320 713.781 722.784 790.711 968.199 1045.128 1325.508 1355.175 1368.160 1436.561 1488.88 1690.975 2090.936	2.70379E-08	2.69957E-07	1.00156E-01	2.6578E-08 2.0170E-09 3.6772E-10 6.1836E-10 2.9228E-09 2.0089E-10 5.1156E-10 4.9777E-10 4.2936E-10 2.8201E-10 7.0920E-10 3.3040E-10 1.8251E-10 1.2921E-08 1.4898E-19
^{126}Sb	12.35	83.27 99.6 99.6	414.7 666.5 695.0	8.75506E-06	1.37397E-05	0.637208964	7.2903E-06 8.7200E-06 8.7200E-06
^{131}I	8.0252	2.607 6.06 81.2 7.26 1.796	80.185 284.305 364.48 636.989 722.911	3.90977E-05	2.29304E-04	0.170505966	1.0193E-06 2.3693E-06 3.1747E-05 2.8385E-06 7.0219E-07
^{132}Te	3.20375	14.96 1.96 88.0	49.72 116.30 228.16	1.52851E-02	2.25318E-02	0.678379002	2.2867E-03 2.9959E-04 1.3451E-02
^{132}Cs	6.48	0.75 0.96 99.45 84.48 11.94 6.88	505.79 630.19 667.71 464.47 567.16 1031.66	7.36827E-10	2.97953E-09	0.247296386	5.5262E-12 7.0735E-12 7.3277E-10 6.2247E-10 8.7977E-11 5.0694E-11
^{134}Cs	753.725	8.37 15.38 97.65 85.5 8.7 3.017	563.243 569.32 604.72 795.83 801.945 1365.186	4.43390E-08	3.85859E-06	1.14910E-02	3.7112E-09 6.8193E-09 4.3297E-08 3.7910E-08 3.8575E-09 1.3377E-09

Table 6 continued.

^{136}Cs	13.16	42.17	340.55	3.48339E-05	6.13750E-04	5.67558E-02	1.4689E-05
		99.7	818.51				3.4729E-05
		79.76	1048.07				2.7784E-05
^{140}La	1.6785	20.8	328.761	5.20771E-05	1.01954E-04	5.10790E-01	1.0832E-05
		2.995	432.513				1.5597E-06
		46.1	487.022				2.4008E-05
		4.392	751.653				2.2872E-06
		23.72	815.781				1.2353E-05
		5.58	867.839				2.9059E-06
		2.73	919.533				1.4217E-06
		7.04	925.198				3.6662E-06
		0.531	950.988				2.7653E-07
		95.40	1596.203				4.9682E-05
		0.845	2347.847				4.4005E-07
		3.412	2521.30				1.7769E-06
^{144}Pm	363	43.78	476.78	4.6662E-14	1.2900E-12	0.036172093	2.0429E-14
		98.5	618.01				4.5962E-14
		99.49	696.49				4.6424E-14
^{148m}Pm	41.3	22.2	75.8	8.78357E-11	4.03712E-08	0.002175702	1.9500E-11
		2.47	98.48				2.1695E-12
		1.10	189.63				9.6619E-13
		12.56	288.11				1.1032E-11
		3.92	311.63				3.4432E-12
		18.66	414.07				1.6390E-11
		5.35	432.78				4.6992E-12
		6.75	501.26				5.9289E-12
		94.9	550.27				8.3356E-11
		12.54	599.74				1.1015E-11
		5.48	611.26				4.8134E-12
		89.0	629.97				7.8174E-11
		32.8	725.70				2.8810E-11
		17.17	915.33				1.5081E-11
		20.3	1013.81				1.7831E-11
^{181}Hf	42.38	43.3	133.021	N/A	N/A	N/A	N/A
		5.85	136.26				
		0.86	136.86				
		15.12	345.93				
		0.703	475.99				
		80.5	482.18				
		0.233	615.17				
^{192}Ir	73.828	31.2	308.46	N/A	N/A	N/A	N/A
		86.94	316.51				
		50.26	468.07				
^{194m}Ir	170	93	328.5	N/A	N/A	N/A	N/A
		97	482.6				
		62	600.5				
^{200}Tl	1.088	87.0	367.94	N/A	N/A	N/A	N/A
		13.75	579.30				
		29.93	1205.75				
^{202}Tl	12.31	91.5	439.51	N/A	N/A	N/A	N/A
		0.59	520.3				
		0.07	960.1				

Table 6 continued.

^{203}Pb	2.163	80.9 3.35 0.75	279.2 401.32 680.51	N/A	N/A	N/A	N/A
^{203}Hg	46.594	81.48	279.2	N/A	N/A	N/A	N/A
^{206}Bi	6.243	40.79 99 66.23	516.18 803.10 881.01	N/A	N/A	N/A	N/A

Table 7 lists thermal neutron absorption cross sections and number of production paths for group 2 candidate isotopes. In this table ^{192}Ir has the highest value of absorption cross section. Similar to group 1, for storage-pool monitoring applications (group 2) low thermal neutron absorption cross section is desired. Any burnup indicator with large thermal neutron cross section will be highly dependent on burnup history. Therefore at 1.42E+03 b, the thermal absorption cross section of ^{192}Ir is much too high to be used as a tracer for online burnup analyses. On the other hand, ^{56}Ni, ^{206}Bi, and ^{203}Pb having multiple modes of production is not suitable for interim-storage monitoring applications.

Table 8 shows the diffusion properties for group 2 isotopes. Where possible the diffusion coefficient in UO_2 is provided, but for most candidates this information is not readily available. As discussed earlier, high diffusion rates are not desirable for isotopes being considered for burnup analysis. Diffusion coefficients data is provided for many of these isotopes in other materials due to limited information available in the literature. For instance, there is no diffusion coefficient within the fuel element for Ni isotope; however, data is available for Ni diffusion in copper and aluminum. The available data also shows significant temperature dependence. Diffusion coefficients in the table 8 are not sufficient and need for further research on diffusion coefficients in UO_2 and MOX fuels is obvious.

Table 7. Group 2 candidate isotopes thermal absorption cross section and production mode for storage fuel burnup analysis [24]

Isotope	Thermal Absorption Cross Section (barns)	Number of Production Modes
^{134}Cs	0.0000E+00	1
^{103}Ru	0.0000E+00	1
^{148m}Pm	0.0000E+00	1

Table 7 continued.

^{132}Te	2.0000E-03	1
^{95}Zr	1.2000E+00	1
^{140}La	2.7000E+00	1
^{90}Y	3.5000E+00	1
^{203}Hg	4.9480E+00	1
^{56}Ni	5.0230E+00	3
^{126}Sb	5.8000E+00	1
^{95}Nb	7.0000E+00	1
^{203}Pb	9.8709E+00	2
^{206}Bi	1.0400E+01	2
^{67}Ga	1.0760E+01	1
^{202}Tl	1.1402E+01	1
^{136}Cs	1.30000E+1	1
^{82}Br	1.6630E+01	1
^{124}Sb	1.7400E+01	1
^{194m}Ir	1.7600E+01	1
^{87}Y	1.8361E+01	1
^{200}Tl	1.9500E+01	1
^{96}Tc	2.35440E+1	1
^{144}Pm	3.5380E+01	1
^{132}Cs	3.7035E+01	1
^{111}In	4.3100E+01	1
^{52}Mn	5.3366E+01	1
^{181}Hf	8.0000E+01	1
^{131}I	8.0000E+01	1
^{58}Co	1.6508E+02	1
^{192}Ir	1.4212E+03	1

Table 8. Diffusion coefficients of candidate isotopes for spent fuel monitoring

Isotopes	DIFFUSION	Isotopes	DIFFUSION
^{52}Mn	Mn in CdTe: D=9.72x10^{-11} cm^2/s at 800 ^{0}C D=8.70x10^{-14} cm^2/s at 600 ^{0}C [46]	^{132}Te	Te in UO$_2$: D=1.7x10^{-12} cm^2/s at 1400 ^{0}C [47]

Table 8 continued.

^{56}Ni	Ni in copper : D=4.67x10^{-24} m^2/s at 340 ^{0}C Ni in aluminum: D: 5.12x10^{-13} cm^2/s at 450 ^{0}C [48,49]	^{132}Cs	Cs in UO$_2$: D=1.14x10^{-18} cm^2/s at 1227 ^{0}C D=1.0x10^{-17} cm^2/s at 1327 ^{0}C [50]
^{58}Co	Co in β-Uranium : D=9.3x10^{-9} cm^2/s at 691.5 ^{0}C D=1.16x10^{-8} cm^2/s at 706.3 ^{0}C D=1.33x10^{-8} cm^2/s at 717.0 ^{0}C D=1.90x10^{-8} cm^2/s at 741.0 ^{0}C [30]	^{134}Cs	Cs in UO$_2$: D=1.14x10^{-18} cm^2/s at 1227 ^{0}C D=1.0x10^{-17} cm^2/s at 1327 ^{0}C [50]
^{67}Ga	Ga in GaSb : D=3.83x10^{-18} cm^2/s at 551 ^{0}C D: 9.33x10^{-16} cm^2/s at 640 ^{0}C [51]	^{136}Cs	Cs in UO$_2$: D=1.14x10^{-18} cm^2/s at 1227 ^{0}C D=1.0x10^{-17} cm^2/s at 1327 ^{0}C [50]
^{82}Br	Br in NaCl: D=2.27x10^{-16} cm^2/s at 20 ^{0}C D=1.52x10^{-13} cm^2/s at 500 ^{0}C [52]	^{140}La	La in molten Uranium: D=4.2x10^{-7} cm^2/s at 1200 ^{0}C [53]
^{87}Y	Y in UO$_2$: D=6.8x10^{-8} cm^2/s at 1150-1450 ^{0}C [41]	^{144}Pm	Pm in Silicon: D=1x10^{-13} cm^2/s at 1100 ^{0}C D=1.5x10^{-12} cm^2/s at 1250 ^{0}C [54]
^{90}Y	Y in UO$_2$: D=6.8x10^{-8} cm^2/s at 1150-1450 ^{0}C [41]	^{148m}Pm	Pm in Silicon: D=1x10^{-13} cm^2/s at 1100 ^{0}C D=1.5x10^{-12} cm^2/s at 1250 ^{0}C [54]
^{95}Nb	Nb in UO$_2$: D=7.99x10^{-11} cm^2/s at 1096 ^{0}C D=4.82x10^{-11} cm^2/s at 1380 ^{0}C [41]	^{181}Hf	Hf in α-Zr: D=4.0x10^{-24} m^2/s at 500 ^{0}C D=1.5x10^{-20} cm^2/s at 842 ^{0}C [55]
^{95}Zr	Zr in Titanite: D=3.46x10^{-19} cm^2/s at 753 ^{0}C D=1.21x10^{-15} cm^2/s at 1050 ^{0}C [56]	^{192}Ir	Ir in Silicon : D=3.1x10^{-20} cm^2/s at 550 ^{0}C [57]
^{96}Tc	Tc in dense Bentonite : D=8x10^{-11} m^2/s Tc in dense metalic Molybolenum : D=5.1x10^{-14} cm^2/s at 600 ^{0}C [44,27]	^{194m}Ir	Ir in Silicon : D=3.1x10^{-20} cm^2/s at 550 ^{0}C [57]

Table 8 continued.

^{103}Ru	Ru in SiC: D=55x10^{-12} cm^2/s at 1850 ^{0}C D=8x10^{-12} cm^2/s at 1650 ^{0}C Ru in Aluminum: D= 5.1x10^{-10} cm^2/s at 600 ^{0}C [58,59]	^{200}Tl	Tl in KCl: D=0.8x10^{-7} cm^2/s at 300 ^{0}C Tl in Tl Amalgam : D=0.98x10^5 cm^2/s at 1200 ^{0}C [39,40]
^{111}In	In in In-Sn alloy : D=2.29x10^{-18} cm^2/s at 25 ^{0}C [60]	^{202}Tl	Tl in KCl : D=0.8x10^{-10} cm^2/s at 300 ^{0}C D=1.2x10^{-6} cm^2/s at 350 ^{0}C [39,40]
^{124}Sb	Sb in TiSi$_2$: D=3x10^{-14} cm^2/s at 550 ^{0}C D=1.3x10^{-13} cm^2/s at 600 ^{0}C D=1.5x10^{-12} cm^2/s at 700 ^{0}C [61]	^{203}Pb	Pb in Zircon : D=1.77x10^{-16} cm^2/s at 1251 ^{0}C Pb in solid PbTl 50%Pb : D=1.86x10^{-12} cm^2/s at 206 ^{0}C [42,43]
^{126}Sb	Sb in TiSi$_2$: D=3x10^{-14} cm^2/s at 550 ^{0}C D=1.3x10^{-13} cm^2/s at 600 ^{0}C D=1.5x10^{-12} cm^2/s at 700 ^{0}C [61]	^{203}Hg	Hg in Ag$_3$Sn : D=6.04x10^{-11} cm^2/s at 50 ^{0}C Hg in Ag$_2$Hg$_3$: D=1.53x10^{-9} cm^2/s at 50 ^{0}C [62,63]
^{131}I	Iodine in UO$_2$ D=5.0x10^{-14} cm^2/s at 1700 ^{0}C D=3.0x10^{-15} cm^2/s at 1400 ^{0}C [28]	^{206}Bi	Bi in nanocrystalline copper : D=2.3x10^{-15} cm^2/s at 100 ^{0}C [64]

c) Long-term storage/Historic data – Candidate Isotopes

For long-term storage monitoring application (group 3) only six isotopes were identified in table 2. Table 9 lists data aggregated from the literature to identify the best isotopes from Group 3 (5 years < $T_{1/2}$) for historical data burnup analysis. The data presented here includes the thermal fission yields from ^{235}U and ^{239}Pu, important photon emission probabilities, and corresponding gamma ray energies. Similar to the previous groups the product of fission yields and gamma emission is also listed as the figure of merit for the isotope's suitability for tracer applications. Isotopes with a gamma yield of less than 10^{-8} were not consideration useful. Unfortunately, the highest gamma yield in Table 9 (from ^{94}Nb) is still an order of magnitude below this criterion. For group 3 application long-term storage historic burnup data reconstruction it is possible to count for extended period of data and therefore lower gamma yield are acceptable. Moreover, due to long cooling time many of the interfering short lived gamma emitter would decay away making low intensity measurements possible. With this possibility in mind, thermal absorption cross sections, number of production modes and diffusion coefficients of group 3 isotopes are presented in Tables 10 and 11 respectively.

Table 9. Group 3 fission product and decay data [20,21,22,23]

Isotope	Half-life (years)	Emission Probability (%)	Energy (keV)	^{235}U Th. Fiss. Yield	^{239}Pu Th. Fiss. Yield	FY Ratio (^{235}U/^{239}Pu)	PxFY (^{235}U)
^{44}Ti	58.9	69.84 97.0 0.27	67.07 361.2 510.0	N/A	N/A	N/A	N/A
^{94}Nb	20300	99.815 99.892	702.639 871.114	1.44759E-09	9.51964E-08	1.5206E-02	1.4449E-09 1.4460E-09
^{98}Tc	4200000	100 102	652.41 745.35	8.87586E-09	4.16934E-09	2.1288E+00	8.8758E-09 9.0533E-09
^{108m}Ag	418	99.1 98.41 99.5 76.2	433.94 614.28 722.91 79.13	2.9300E-10	9.4100E-06	3.1137E-05	2.9036E-10 2.8834E-10 2.9153E-10 2.2326E-10
^{166m}Ho	1200	72 .0 54.14 56.88	184.41 711.68 810.29	9.40646E-13	1.32047E-09	7.1236E-04	6.7726E-13 5.0926E-13 5.3503E-13
^{243}Am	7390	5.89 67.20.346 0.115 0.56	43.53 74.66 86.71 141.90 117.60	N/A	N/A	N/A	N/A

The thermal absorption cross sections and number of production modes for Group 3 candidates are listed in Table 10. Several of the isotopes listed in the table have rather convoluted production path with multiple modes. For example, ^{243}Am is produced in a thermal reactor through three different paths. This makes it an unattractive candidate for burnup analysis. The same is true for ^{44}Ti which has four production paths.

Table 11 shows diffusion properties of candidate isotopes. Only Am and Nb diffusion coefficients are available in UO_2 fuel for other isotopes diffusion coefficient in other materials are reported as reference information. Ideally diffusion coefficient should be available in UO$_2$ or MOX fuel material at elevated temperature comparable to the fuel temperature in the reactor. In the absence of the desired information available data is reported as starting point. For example, diffusion coefficient for Ti is 79x10^{-14} m^2/s at 1010 ^{0}C and 0.25x10^{-14} m^2/s at 700 ^{0}C in pure copper. Significant variation with temperature is obvious from the data [65]. Data gaps are obvious stressing the need for collection of diffusion coefficient values for these isotopes in UO$_2$ and MOX fuel at high temperatures.

Table 10. Group 3 candidate isotopes thermal absorption cross section and production modes for online burnup analysis [24]

Isotopes	Thermal Absorption Cross Section (barns)	Number of Production Modes
^{243}Am	0.000000E+0	3
^{94}Nb	0.000000E+0	1
^{98}Tc	9.300000E-1	1
^{44}Ti	9.726000E-1	4
^{108m}Ag	5.070600E+1	1
^{166m}Ho	2.838660E+3	1

Table 11. Diffusion coefficients of candidate isotopes for historical data

Isotopes	DIFFUSION	Isotopes	DIFFUSION
^{44}Ti	Ti in pure copper : D=79x10^{-10} cm^2/s at 1010 ^{0}C D: 0.25x10^{-10} cm^2/s at 700 ^{0}C [65]	^{108m}Ag	Ag in SiC : D=1.0x10^{-14} cm^2/s at 1200 ^{0}C Ag in Cadmium : D=2.63x10^{-11} cm^2/s at 220 ^{0}C D=2.29x10^{-10} cm^2/s at 280 ^{0}C [66,67]
^{94}Nb	Nb in UO$_2$: D=7.99x10^{-11} cm^2/s at 1096 ^{0}C D=4.82x10^{-11} cm^2/s at 1380 ^{0}C [41]	^{166m}Ho	Ho in barium titanate : D=4.3x10^{-14} cm^2/s at 1200 ^{0}C D: 4.7x10^{-13} cm^2/s at 1400 ^{0}C [68]
^{98}Tc	Tc in dense Bentonite : D=8x10^{-7} cm^2/s Tc in dense metalic Molybolenum : D=5.1x10^{-13} cm^2/s at 600 ^{0}C [44,27]	^{243}Am	Am in UO2: D=4.5x10^{-11} cm^2/s for high O potential D=6.0x10^{-10} cm^2/s for low O potential [45]

Table 12. Candidate isotopes comparison for three burnup applications

	ONLINE ANALYSIS (GROUP 1)		INTERIM STORAGE ANALYSIS (GROUP 2)		LONG-TERM STORAGE (GROUP 3)	
	Isotope	**Remarks**	**Isotope**	**Remarks**	**Isotope**	**Remarks**
1	^{190}Os (m)	1	^{200}Tl	1,4	^{44}Ti	1,3,4
2	^{49}Cr	1,3,4	^{82}Br	5	^{108m}Ag	5*
3	^{204m}Pb	1,2	^{140}La	4*	^{166m}Ho	1,2
4	^{85m}Sr	1,4	^{203}Pb	1,3	^{243}Am	1,3
5	^{97}Nb	5	^{90}Y	1,4	^{94}Nb	5
6	^{61}Co	1,4	^{111}In	1	^{98}Tc	5*
7	^{132}I	5	^{132}Te	5		
8	^{90m}Y	4*	^{67}Ga	1		
9	^{85m}Kr	5*	^{87}Y	1,4		
10	^{99m}Tc	1	^{96}Tc	1		
11	^{73}Se	1	^{52}Mn	1		
12	^{157}Dy	1,2,4	^{56}Ni	1,3		
13	^{52}Fe	1,3,4	^{206}Bi	1,3		
14	^{244}Am	1,2	^{132}Cs	1		
15	^{130}I	5	^{131}I	5		
16	^{69m}Zn	1	^{202}Tl	1,4		
17	^{135m}Xe	2	^{126}Sb	5*		
18	^{95}Tc	1	^{136}Cs	5		
19	^{133}I	5	^{95}Nb	5		
20	^{43}K	1	^{103}Ru	5		
21	^{200}Tl	1,4	^{148m}Pm	1		
22			^{181}Hf	1		
23			^{203}Hg	1,4		
24			^{124}Sb	5*		
25			^{95}Zr	5*		
26			^{58}Co	1,2,4		
27			^{192}Ir	1,2		
28			^{194m}Ir	1		
29			^{144}Pm	1		
30			^{134}Cs	5		

Remarks – 1) Not Suitable due to low or missing gamma yield 2) Not Suitable due to high neutron x-section 3) Not Suitable due to multiple production 4) Not Suitable due to high diffusion rate 5) Suitable based on available data *) Perhaps acceptable

d) Suitable Isotopes of Burnup Monitoring

Based on the available information the three lists of candidate isotopes for the three applications; online burnup analysis, interim-storage and long-term storage were evaluated and the results is shown in table 12. The list is not in any specific order, however, the remarks may be helpful in narrowing down the choice for a certain application to a single or small group of isotopes.

Best suited candidate isotopes for three applications are listed in table 13 with gamma energies and yields. Based on the available measurement resources and the application users would have to select the gamma peaks of interest to be measured for analysis. For example, for on-line burnup analysis ^{97}Nb is identified as a good candidate with 657.94 keV (yield of 1.05E-04) and 1268.62 keV (yield of 1.50E-07). If the available measurement system does not offer good energy resolution at low energies one may have to rely on 1268.62 keV low yield peak while if high resolution system is available one could measure 657.94 keV.

Table 13. Best candidate isotopes for three burnup applications with characteristic data *) Diffusion Data not available to UO_2

	ONLINE ANALYSIS (GROUP 1)			**INTERIM STORAGE ANALYSIS (GROUP 2)**			**LONG-TERM STORAGE (GROUP 3)**		
	Isotope ($T_{1/2}$) (min)	**Gamma Energy (keV)**	**Gamma Yields**	**Isotope ($T_{1/2}$) (days)**	**Gamma Energy (keV)**	**Gamma Yields**	**Isotope ($T_{1/2}$) (years)**	**Gamma Energy (keV)**	**Gamma Yields**
1	^{97}Nb (72.1)	1268.62 657.94	1.50E-07 1.05E-04	^{82}Br* (1.47)	554.35 619.11 776.52	2.71E-07 1.66E-07 3.18E-07	^{108m}Ag* (418)	433.94 614.28 722.91 79.13	2.90E-10 2.88E-10 2.91E-10 2.23E-10
2	^{132}I (137.7)	667.71 772.60 954.55	1.02E-04 7.86E-05 1.83E-05	^{132}Te (3.20)	49.72 116.30 228.16	2.28E-03 2.99E-04 1.34E-02	^{94}Nb (20300)	702.639 871.114	1.44E-09 1.44E-09
3	^{85m}Kr (268.8)	75 0.300 0.01 14	151.195 129.81 451.0 304.87	^{131}I (8.025)	80.185 284.30 364.48 636.98 722.91		^{98}Tc* (42E+5)	652.41 745.35	8.87E-09 9.05E-09

Table 13 continued.

4	^{130}I (741.6)	536.07 668.54 739.51	1.54E-06 1.49E-06 1.27E-06	12 ^{6}Sb* (12.35)	414.7 666.5 695.0	7.29E-06 8.72E-06 8.72E-06			
5	^{133}I (1248)	262.70 422.903 510.530 617.978 680.252 706.575 768.360 856.278 875.328 1052.39 1236.44 1298.22 529.870	3.64E-06 3.16E-06 1.85E-05 5.51E-06 6.59E-06 1.52E-05 4.67E-06 1.25E-05 4.57E-05 5.63E-06 1.52E-05 2.38E-05 8.83E-04	1 ^{136}Cs (13.16)	340.55 818.51 1048.07	1.46E-05 3.47E-05 2.77E-05			
6				9 ^{95}Nb (34.98)	204.12 561.88 765.803	3.18E-10 1.06E-10 1.05E-06			
7				1 ^{103}Ru* (39.24)	39.76 53.275 294.98 443.80 497.08 557.04 610.33	1.67E-10 9.04E-10 6.80E-10 8.10E-10 2.15E-07 2.01E-09 1.36E-08			
8				11 ^{24}Sb* (60.2)	602.727 645.853 709.320 713.781 722.784 790.711 968.199 1045.128 1325.508 1355.175 1368.160 1436.561 1488.88 1690.975 2090.936	2.65E-08 2.01E-09 3.67E-10 6.18E-10 2.92E-09 2.00E-10 5.11E-10 4.97E-10 4.29E-10 2.82E-10 7.09E-10 3.30E-10 1.82E-10 1.29E-08 1.48E-19			
9				99 ^{5}Zr* (64.03)	235.69 724.193 756.729	3.43E-06 5.62E-04 6.90E-04			
10				11 ^{34}Cs (753.7)	563.243 569.32 604.72 795.83 801.945 1365.186	3.71E-09 6.81E-09 4.32E-08 3.79E-08 3.85E-09 1.33E-09			

5. Conclusions and Recommendations

The best isotopes for online burnup analysis, interim storage monitoring, and long-term storage monitoring have been investigated. Considering group 1 isotopes in table 2 and all the burnup indicator parameters that discussed before, ^{130}I, ^{132}I, ^{133}I for all corresponding energy levels are better candidate for the online burnup analysis while ^{97}Nb is also a good candidate. ^{132}I has a small (0.0686) fission yield ratio making it a good candidate for plutonium identification. But the low gamma energies from ^{132}I is would make it a bit challenging to separate the peak out from the possible noise from Compton from higher energies and other sources. The possibility of relying on 1024.4 keV from ^{97}Nb is not as attractive because of the low gamma yield of only 1.1667E-06. Therefore ^{132}I seems to be a better candidate. Because of the small difference between the emission energy from ^{130}I (668.54 keV) ^{132}I (667.71 keV) the two peaks will be practically inseparable but due to the low gamma yield of ^{130}I (1.4894E-06) as compared to ^{132}I (1.0258E-04) one can assume that the entire peak is from ^{132}I.

In short, ^{132}I seems to be a good candidate for on-line burnup analysis. Other isotopes like ^{85}Kr(m) is not as attractive due to its low emission energy (151.195 keV and 304.87 keV) and hence being prone interference. Iodine is also an attractive candidate for burnup analysis due to its low diffusion rate (~10^{-14} cm^2/s) in UO_2 at the elevated temperature. Another good candidate is ^{97}Nb at the energy level of 1024.4 keV and 657.94 keV. Even though ^{135}Xe(m) looks very good candidate given the circumstances, it has very large thermal neutron absorption cross section (2.65x10^6 barn) it will not be considered a good candidate for the analysis.

For the interim storage (short-term) monitoring there are several candidate isotopes. However, the list reduces to only a few once consideration is given to gamma yield and emission energies. The good candidate isotopes include; ^{140}La, ^{136}Cs, ^{134}Cs, ^{131}I, ^{95}Zr and ^{103}Ru. From the list ^{140}La is of particular interest due to its high emission energy (2521.30 keV) and significantly large gamma yield of (1.7769E-06). However it has a large diffusion rate (4.2E-07 cm^2/s) in molten uranium making it not so attractive. The two isotopes of cesium are well known for their usefulness as a burnup indicator and need not to be discussed. From the remaining choices, ^{131}I is an attractive option. The two energies of interest from ^{131}I are 636.98 keV and 722.91 keV with the respective yields of 2.8385E-06 and 7.0219E-07. ^{131}I also have a nonzero neutron absorption cross section make its use somewhat history dependent. ^{95}Zr is also a good candidate but it has two drawbacks. Firstly while the gamma yields are high, the emission energies are relatively low in the 700 keV range. The other issue with ^{95}Zr is the unavailability of its diffusion rate information in the fuel matrix. This knowledge gap must be filled to make use of this very attractive candidate. ^{103}Ru is potentially a good candidate for plutonium identification because of the large difference in the fission yield from uranium vs. plutonium. However, it has the same issue of missing information on the diffusion rate in UO_2. The other issue with the possible use of ^{103}Ru is the low emission energies with the maximum being 610.33keV. In short the only alternate to the use of cesium is ^{131}I isotopes for interim storage monitoring unless the data gaps are addressed for other isotopes.

There are only six isotopes for long term storage monitoring. From those six only ^{108m}Ag*, ^{94}Nb and ^{98}Tc* are viable options. ^{98}Tc has a very long half live (42E+05 yrs) which will result very low count rates. Moreover, the emission energies are also low (652.41 keV and 745.35 keV). ^{108m}Ag has a large difference in the fission yield from uranium vs. plutonium (fission yield ratio of 3.1137E-05) but its diffusion rate in UO_2 is not known and it has a nonzero absorption cross section. Therefore the only good candidate for long term storage monitoring is ^{94}Nb. It has a half-life of 20300 years with a low diffusion rate of ~10-11 cm^2/s. It has almost zero neutron absorption cross section making it burnup history independent and decent gamma yield of 1.44E-09. Based on this analysis ^{94}Nb is the only good candidate for long-term storage monitoring.

References

[1] Nuclear waste repository safe for future generations, 1663 LANL Sci/Tech Magazine. December 2008. Retrieved September 19, 2010.

[2] Nuclear Energy Institute, Plutonium and Uranium Reprocessing, http://www.nei.org/resourcesandstats/documentlibrary/nuclearwastedisposal/policybrief/advancedfuelcycle, Accessed on 13, April, 2013, Created on March 2010.

[3] Shaw Areva MOX Services, LLC, 2008, September 27. MOX Project [Online]. Available: http://www.moxproject.com/.

[4] United States Enrichment Corporation, Megatons to Megawatts Program, http://www.usec.com/news/megatons-megawatts-program-recycles-450-metric-tons-weapons-grade-uranium-commercial-nuclear-fu, Accessed on 13 April, 2013, Created on 9 July 2012.

[5] International Atomic Energy Agency, Thorium Fuel cycle-Potential benefits and challenges, IAEA-TECDOC-1450, page 1-2, May 2005, Austria.

[6] M. L. Dennis, S. Usman, “Feasibility Study of MOX Fuel Online Burnup Analysis”, Proceedings of ICAPP ’06. Reno, NV. June 2006.

[7] B.B. Bevard, J.C. Wagner, C.V. Parks, and M. Aissa, “Review of Information for Spent Nuclear Fuel Burnup Confirmation”, NUREG/CR-6998, 2009.

[8] Håkansson, A., Bäcklin, A., Hildingson, L., Danielson, N. 1993. Results of spent-fuel NDA with HRGS. In: Proceedings of the 15th Annual Esarda meeting, Rome, Italy.

[9] C. Willman, et al., “Nondestructive assay of spent nuclear fuel with gamma-ray spectroscopy”, Annals of Nuclear Energy 33, (2006), 427-438.

[10] C. Willman, et al., “A nondestructive method for discriminating MOX fuel from LEU fuel for safeguards purpose”, Annals of Nuclear Energy 33, (2006), 766-773.

[11] M. L. Dennis, S. Usman, Feasibility of 106Ru peak measurement for MOX fuel burnup analysis. Nuclear Engineering and Design, 240 (2010), 3687-3696.

[12] K.A. Jordan, G. Perret, “A delayed neutron technique for measuring induced fission rates in fresh and burnt LWR fuel”, Nuclear Instruments and Methods in Physics Research A 634, 91-100, (2011).

[13] Kiyoshi Inoue et al., “Burnup determination of Nuclear Fuel”, Mass Spectroscopy, 17, (1969), 830-842.

[14] S. Grape, et al., “Modeling Cherenkov light from irradiated nuclear fuel assemblies using GEANT4”, IAEA-CN-184/88, The IAEA Symposium on International Safeguards, Vienna, Austria, November 1-5, 2010.

[15] E. Dowdy, et al., “Method of monitoring irradiated nuclear fuel using Cerenkov radiation”, US Patent No. 4,389,568, Jun. 21, 1983.

[16] Crane, T.W., Hsue, S.T., Lee, J.C., Talbert Jr., W.L., 1978. Nondestructive assay methods for irradiated nuclear fuels. Los Alamos National Lab., Los Alamos, NM, LA-6923, pp. 2-8.

[17] A. Hawari, et.al., Assessment of Online Burnup Monitoring of Pebble Bed Reactor Fuel Using Passive Gamma Ray Spectrometry, IEEE Transaction of Nuclear Science, Vol. 49, 1249 (2002).

[18] P. Jansson, A. Håkansson, and A. Backlin, Gamma-ray Measurements of Spent PWR Fuel and Determination of Residual Power, http://jansson.net/publications/isv_7_1997.pdf, Accessed on April 2013, Created on October 1997, p.12.

[19] J. R. Parrington, et al., Nuclides and Isotopes Chart of the Nuclides Fifteenth Edition, Lockheed Martin Company, NY, 1996.

[20] “Nuclear Data Center” Japan Atomic Energy Agency, wwwndc.jaea.go.jp, Accessed April 2013, Created 1995.

[21] “Nuclear Data Services” International Atomic Energy Agency, www-nds.iaea.org, Accessed April 2013, Created 2007.

[22] “Fission Data” The Isotopes Project – Lawrence Berkeley National Laboratory, http://ie.lbl.gov/fission.html, Accessed April 2013.

[23] K. Tasaka, et al., JNDC Nuclear Data Library of Fission Products, Japan Atomic Energy Research Institute, JAERI 1287, June 3, 1983.

[24] “Evaluated Nuclear Data File (ENDF) Database” International Atomic Energy Agency, http://www-nds.iaea.org/exfor/endf.htm#1, Accessed April 2013.

[25] James M. Brenan, et al., Diffusion of Osmium in pyrrhotite and pyrite: implications for closure of the Re-Os isotopic system, Earth and Planetary Science Letters, 180, (2000), 399-413.

[26] M. Ito and J. Ganguly, Potassium diffusion in melilite; Experimental studies and constraints on the thermal history and size of planetesimals hosting CAIs, Meteoritics & Planetary Science 39, (2004), 1911-1919.

[27] I. E. Alekseev and A. E. Antropov, Accelerated Transfer of 99mTc impurity atoms at polymorphic transition in irradiated molybdenum metal, Radiochemistry, 44, (2002), 336-369.

[28] G. Stankunas, et al., Modeling the influence of nuclear fuel microstructure on fission product release, Lithuanian Journal of Physics, 46, (2006), 271-275.

[29] N. L. Peterson, W.K Chen and D. Wolf, Correlation and isotope effects for cation diffusion in magnetite, J. Phys Chem Solids, 41, (1980) 709-719.

[30] M.P Dariel, M. Blumenfeld, and G. Kimmel, Diffusion of Cobalt in BetaUranium, J. Applied Physics, 41, (1970) 1480-1483.

[31] I. Song, et al., Diffusion of Zn in stoichiometric LiTaO3, Journal of Crystal Growth, 270, (2004), 568-572.

[32] M. Benabdeslem, et al., Diffusion of Zn in CuInSe2 bulk crystals, Journal of Crystal Growth, 274, (2005), 144-148.

[33] W. Miekeley and F.W. Felix, Effect of stoichiometry on diffusion of xenon in UO2, Journal of Nuclear Materials, 42, (1972), 297-306.

[34] T.B. Caldwell, Ancillary Equipment Residual Radioactivity Estimate to support tank closure activities for F-tank farm, CBU-PIT-2005-00120, June 16, 2005.

[35] R. L. Guldi, et al., Difusion of lead and selenium in lead selenide, J. Applied Physics, 44, (1973), 4896-4907.

[36] T. Biernat, R. Blaszczyszyn, Surface diffusion of dysprosium on the W(111) facet, Applied surface science, 230, (2004), 81-87.

[37] N. Chen, et al., Diffusion of Sr in Bi2Sr2Can-1Cu2n+4, J. Mater. Res., Vol. 8, No. 10, (1993), 2465-2470.

[38] A. B. Auskern, The diffusion of krypton-85 from uranium dioxide powder, Metallurgy and ceramics, 1960.

[39] K. Gaswami, et al., Determination of the diffusion coefficient of thallium in KCl crystal by electron irradiation, Solid-state science and technology, (1980), 1855-1856.

[40] W. T. Foley, M.T.H. Liu, Tracer diffusion of thallium in thallium amalgams, Canadian Journal of Chemistry, 42, (1964), 2607-2609.

[41] J.I Federer and R.A. Padgett, Jr., Diffusion studies of 95Nb in polycrystalline UO2 between 1100 and 2100 0C, Journal of Nuclear Material, 17, (1965), 294-304.

[42] D.J. Cherniak, E.B. Watson, Pb diffusion in zircon, Chemical geology, 172, (2000), 5-24.

[43] H.A. Resing and N. H. Nachtrieb, Self-diffusion of lead, thallium and bismuth in the solid lead-thallium system, J. Phys. Chem. Solids, 21, (1961), 40-56.

[44] N.G. Sawatsky and D.V. Oscarson, Diffusion of Technetium in dense bentonite, Water, air, and soil pollution, 57-58, (1991), 449-456.

[45] I. Sato, K. Tanaka, and T. Arima, Diffusion behaviors of plutonium and americium in polycrystalline urania, Materials Science and Engineering, 9, (2010), 012005.

[46] N. Y. Jamil and D. Shaw, The diffusion of Mn in CdTe, Semicond. Science Technology, 10, (1995), 952-958.

[47] Dominique Bayen, Release of Volatile Fission Products from Uranium Dioxide-MS Thesis, University of California, Nuclear Engineering Department, 1983.

[48] A. Almazouzi, et al., Diffusion of iron and nickel in single-crystalline copper, Physical Review B, 54, (1996), 857-863.

[49] Ken-Ichi Hirano, R.P. Agarwala and Morris Cohen, Diffusion of Iron, Nickel and Cobalt in Aluminum, Acta Metallurgica, 10, (1962), 857-863.

[50] G. Busker, R.W. Grimes, M. R. Bradford, The diffusion of Iodine and caesium in the UO2±x lattice, Journal of Nuclear Materials, 279, (2000), 46-50.

[51] K. Sunder, et al., Zinc and Gallium diffusion in gallium antimonide, Physical Review B, 75, (2007), 245210-1 - 245210-9.

[52] M. Hess, et al., Diffusion constants of Br in NaCl measured by Rutherford backscattering spectroscopy, Journal of Applied Physics, 105, (2009), 124910-124915.

[53] J. Hovingh, Diffusion of Lanthanum in Molten Uranium, Department of Nuclear Engineering, University of California, Berkeley, California.

[54] D. E. Nazyrov, G. S. Kulikov, R. Sh. Malkovich, Diffusion of Promethium in Silicon, Tech. Physics Letter, 23, (1997), 68-69.

[55] F. Dyment, et al., Diffusion of Hf in α-Zr, Applied Physics A, 51, (1990), 29-33.

[56] D. J. Cherniak, Zr diffusion in titanite, Contrib Mineral Petrol, 152, (2006), 639-647.

[57] A. Rodriguez, et al., RBS characterization of the iridium diffusion in silicon, Nuclear Instruments and Methods in Physics Research B, 161-163, (2000), 663-667.

[58] K. Fukuda and K. Iwamoto, Diffusion Behavior of Fission Product in Pyrolytic Silicon Carbide, Journal of Nuclear Materials, 75, (1978), 131-144.

[59] F. Dyment, et al., Ru Self-diffusion and Ru diffusion in Al, Defect and Diffusion Forum, 237-240, (2005), 402-407.

[60] Masaharu Komiyama, et al., Diffusion coefficients of indium and tin in In-Sn alloys determined by Auger electron spectroscopy using xenon ion bombardment, Journal of Materials Science Letters, 5, (1986), 673-674.

[61] P. Gas, et al., Diffusion of Sb, Ga, Ge, and (As) in TiSi2, Journal of Applied Physics, 63, (1988), 5335-5345.

[62] T. Okabe, A. L. Hines, R.F Hochman, Diffusion of mercury in Ag3Sn, Journal of Applied Physics, 47, (1976), 49-52.

[63] P. J. Shires, A.L. Hines, and T. Okabe, Diffusion of mercury in Ag2Hg3, Journal of Applied Physics, 48, (1977), 1734-1735.

[64] H. J. Höfler, et al., Diffusion of bismuth and gold in nanocrystalline copper, Journal of Applied Physics, 74, (1993), 3832.

[65] Y. Iijima, K. Hoshino, and K. Hirano, Diffusion of Titanium in Copper, Metallurgical Transactions A, 8A, (1997), 997-1001.

[66] E. López-Honorato, et al., Silver Diffusion in Silicon Carbide Coatings, Journal of the American Ceramic Society, 94, (2011), 3064-3071.

[67] A. K. Jha, et al., Diffusion of Silver in Cadmium, Scripta Metallurgica, 6, (1972), 495-500.

[68] J. Itoh, et al., Diffusion and solubility of holmium ions in barium titanate ceramics, Journal of Materials Research, 19, (2004), 3512-3520.

III. THORIUM-BASED MIXED OXIDE FUEL IN A PRESSURIZED WATER REACTOR: A BEGINNING OF LIFE FEASIBILITY ANALYSIS WITH MCNP

Lucas P. Tucker, Ayodeji Alajo and Shoaib Usman[2]

Abstract

Thorium is an asset the nuclear industry does not use, and plutonium is a liability that much of the world would like to be rid of. By incorporating a thorium-plutonium mixed oxide fuel (Th-MOX) into the fuel cycle, pressurized water reactors could provide a means for the United States to address both of these issues – but only if key reactor safety parameters are not affected.

The feasibility of utilizing Th-MOX fuel in a pressurized water reactor is examined under steady-state, beginning of life conditions. With a three-dimensional MCNP model of a Westinghouse-type 17x17 PWR, many possibilities for replacing one-third of the UO_2 assemblies with Th-MOX assemblies were considered. The excess reactivity, critical boron concentration, and centerline axial and radial flux profiles for several configurations and compositions of a one-third Th-MOX core were compared to a 100% UO_2 core. A blanket-type arrangement of 5.5 wt% PuO_2 was determined to be the best candidate for further analysis. Therefore, this configuration was compared to a 100% UO_2 core using the following parameters: delayed neutron fraction (β_{eff}), temperature coefficient, shutdown margin (SDM), and axial and radial nuclear hot channel factors (F_Z^N and F_R^N).

The one-third Th-MOX configuration showed an undesirable reduction in β_{eff} from 0.00716 ± 4.60E-07 for the 100% UO_2 configuration to 0.00607 ± 4.30E-07. The reduction in β_{eff} would perhaps be ameliorated by the one-third Th-MOX configuration's temperature coefficient of reactivity, which at -2.05 ± 0.02 pcm $^{o}F^{-1}$ is more favorable than the corresponding value of -1.42 ± 0.02 pcm $^{o}F^{-1}$ for the 100% UO_2 configuration. The SDM of the one-third Th-MOX configuration is estimated to be 8134 ± 47 pcm, which is lower

---

[2] Correspondence to usmans@mst.edu, 225 Fulton Hall, 301 W. 14th Street Rolla, MO 65409.

than SDM of the 100% UO_2 configuration. The F_Z^N for the two cores were virtually identical. However, F_R^N for the one-third Th-MOX configuration (1.67 ± 0.28) was 20% higher than the corresponding value for the 100% UO_2 configuration (1.39 ± 0.23).

These preliminary results are encouraging. However, additional investigations are required to study the impact of thermal fluid feedback and the effect of burnup and poison buildup.

1. Introduction

Thorium represents a vast, largely untapped source of nuclear energy. Its abundance in the earth's crust is roughly three times greater than uranium [1]. Though ^{232}Th – the only naturally occurring isotope of thorium – is not fissile, it is fertile. After absorbing a neutron to become ^{233}Th and decaying to ^{233}Pa, it ultimately decays to ^{233}U [2]. Thorium-based fuels offer several potential advantages over uranium fuels: higher fissile conversion rate, higher thermal fission factor (η), lower capture-to-fission ratio, low actinide production, plutonium reduction, chemical stability, proliferation resistance [3, 4, 5, 32]. Because of these advantages, several methods for utilizing thorium fuels have been explored.

Most thorium utilization schemes require the development of advanced reactor designs. In a molten salt reactor (MSR) thorium and uranium fluorides are dissolved with the fluorides of beryllium and lithium [6]. MSRs offer some distinct advantages: they have a strongly negative temperature coefficient and allow for online refueling [6]. Also, two MSRs were designed, built, and operated at Oak Ridge National Laboratory, proving the concept and providing valuable experimental data [7, 8].

High temperature gas cooled reactors (HTGRs) are another option for thorium utilization. HTGRs would use TRISO fuel composed of pellets of thorium oxide or carbide blended with pellets of uranium oxide or carbide and coated with several layers of carbon and silicon carbide; the TRISO particles are combined in a graphite matrix and formed into either prisms or pebbles [3]. Several countries (Germany, Japan, the Russian Federation, the United Kingdom, and the United States) have built HTGRs and loaded them with thorium fuel [3]; and Tsinghua University in China is currently designing a 500 MW(th) pebble bed reactor demonstration plant [9]. HTGRs could be adapted to several fuel cycles without modification of the core or plant, but several technical hurdles remain before the technology is commercially viable [3].

An accelerator driven system is a unique reactor design in which a proton accelerator is used to produce enough spallation neutrons to bring an otherwise subcritical core to criticality [5]. Such a system would use only natural uranium and thorium fuels, eliminating the need for enrichment technology, and reducing proliferation concerns, while also achieving high burnup [10]. India has been pursuing this technology, but the design is still in the conceptual stages, and the amount of power required to operate the accelerator casts doubt on the economic viability of such a system [10, 32].

Perhaps the most expedient scheme for exploiting the world’s thorium resources is incorporating it into the current reactor fuel supply. Numerous publications have demonstrated a number of ways thorium could enhance the operation of boiling water reactors (BWRs), pressurized water reactors (PWRs), and heavy water reactors (HWRs) [3, 4, 11, 12, 13].

Thor Energy, a Norwegian company, is developing and testing thorium-plutonium BWR fuel pellets and assemblies for plutonium destruction [14, 15]. Xu, Downar, Takahashi, and Rohatgi are also studying the potential for plutonium disposition in BWRs [16] as are Mac Donald and Kazimi [17]. Francois et al. have investigated replacing all of the uranium fuel in a BWR with a thorium-uranium fuel blend [18].

Similar research on Th-Pu and Th-U fuels has been conducted for PWRs as well. Shwageraus, Hejzlar, and Kazimi have investigated the use of Th-Pu fuel in PWRs for both the destruction of plutonium [19] and improved economics [20]. Bjork et al. studied the use of Th-Pu fuel for extending the operating cycle of a PWR [21]. Trellue, Bathke, and Sadasivan have used MCNP and MCNPX to compare the reactivity safety characteristics and Pu destruction capabilities of conventional MOX fuel to those of Th-MOX fuel [22]. Their work is complemented by that of Tsige-Tamirat, who also used Monte Carlo techniques to study the effect of Th-MOX fuel on a PWR’s reactivity safety characteristics [23]. Burnup analyses of Th-MOX fuel for Pu disposition in PWRs have been performed by others: Fridman and Kliem [24].

Research on thorium utilization in HWRs has focused on both incorporating thorium rods into existing CANDU reactors [25], and, in India, developing advanced heavy water reactors specifically designed to burn thorium fuel [26].

This work focuses on incorporating thorium-plutonium mixed oxide fuel (Th-MOX) into the fleet of currently operating reactors for the purpose of plutonium disposition. The goal was to incorporate Th-MOX without changing the geometry of the core or fuel assemblies or the reactor's operational and safety characteristics. The Monte Carlo code MCNP was used to develop a three dimensional neutronic model of a 17x17 Westinghouse pressurized water reactor. For reference, a conventional cold, clean, UO_2-fueled core was modeled. Several Th-MOX fuel compositions and arrangements were considered. A core arrangement in which the outer third of the UO_2 assemblies were replaced with Th-MOX assemblies composed of 5.5% PuO_2 and 94.5% ThO_2 was identified as the most promising scenario. The following reactor characteristics were used for the analysis: excess reactivity, critical boron concentration, axial and radial flux profiles, delayed neutron fraction, temperature coefficient, shutdown margin, and axial and radial nuclear hot channel factors. These hot channel factors are routinely used in the industry to perform safety analysis.

2. Description of Reference Case: 100% UO_2

To understand the effects of incorporating Th-MOX fuel into a PWR core a conventional, UO_2 fueled reference model was developed in MCNP, and all simulations performed for characterization of the Th-MOX model were first performed on the UO_2 model. As seen in Figure 1, virtually all core structures were included. However, the upper and lower coolant nozzle on each assembly was homogenized and the grid spacers were not included. Another noteworthy approximation is that the control rods were modeled as fully withdrawn except for the shutdown margin simulation. Since the control rods were modeled as fully withdrawn, boric acid (with natural boron) was incorporated into the coolant as the control material. All other contributions to primary coolant chemistry (hydrogen, lithium, oxygen, chloride, sulfate) were ignored in this study.

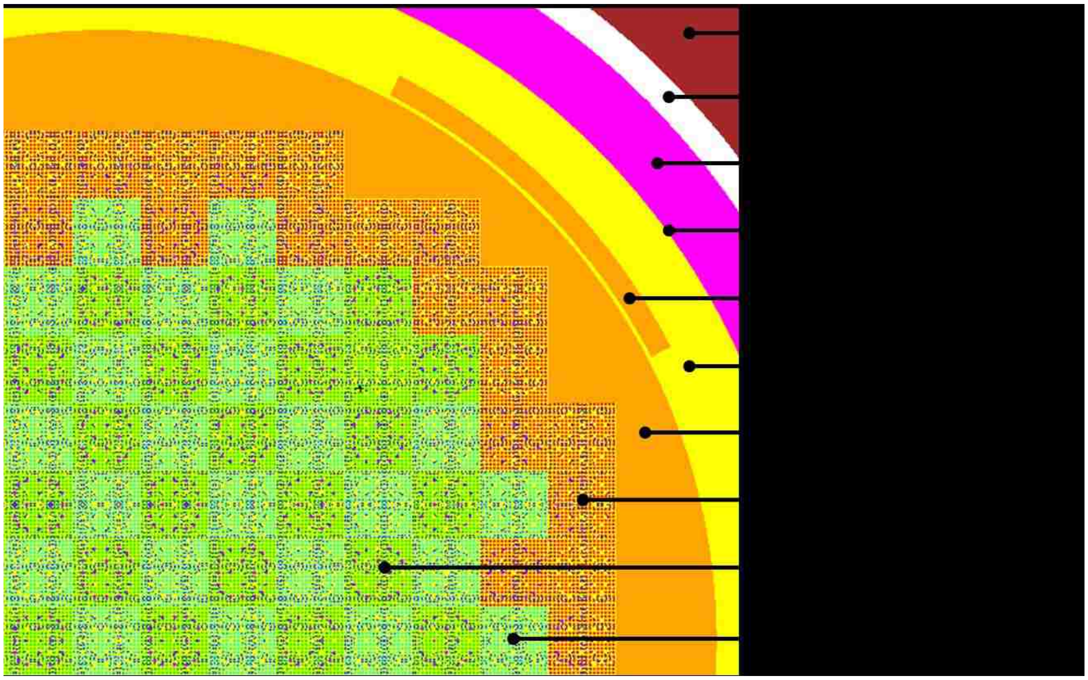

Fig. 1. Radial cross-section of core geometry showing many of the included core components.

Three fuel mixtures make up the beginning of life (BOL) core. The outer ring of fuel is enriched to 3.1% ^{235}U by weight. The inner assemblies are enriched to 2.6% or 2.1% and arranged in a checkerboard pattern. Figure 2 (a) shows the distribution of each fuel assembly type in the core. These enrichments were meant to maintain a relatively flat radial power profile and emulate depletion as fuel is burned and shuffled during its lifetime. However, the buildup of fission products and actinides was ignored.

All simulations were performed with MNCP5 Version 1.51. The ENDF-VII cross section libraries were used (unless unavailable for a particular isotope). For most problems, Two hundred million histories (2,000 KCODE cycles of 100,000 histories) were sufficient to obtain a relative error of less than 5%. All simulations were performed on a machine with eight 3 GHz processors and 8 GB of RAM.

3. Th-MOX Fuel Composition and Core Configuration Selection

During the first stage of the analysis, the fuel arrangement and fuel composition were selected. Three Th-MOX fuel arrangements were compared to each other and to the

100% UO_2 core based on their excess reactivity and critical boron concentration. Several fuel compositions were compared based on the reactor's centerline axial and radial flux profiles. However, an initial Th-MOX fuel composition was needed to examine the effect of core configuration. With this initial fuel composition the core could be configured with all of the Th-MOX fuel in the center, with a ring of Th-MOX fuel, and finally with a blanket of Th-MOX fuel replacing the 3.1% enriched UO_2 assemblies and surrounding the LEU core.

3.1. Core Configuration Analysis

Since an initial fuel composition was needed to begin the core configuration analysis, a literature review was performed, and a Th-MOX fuel composition of 7 wt% PuO_2 and 93 wt% ThO_2 was selected from the work of Shwageraus, Hejzlar, and Kazimi [19]. The isotopic composition for plutonium used in this work and shown in Table 1 was also adopted from their work.

Table 1. Isotopic composition of plutonium used for Th-MOX feasibility analysis. Adapted from Shwageraus, Hejzlar, and Kazimi [19].

Isotope	Weight Percent
^{238}Pu	3.18
^{239}Pu	56.35
^{240}Pu	26.62
^{241}Pu	8.02
^{242}Pu	5.83

The first task was to quantify the change in excess reactivity and critical boron concentration when Th-MOX fuel is incorporated into the core. To do this, the reference MCNP model of a Westinghouse PWR described in Section 2 was modified to include Th-MOX fuel and several KCODE calculations were performed while the boron concentration was varied. Two arrangements of Th-MOX fuel were compared to the 100% UO_2-fueled core. Figure 2 shows all three simulated core configurations. As previously discussed, the 100% UO_2 fueled core utilized the typical BOL loading pattern of a high enrichment (3.1%)

ring with an alternating checker board pattern of low enrichment (2.6% and 2.1%) as shown in Figure 2 (a). Figure 2 (b) demonstrates the blanket configuration of the Th-MOX fuel in which all 3.1% enriched UO_2 fuel is replaced with Th-MOX fuel. Figure 2 (c) shows the ring geometry in which some of the lower enrichment assemblies with 2.6% or 2.1% enriched UO_2 fuel are replaced, creating a ring of Th-MOX fuel in the core. For both the blanket and the ring configuration, 64 of the UO_2 assemblies (one third of the core) were replaced with Th-MOX assemblies to simulate the introduction of MOX into the current fuel cycle.

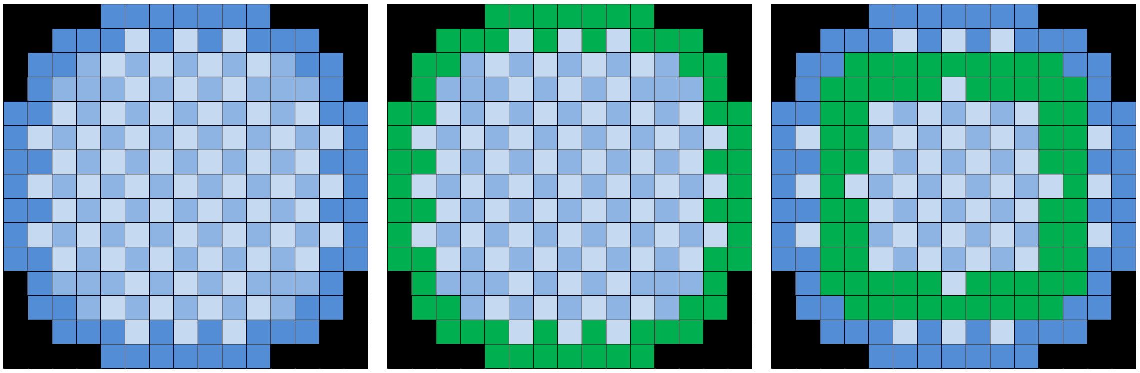
(a) (b) (c)

Fig. 2. Core loading schemes analyzed to compare a PWR fueled only with UO_2 to a PWR fueled with some Th-MOX. ■ 3.1% enriched UO_2, ■ 2.6% enriched UO_2, □ 2.1% enriched UO_2, 🟩 Th-MOX. (a) 100% UO_2, (b) Th-MOX blanket, (c) Th-MOX ring.

Figure 3 shows the results of the KCODE simulations to determine excess reactivity and critical boron concentration for the 100% UO_2 core, the Th-MOX blanket configuration, and the Th-MOX ring configuration. All three configurations yielded similar excess reactivity, but the critical boron concentration of the Th-MOX ring configuration is almost twice that of the 100% UO_2 fueled core. On the other hand, the critical boron concentration curve for the Th-MOX blanket configuration is very similar to that of the 100% UO_2-fueled core with a critical boron concentration (CBC) that is only about 100 ppm higher. The differences in excess reactivity and CBC between the 100% UO_2 configuration and the Th-MOX blanket configuration are due to the higher thermal neutron capture cross section of ^{232}Th (7.37 b [2]) compared to ^{238}U (2.68 b [2]) and higher fast fission factor of ^{239}Pu compared to ^{235}U. Though determining the fast fission factor would require considerable analysis, the relative difference between the fission factors of the two fissile isotopes can be estimated by calculating the ratio of fast fission cross section over thermal fission cross section as in Equation 1.

$$\frac{\left[\frac{\sigma_f^F}{\sigma_f^T}\right]_{Pu-239}}{\left[\frac{\sigma_f^F}{\sigma_f^T}\right]_{U-235}} \tag{1}$$

This ratio is 1.035; meaning that for a given flux one would expect a higher fast fission factor for Pu. The Th-MOX blanket configuration was selected for all future analysis in order to match the performance of the 100% UO_2 core as closely as possible. The last configuration of Th-MOX considered was an annulus of UO_2 fuel surrounding 64 Th-MOX assemblies in the center of the core. However, based on the results from the blanket and ring configurations it was concluded that the UO_2 annulus would require much higher initial boron concentration making it undesirable for any transition to Th-MOX fuel.

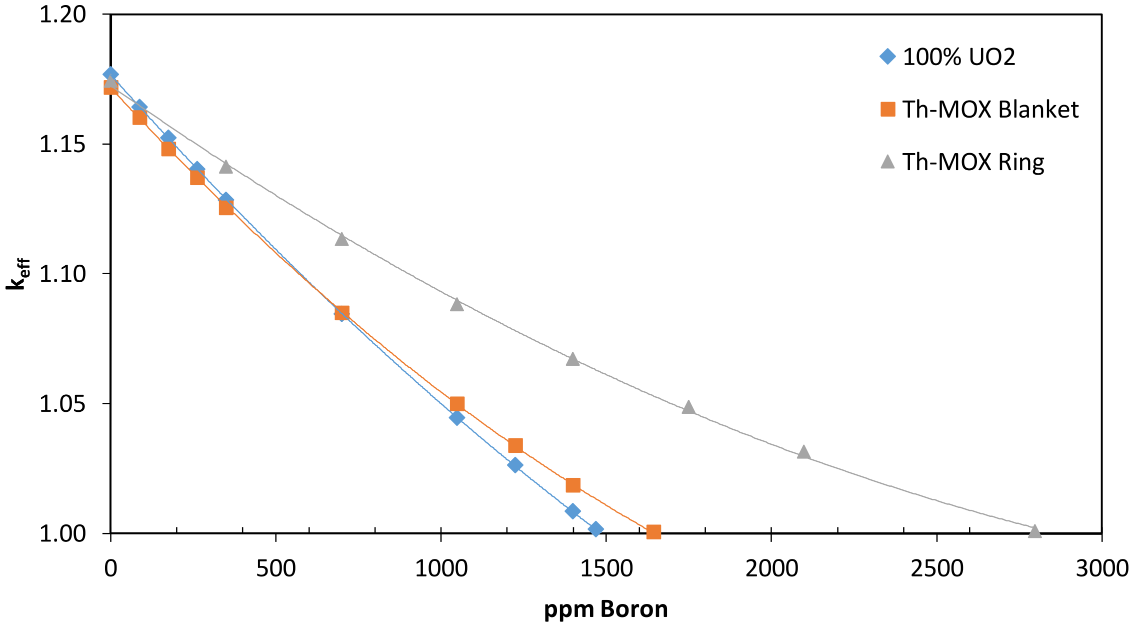

Fig. 3. The effective multiplication factor of a 17x17 PWR core as a function of ^{10}B concentration for the 100% UO_2, Th-MOX blanket, and Th-MOX ring fuel configurations detailed in Fig. 2.

3.2. *Fuel Composition Analysis*

After selecting the Th-MOX blanket configuration, the optimum fuel composition was determined. Centerline radial and axial flux profiles were generated for a range of PuO_2 contents between 5% and 7% by weight as seen in Figure 4. Based on error analysis, 5.5 wt% PuO_2 had the smallest percent difference relative to the 100% UO_2 configuration for both the radial and axial flux profiles.

In Figure 5 the radial and axial flux profiles of the 100% UO_2 and 5.5 wt% PuO_2 Th-MOX blanket configurations are compared. The axial flux profiles are almost identical. Though similar, the radial flux profile of the Th-MOX configuration slightly deviates from the 100% UO_2 configuration approximately 130 cm from the center of the core, which is the beginning of the Th-MOX assemblies.

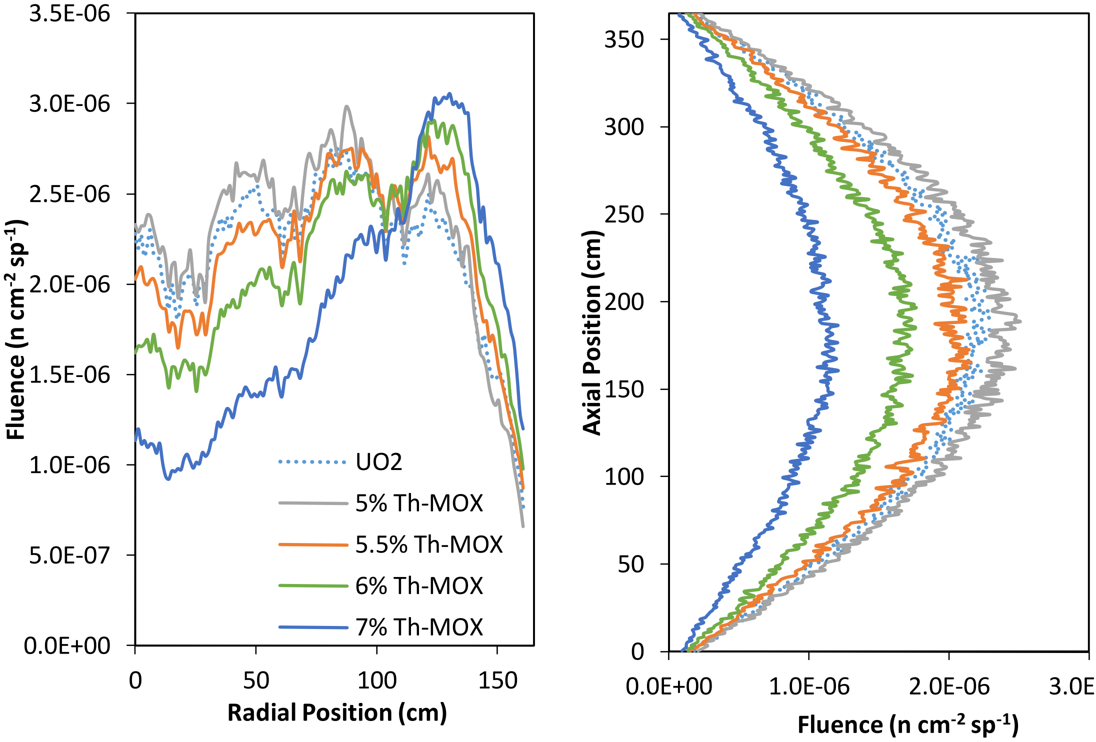

(a) (b)

Fig. 4. Flux profile comparisons of 5% to 7% PuO_2 Th-MOX blanketed core and 100% UO_2 core. (a) Radial. (b) Axial.

After 5.5 wt% PuO_2 was found to be the best fuel composition, the analysis of excess reactivity and critical boron concentration was repeated to ensure the blanket configuration with 5.5 wt% remained the configuration most similar to the 100% UO_2 configuration. Table 2 shows the results of this analysis. Though the excess reactivity of the Th-MOX Ring configuration with 5.5 wt% PuO_2 was actually closer to that of 100% UO2, the CBC remains substantially (680 ppm) higher. The CBC of the 5.5 wt% PuO_2 Th-MOX blanket configuration was only 15 ppm higher than that of the 100% UO_2 configuration. Therefore, the blanket configuration remained the recommended configuration.

Based on the results of the simulations to determine excess reactivity, critical boron concentration, and the radial and axial flux profiles, it can be concluded that if Th-MOX assemblies were to be introduced into the existing fleet of PWRs the blanket configuration with fuel composed of 5.5 wt% PuO_2 would most closely match the performance of the 100% UO_2 core. For all subsequent analyses in this work, this configuration and composition was used.

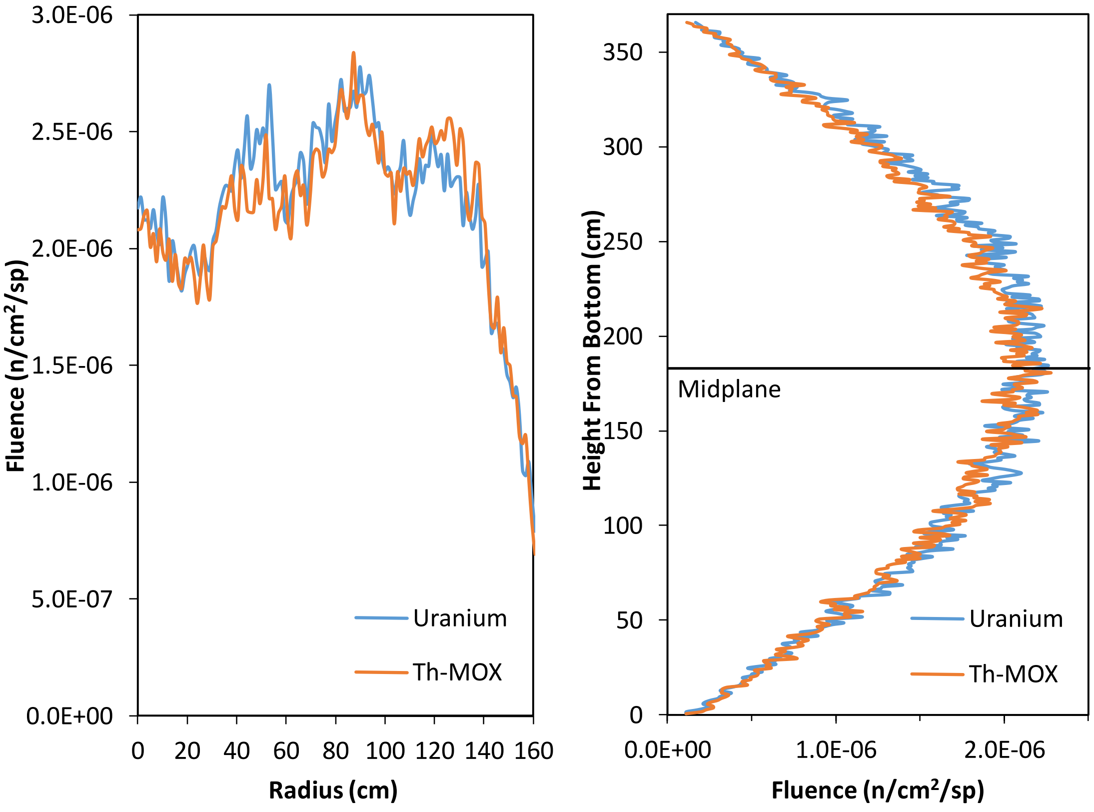

(a) (b)

Fig. 5. Flux profile comparison of 5.5% PuO_2 Th-MOX blanketed core and 100% UO_2 core. (a) Radial. (b) Axial.

Table 2. Excess reactivity in pcm and critical boron concentration in ppm for all simulated core configurations and fuel compositions

Configuration	Excess Reactivity (pcm)	Critical Boron Concentration (ppm B)
100% UO_2	14785 ± 20	1290
7% Th-MOX Blanket	14381 ± 28	1452
5.5% Th-MOX Blanket	14200 ± 30	1305
7% Th-MOX Ring	17425 ± 21	2798
5.5% Th-MOX Ring	14912 ± 29	1970

4. One-Third Th-MOX Core Reactor Safety Metrics

With the least disruptive Th-MOX fuel composition and configuration identified by determining the excess reactivity, critical boron concentration, and radial and axial flux profiles, several reactor safety parameters were investigated for the Th-MOX blanket configuration with 5.5 wt% PuO_2. The safety parameters investigated here were delayed neutron fraction, temperature coefficient of reactivity, control rod worth and shutdown margin, and the axial and radial nuclear hot channel factors.

4.1. Delayed Neutron Fraction

Since a smaller delayed neutron fraction (β_{eff}) reduces the reactor's controllability, β_{eff} is an important parameter to investigate. To determine the delayed neutron fraction, two KCODE simulations were performed at 600 K for each configuration and fuel composition. In the first simulation, both delayed neutrons and prompt neutrons were generated and tracked yielding the total multiplication factor. In the second simulation, only prompt neutrons were generated and tracked, yielding the prompt multiplication factor. Using results of these two simulations the effective delayed neutron fraction could be determined from Equation 2 [27]:

$$\beta_{eff} \cong 1 - \frac{k_p}{k} \tag{2}$$

These simulations were performed for the 100% UO_2 and Th-MOX blanket configuration. For the Th-MOX blanket configuration two fuel compositions were used: 5.5 wt% PuO_2 and 7 wt% PuO_2. Results are shown in Table 3 with each configuration's values for excess reactivity and critical boron concentration. For a core with one third 5.5 wt% PuO_2 Th-MOX assemblies β_{eff} is slightly lower than the corresponding value for the 100% UO_2 core but it is higher than the β_{eff} for 7 wt% Th-MOX. This finding, together with its lower excess reactivity and CBC, indicates that 5.5 wt% Th-MOX fuel in blanket configuration is the better choice than 7 wt% PuO_2 Th-MOX. In both cases, β_{eff} is lower for the Th-MOX configuration than the 100% UO_2 configuration suggesting that Th-MOX core will be slightly more difficult to control than the 100% LEU core.

Table 3. Reactor fuel parameters for 100% UO_2 core, one-third 5.5% PuO_2 Th-MOX blanketed core, and one-third 7% PuO_2 Th-MOX blanketed core

Fuel Arrangement	β_{eff}	Excess Reactivity (pcm)	Critical Boron Concentration (ppm)
100% UO_2	0.00716 ± 4.60E-07	14785 ± 20	1290
5.5% PuO_2 Th-MOX	0.00607 ± 4.30E-07	14200 ± 30	1305
7% PuO_2 Th-MOX	0.00545 ± 1.65E-06	14381 ± 28	1452

4.2. *Temperature Coefficients of Reactivity*

Another important reactor safety parameter is the temperature coefficient (α_T), which quantifies the effects of temperature changes on reactivity. Equation 3 shows how the temperature coefficient is calculated [28].

$$\alpha_T = \frac{1}{k^2}\frac{dk}{dT} \tag{3}$$

Typically, a negative α_T is both desired and required by the Nuclear Regulatory Commission (NRC). However, at beginning of life the NRC does allow most plants to have a slightly positive α_T. For the Westinghouse PWR simulated for this project an α_T up to 5 pcm/°F is allowed [29].

To determine the temperature coefficient of each core configuration three MCNP simulations were performed. The first simulation was performed with room-temperature cross sections for coolant and fuel (293.6 K, typically the 70c ENDF-VII libraries). Water density was 1 g cm^{-3}, and the critical boron concentration for each configuration was used. A KCODE with 5,000 active cycles of 40,000 particles was run under these conditions to determine the effective multiplication factor (k_{eff}) as an initial point for calculating both the overall coefficient of reactivity and the fuel coefficient of reactivity. The second simulation was performed with cross sections at the PWR operating temperature for both the coolant and fuel (600 K, typically the 71c ENDF-VII libraries). A reduced coolant density of 0.711 g cm^{-3} was applied, which automatically resulted in reduced boron number density. A KCODE with 5,000 active cycles of 40,000 particles was run under these conditions to determine the overall coefficient of reactivity. The final simulation was performed with elevated fuel temperature (600 K) cross sections and room temperature (293.6 K) coolant cross sections and density. The purpose of this last simulation was to separately determine the fuel coefficient of reactivity.

All three simulations were performed for the 100% UO_2 configuration and the 5.5 wt% PuO_2 Th-MOX blanket configuration. The results of these simulations are plotted in Figures 6 and 7. As shown in Figure 6, the overall temperature coefficient of reactivity for the 100% UO_2 configuration is approximately 1.5094E-05 ± 2.2857E-07 Δk/K (or 0.83863 ± 0.02286 pcm/°F), while the 5.5 wt% PuO_2 Th-MOX blanket configuration is approximately -3.4051E-05 ± 2.3355E-07 Δk/K (-1.8917 ± 0.02335 pcm/°F).

For various safety reasons NRC pays particular attention to the fuel temperature coefficient of reactivity [30]. Therefore, the fuel coefficient of reactivity was estimated by running a simulation with room temperature moderator but with fuel cross sections at elevated temperature. These results for both 100% UO_2 and 5.5 wt% PuO_2 fuel are shown in Figure 7. It is important to note that for both fuels, these coefficients were negative as required by NRC. As shown in Figure 7, the fuel temperature coefficient of reactivity for the 100% UO_2 configuration was -2.5648E-05 ± 2.3432E-07 Δk/K (or -1.42491 ± 0.02343 pcm/°F), while it was -3.6922E-05 ± 2.3395 Δk/K (-2.05122 ± 0.02339 pcm/°F) for the 5.5

wt% PuO_2 Th-MOX blanket configuration. These results suggest that introducing Th-MOX fuel into a PWR fuel cycle would not negatively impact the reactor's temperature coefficient.

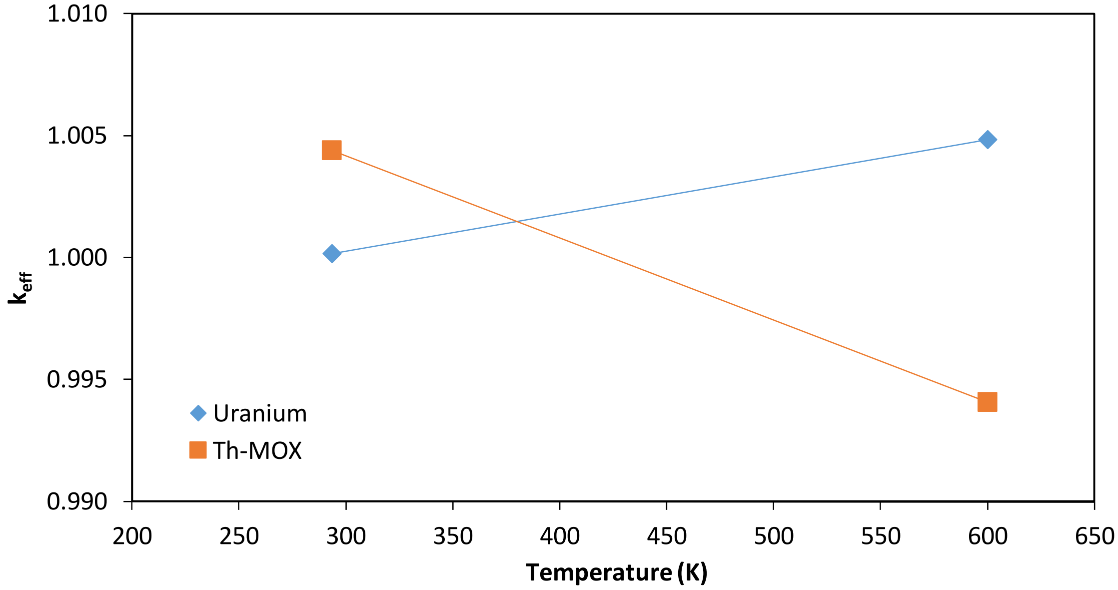

Fig. 6. Total temperature coefficient data for the 100% UO_2 core and the 5.5% PuO_2 Th-MOX blanketed core

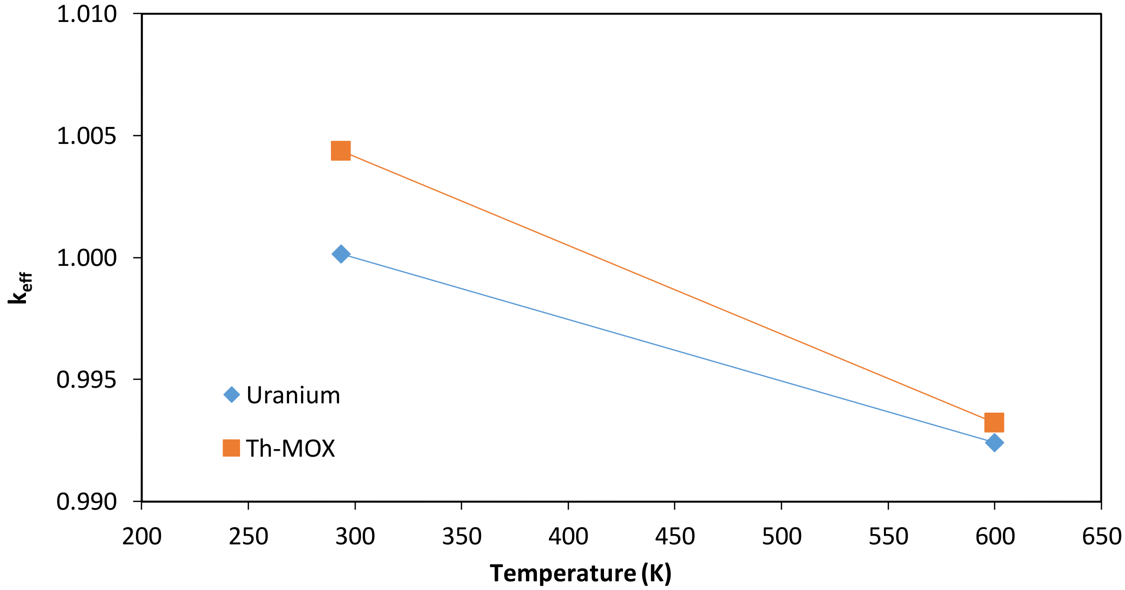

Fig. 7. Fuel temperature coefficient data for the 100% UO_2 core and the 5.5% PuO_2 Th-MOX blanketed core

4.3. Control Rod Worth and Shutdown Margin

A safety analysis of any reactor will invariably include determination of the control rod worth and shutdown margins. In order to comply with regulatory requirements, the shutdown margin of a reactor with Th-MOX fuel must be comparable to that of a 100% UO_2 fueled core. A reactor core's reactivity is the algebraic sum of many contributing factors, and so its control rod worth depends on many factors as well. Control rod calibrations are part of routine operation; each time fuel is shuffled or fresh fuel is added, the control rods must be calibrated. However, the calibration is dynamic in that as fuel is consumed and fission products build up during operation, the neutron flux at the location of a rod may have changed significantly, and, consequently, the rod worth will have changed as well. Likewise, boron concentration in the coolant and the thermal feedback of the moderator will also have a profound effect on rod worth. In general, rod worth can be expressed as:

$$\rho_{Rod} = \rho_{Fuel} - \rho_{Boron} - \rho_{Xe} - \rho_{Sm} - \rho_{Mod} \tag{4}$$

Where ρ_{Fuel} is the excess reactivity of the fuel, ρ_{Boron} is the negative reactivity of the boron in the coolant and ρ_{Mod} is the negative reactivity feedback from density changes of the moderator. The remaining two terms, ρ_{Xe} and ρ_{Sm}, represent the negative reactivity introduced by xenon and samarium buildup – the two dominant fission product poisons.

The process of determining control rod worths began with a KCODE simulation with all control rods fully inserted. To determine the worth of each rod a separate KCODE simulation would have to be performed with each rod withdrawn, one-by-one. However, taking advantage of the symmetry of a PWR, control rod worth only needed to be determined for one quarter of the reactor's rods. Therefore, KCODE simulations were performed with each full-length control rod in the northeast quadrant of the core fully withdrawn, one-by-one, to identify the highest worth rod. Figure 8 provides a map of the control rods that were analyzed.

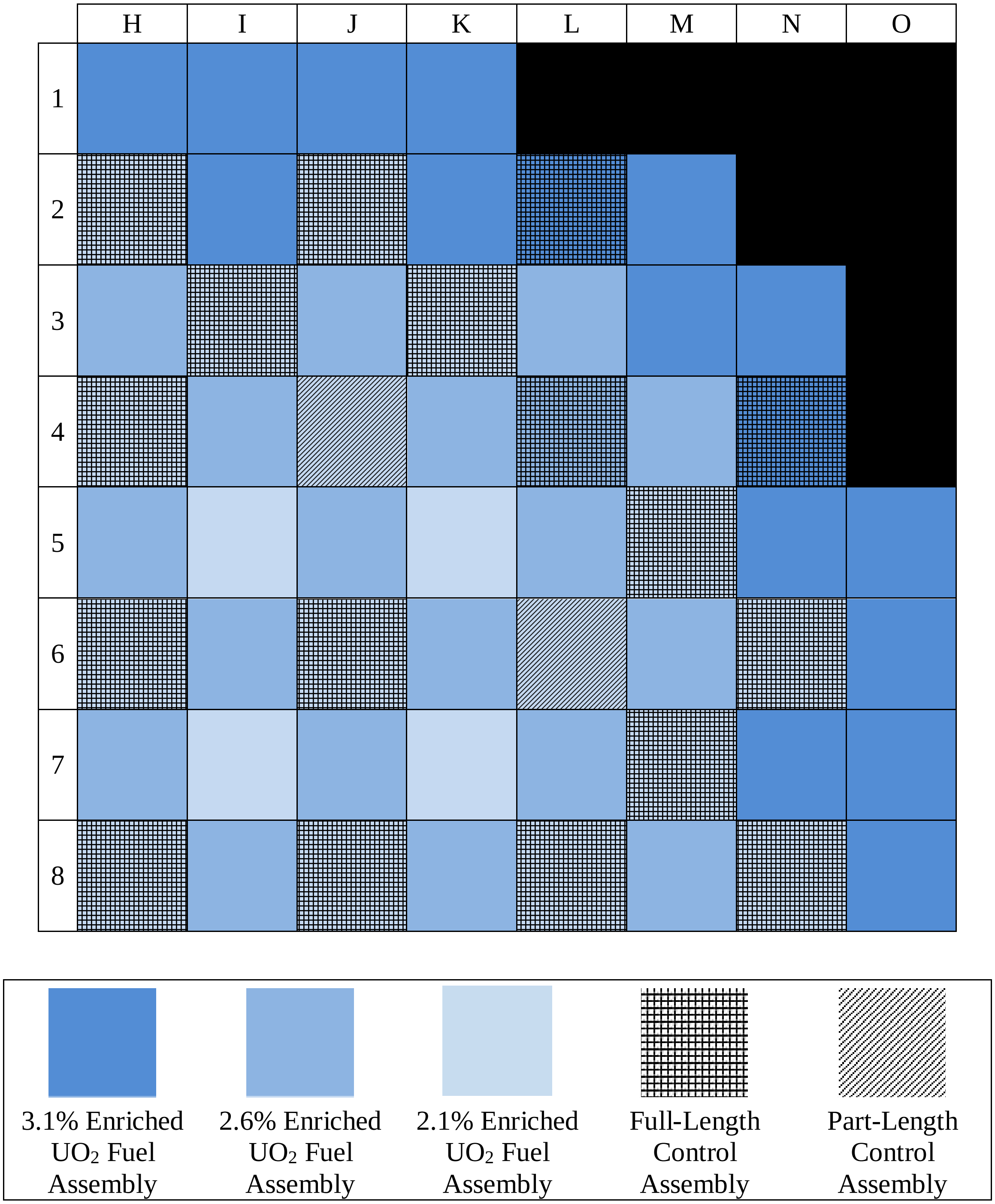

Fig. 8. Map of assemblies analyzed for control rod worth and shutdown margin simulations. The various fuel enrichments are distinguished by their color, while the part-length and full-length control assemblies are distinguished with shading. These assemblies are in the northeast quadrant of the core.

Shutdown margin (SDM) is defined by the NRC as the instantaneous amount of reactivity by which the reactor is subcritical – or would be subcritical from its present condition – assuming all control rods are fully inserted except the highest worth rod, which is fully withdrawn. Shutdown margin can be represented algebraically by Equation 5:

$$SDM = |\rho_{Rod}| - |\rho_{Mod}| - |\rho_{Fuel}| \tag{5}$$

The variable ρ_{Rod} was determined by the aforementioned control rod worth simulations. However, since these simulations did not account for the buildup of poison, the predicted rod worth as well as the shutdown margins were expected to be slightly higher compared to a core with poison present. The results of the simulations – both control rod worth and shutdown margin – are provided in Table 4.

Table 4. This table provides the control rod worths for the control assemblies that were analyzed in both the 100% UO_2 configuration and the Th-MOX blanket configuration and each configuration's SDM. The reactivity of the highest worth rod is shaded.

Stuck	100% UO_2		Th-MOX	
Rod	ρ (pcm)	σ (pcm)	ρ (pcm)	σ (pcm)
H2	830	33	1914	5
H4	395	30	148	31
H6	408	30	144	30
H8	264	28	87	30
I3	254	29	296	29
J2	871	31	1829	5
J6	847	31	265	30
J8	470	29	65	31
K3	345	28	484	31
L2	724	31	800	33
L4	1156	5	784	29
L8	377	28	214	32
M5	392	30	443	30
M7	273	29	311	31
N4	839	31	886	35
N6	953	31	1603	34
N8	775	32	301	31
SDM (pcm)	8804	40	8134	47
SDM (%Δk/k)	8.804%	0.040%	8.134%	0.047%

SDM was calculated to be 8804 ± 40 pcm for the 100% UO_2 configuration and 8134 ± 47 pcm for the Th-MOX configuration. Both values are well above the 1300 pcm required by the NRC, but the reduction in SDM for the one-third Th-MOX configuration is concerning. It would be possible to ameliorate this deficit by increasing the worth of the control rods (e.g. increasing boron-10 content). Again, burnup and fission product buildup have been ignored for these simulations; therefore, the actual SDM would be higher than what was predicted here.

4.4. Nuclear Hot Channel Factors

It is important that replacing the outer third of a PWR's UO_2 assemblies with Th-MOX assemblies does not dramatically change the core's power distribution or induce hot channel factors beyond prescribed limits. There are strict regulatory requirements concerning flux and power distributions in power reactors. Likewise, to ensure that there is no risk of fuel melting, the fuel centerline temperature must be kept well within the melting temperature of the fuel. This requirement is met by ensuring the critical heat flux is never reached. In order to find the critical heat flux, two hot channel factors are required: the nuclear axial hot channel factor ($\mathrm{F_Z^N}$) and the enthalpy rise hot channel factor ($\mathrm{F_{\Delta h}}$) as seen in Equation 6.

$$q_c'' = q_{av}'' \, F_Z^N \, F_{\Delta h} \tag{6}$$

$\mathrm{F_Z^N}$ is defined as the ratio of the maximum heat flux in the hot channel to the average heat flux in the hot channel (see Equation 7).

$$F_Z^N = \frac{Estimated\ maximum\ heat\ flux\ in\ hot\ channel}{Mean\ heat\ flux\ in\ hot\ channel} \tag{7}$$

$\mathrm{F_{\Delta h}}$ is the enthalpy rise in the hottest channel over the enthalpy rise in the average channel [31]. $\mathrm{F_{\Delta h}}$ accounts for both the radial nuclear hot channel factor ($\mathrm{F_R^N}$) and the engineering enthalpy rise hot channel factor ($\mathrm{F_{\Delta h}^E}$);

$$F_{\Delta h} = F_R^N F_{\Delta h}^E \tag{8}$$

The radial nuclear hot channel factor ($\mathrm{F_R^N}$) is the mean heat flux in the hot channel over the mean heat flux in the average channel of the core (see Equation 9).

$$F_R^N = \frac{Mean\ heat\ flux\ in\ hot\ channel}{Mean\ heat\ flux\ in\ average\ channel\ of\ the\ core} \tag{9}$$

However, one would be required to perform a detailed thermal hydraulic analysis of the core to determine the engineering enthalpy rise hot channel factor which would include the core flow subfactor and core mixing subfactor. Additionally, there are fuel fabrication uncertainties associated with the enrichment, density and geometry of the fuel, all of which are accounted for in the engineering hot channel factor, F_Q^E. In the absence of information regarding engineering enthalpy rise hot channel factor ($F_{\Delta h}^E$) and the engineering hot channel factor (F_Q^E), only nuclear hot channel factors can be compared to assess the relative safety of incorporating Th-MOX fuel into a PWR core.

Though calculating the engineering enthalpy rise hot channel factor ($\mathrm{F_{\Delta h}^E}$) was outside the scope of this work, it was possible to estimate the axial and radial nuclear hot channel factors by approximating heat flux with thermal neutron flux. Thermal neutron flux can be used to approximate heat flux in a thermal reactor because the rate of fission and hence energy production is directly related to the thermal neutron population. However, a portion of the thermal reactor’s power is produced by fast fission (typically about 8%), which will introduce some error to the nuclear hot channel factor results presented here – particularly for the Th-MOX core which, as previously mentioned, has a higher fast fission factor.

To find the axial and radial nuclear hot channel factors, several thermal neutron flux tallies were generated with MCNP for both the 100% UO_2 configuration and the 5.5 wt% PuO_2 Th-MOX blanket configuration. First, taking advantage of the symmetry of the PWR core, the northeast quadrant (56 assemblies) was tallied on an assembly-by-assembly basis in sixteen vertical sections. This data was used to generate sixteen flux maps of the core, examples of which can be seen in Figure 9. The thermal neutron flux per source particle for each vertical section of each assembly was recorded according to its location in the core and color coded according to its magnitude. The data from these sixteen flux maps were totaled to determine which assembly had the highest neutron flux and thus the highest power production (hottest assembly). These results are shown in Figure 10. For both the 100% UO_2 configuration and the 5.5 wt% PuO_2 Th-MOX blanket configuration, assembly H4 (midpoint at x = 0 cm, y = 86.0 cm) was the hottest assembly.

Subsequently, a pin-by-pin analysis of assembly H4 was then performed for both fuel configurations. The assembly was divided into seventeen vertical sections and thermal neutron flux was tallied in the fueled channels. Water-filled channels were ignored. The results of this analysis were used to generate seventeen flux maps of assembly H4. Examples of these results can be seen in Figure 11. Each channel's flux was summed across each vertical section to determine the hot channel. Figure 12 displays the results. For the 100% UO_2 configuration the channel centered at (x = 3.8 cm, y = 83.5 cm) was hottest, while the channel centered at (x = 3.8 cm, y = 91.1 cm) was the hottest channel in the 5.5 wt% PuO_2 Th-MOX blanket configuration.

The neutron tally results for each of the seventeen vertical sections in the hot assembly were averaged to obtain the mean heat flux in the hot channel. The highest neutron flux was observed in the middle section as expected. This value was divided by the mean neutron flux of the entire hot channel to obtain the nuclear hot channel factors for each configuration: $[F_Z^N]^{UO2}$ and $[F_Z^N]^{Th-MOX}$, respectively.

$$F_Z^N = \frac{\phi_{max}}{\phi_{ave}} \approx \frac{\phi_9}{\frac{1}{17}\sum_{i=1}^{17} \phi_i} \tag{10}$$

$[F_Z^N]^{UO2}$ was found to be 1.47 ± 0.24 and $[F_Z^N]^{Th-MOX}$ was 1.49 ± 0.25. The relative difference between these two values is small and within one standard deviation suggesting the difference is statistically insignificant, and, hence, adopting the 5.5 wt% PuO_2 Th-MOX blanket configuration would not cause significantly higher vertical heat flux peaking.

Subsequently, the nuclear radial hot channel factor was considered. To determine the radial hot channel factor, thermal neutrons were tallied and averaged for each assembly in the northeast quadrant of the core, and the assembly with the maximum thermal neutron flux was identified. Dividing the maximum flux by the average provided the initial approximation of F_R^N.

$$[F_R^N]_{initial} = \frac{\frac{1}{17}\sum_{i=1}^{17}\phi_i^{hot}}{\frac{1}{17}\sum_{i=1}^{17}\phi_i^{avg}} \tag{11}$$

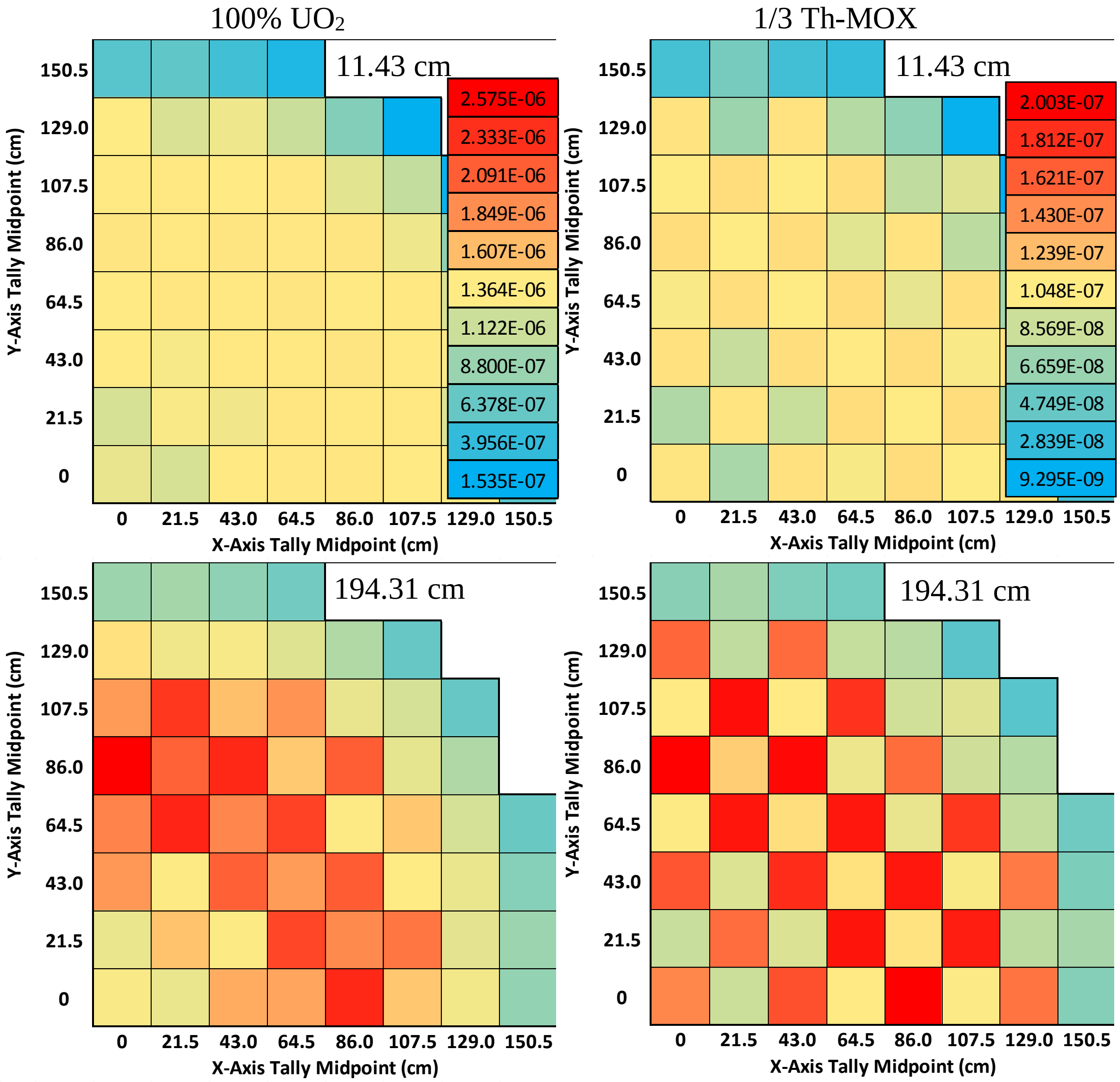

Fig. 9. Heat maps of the assembly-by-assembly thermal flux tally results for one quarter of each core from vertical sections 1 and 9. Results from the 100% UO$_2$ core are in the left column, and results from the 1/3 Th-MOX core are on the right.

However, the estimated value needed additional correction to account for the fact that within the hottest assembly neutron flux – and consequently heat flux – varies by channel. Therefore, additional simulations were performed to acquire pin-by-pin tallies for the hot assembly. The ratio of the flux of the hottest pin divided by the mean pin flux was used as a correction factor. This ratio was multiplied by the result of Equation 10 to arrive at the final value for F_R^N as seen in Equation 11.

$$F_R^N \approx \frac{\phi_{pin}^{max}}{\phi_{pin}^{avg}} [F_R^N]_{initial} \tag{12}$$

The radial nuclear hot channel factor for the 100% UO$_2$ configuration ($([F_R^N]^{UO2})$) was found to be 1.39 ± 0.23, whereas for the 5.5 wt% PuO$_2$ Th-MOX blanket configuration the corresponding value ($([F_R^N]^{Th-MOX})$) was found to be 1.67 ± 0.28. Because $[F_R^N]^{Th-MOX}$ is slightly higher, additional safety analysis may be required to ensure that all safety requirements are fulfilled before Th-MOX can be introduced into an existing PWR.

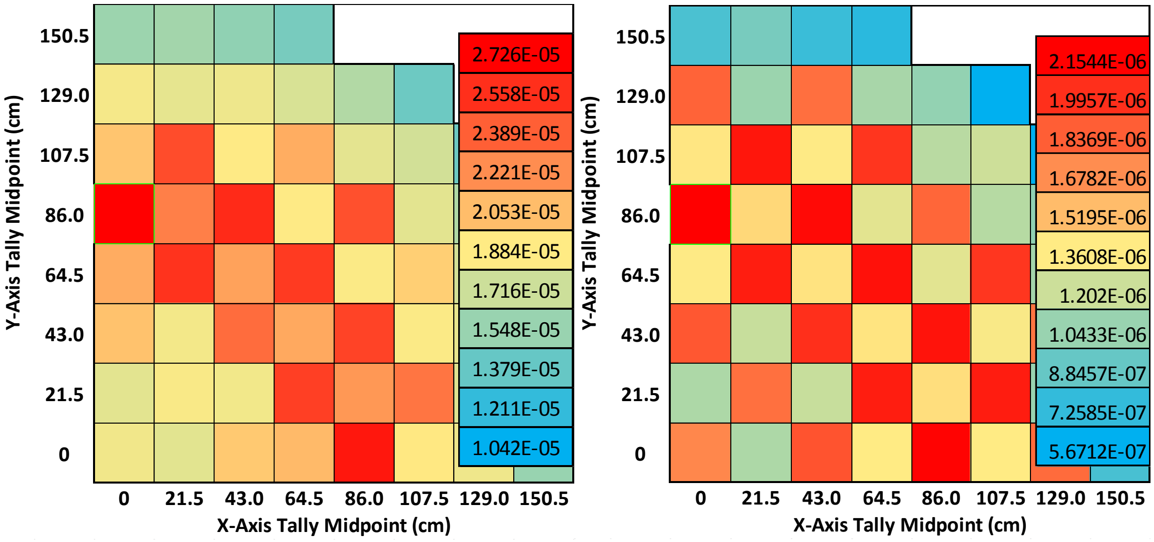

(a) (b)

Fig. 10. Heat maps of the total assembly-by-assembly thermal flux tally results summed over all 16 vertical sections for one quarter of the core in each fuel configuration. For both configurations the peak assembly is H4, the midpoint of which is located at (x = 0 cm, y = 86.0 cm). (a) 100% UO$_2$ (b) 1/3 Th-MOX

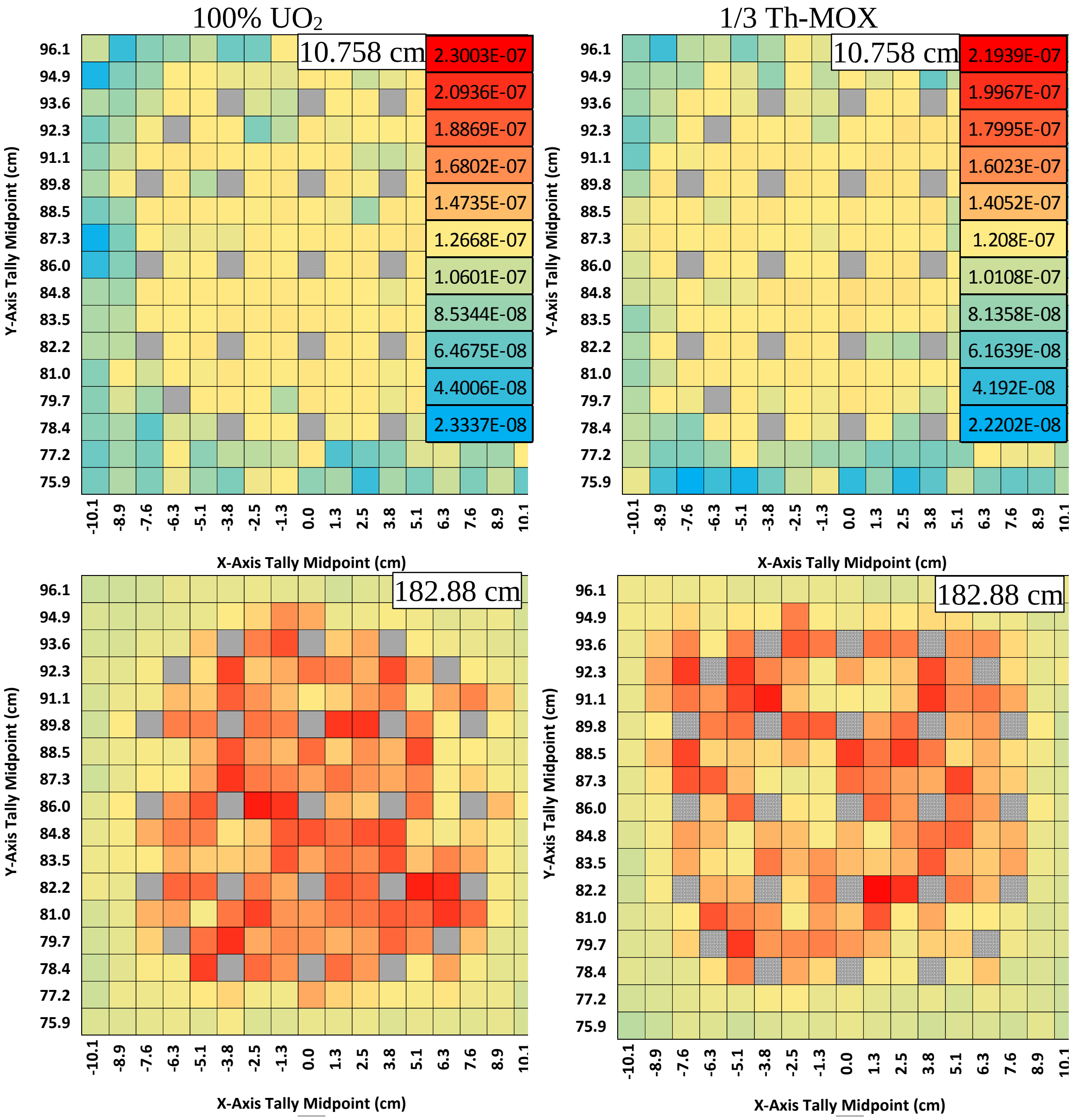

Fig. 11. Heat maps of the pin-by-pin thermal flux tally results for assembly H4 from each core from vertical sections 1 and 9. Results from the 100% UO_2 core are in the left column, and results from the 1/3 Th-MOX core are on the right. Water-filled channels are shown in gray.

5. Conclusions and Future Work

Based on the initial investigation presented here, it appears feasible to introduce Th-MOX fuel into the current fleet of PWRs. However, care is warranted in that many of the one-third Th-MOX configuration's safety parameters, while within the prescribed safety limits, are less favorable than those of the 100% UO_2 configuration.

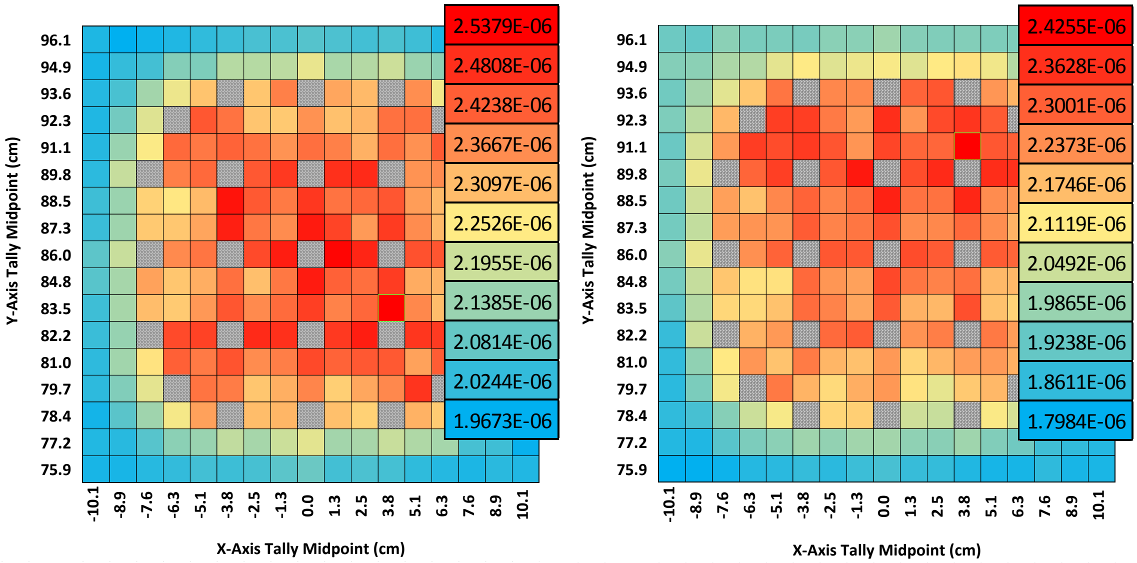

(a) (b)

Fig. 12. Heat maps of the total pin-by-pin thermal flux tally results summed over all 17 vertical sections in assembly H4 for each fuel configuration. Water-filled channels are gray. (a) 100% UO_2, peak assembly midpoint located at (x = 3.8 cm, y = 83.5 cm) (b) 1/3 Th-MOX, peak assembly midpoint located at (x = 3.8 cm, y = 91.1 cm)

Several configurations for replacing one-third of the UO_2 assemblies in a PWR with Th-MOX fuel were considered. It was found that replacing the blanket of higher enrichment (3.1%) UO_2 with Th-MOX had the smallest effect on excess reactivity and critical boron concentration, making this configuration most suitable for further study. Centerline axial and radial flux profiles were compared for several Th-MOX fuel compositions. A composition of 5.5 wt% PuO_2 in ThO_2 (94.5 wt%) resulted in the smallest flux difference relative to the 100% UO_2 configuration. Therefore, a blanket configuration of 5.5 wt% PuO_2 Th-MOX fuel was examined for all future safety analysis.

The delayed neutron fraction (β_{eff}) is a good indicator of a reactor's temporal response. For the 100% UO_2 configuration, β_{eff} was found to be 0.00716 ± 4.60E-07 compared to the 5.5 wt% PuO_2 Th-MOX blanket configuration's value of 0.00607 ± 4.30E-07. This 15% decrease in the delayed neutron fraction may not be significant enough to cause any safety related problems; however, the decrease in β_{eff} must be carefully examined for its impact on the reactor's safety.

Thermal reactivity feedback is another parameter of interest for operational safety. In this regard, the one-third Th-MOX configuration seemed to out-perform the 100% UO_2

configuration. The fuel temperature coefficient of reactivity for the one-third Th-MOX configuration was found to be -2.05 ± 0.02 pcm $^{o}F^{-1}$, which is lower than -1.42 ± 0.02 pcm $^{o}F^{-1}$, the value for the 100% UO_2 configuration. Likewise, the overall temperature coefficient of reactivity (moderator plus fuel) for the Th-MOX configuration was -1.89 ± 0.02 pcm $^{o}F^{-1}$, which was more favorable than the positive value of 0.84 ± 0.02 pcm $^{o}F^{-1}$ for the 100% UO_2 configuration. This favorable temperature feedback of reactivity may help compensate for reduced controllability via the lower β_{eff} of Th-MOX.

Shutdown margin (SDM) was the next safety parameter used to analyze the feasibility of the one-third Th-MOX configuration. To calculate shutdown margin, the rod worth of each control rod cluster in the northeast quadrant of the core was determined. It was found that the SDM for the 100% UO_2 configuration was 8804 ± 40 pcm, which was higher than the SDM of the Th-MOX configuration, 8134 ± 47 pcm. This aspect of the one-third Th-MOX configuration's behavior would require additional safety analysis before incorporating Th-MOX into the fuel cycle of a PWR could be recommended. While the estimated SDM was well within the NRC's prescribed limits, the reduction in SDM of the Th-MOX configuration could reduce its controllability. Increasing the boron-10 content of the control rods could ameliorate this issue. Nevertheless, this is an area of concern based on the present study.

Finally, nuclear hot channel factors were estimated to analyze any potential power peaking issues. The axial nuclear hot channel factor comparison showed no statistically significant difference between the 100% UO_2 configuration (1.47 ± 0.24) and the one-third Th-MOX configuration (1.49 ± 0.25). Though this result was promising, the results for the radial nuclear hot channel factor were less encouraging. The radial nuclear hot channel factor for the one-third Th-MOX configuration was found to be 1.67 ± 0.28 – 20% higher than the corresponding value of 1.39 ± 0.23 for the 100% UO_2 configuration. Therefore, additional studies are required.

It is important to reiterate that all analyses presented here were performed without any thermal fluid considerations. However, because of the identical core and assembly geometry, the assumption that the two cores will exhibit similar thermal fluid behavior during normal and off-normal operating conditions makes these comparisons relevant. Nevertheless, it would be beneficial to couple a detailed thermal analysis with this study to provide comprehensive answers to all safety concerns (i.e. hot channel factors, control rod worth and shutdown margin). Additionally, the analysis presented here was limited to the beginning-of-life condition. Burnup and fission product buildup were not included in the neutronic simulations. Burnup and buildup will be considered in a follow-up study.

References

[1] B.S. Van Gosen, V.S. Gillerman, T.J. Armbrustmacher. “Thorium Deposits of the United States—Energy Resources for the Future?” U.S. Geological Survey Circular 1336. 2009.

[2] E.M. Baum, H.D. Knox, T.R. Miller. “Nuclides and Isotopes: Chart of Nuclides, 16th Ed.” Lockheed Martin Distribution Services. 2002.

[3] F. Sokolov, K. Fukuda, H.P. Nawada. “Thorium Fuel Cycle – Potential Benefits and Challenges” IAEA-TECDOC-1450. IAEA. Vienna, 2005.

[4] “Role of Thorium to Supplement Fuel Cycles of Future Nuclear Energy Systems” IAEA Nuclear Energy Series No. NF-T-2.4. IAEA. Vienna, 2012.

[5] S. Peggs, W. Horak, T. Roser, et al. “Thorium Energy Futures” Proceedings of IPAC2012. New Orleans, 2012.

[6] J.A. Lane “Fluid Fuel Reactors” Addison-Wesley Pub. Co. 1958.

[7] P.N. Haubenreich, J.R. Engel. “Experience with the Molten-Salt Reactor Experiment” Nuclear Applications and Technology. 1970.

[8] D.E. Holcomb, G.F. Flanagan, B.W. Patton, J.C. Gehin, R.L. Howard, T.J. Harrison, “Fast Spectrum Molten Salt Reactor Options” ORNL Report ORNL/TM-2011/105. 2011.

[9] Zuoyi Zhang, Zongxin Wu, Dazhong Wang, Yuanhui Xu, Yuliang Sun, Fu Li, Yujie Dong. “Current Status and Technical Description of Chinese 2 x 250 MW_{th} HTR-PM Demonstration Plant” Nuclear Engineering and Design, 239, 1212-1219. July 2009.

[10] S. Banerjee. “Towards a Sustainable Nuclear Energy Future” 35th World Nuclear Association Symposium. London, 2010.

[11] P. Bromley, et al. “LWR-Based Transmutation of Nuclear Waste An Evaluation of Feasibility of Light Water Reactor (LWR) Based Actinide Transmutation Concepts-Thorium-Based Fuel Cycle Options” BNL-AAA-2002-001. 2002.

[12] K.D. Weaver, J.S. Herring. “Performance of Thorium-Based Mixed Oxide Fuels for the Consumption of Plutonium in Current and Advanced Reactors” Nucl. Tech., 143, 22-36. 2002.

[13] M. Todosow, G. Raitses. “Thorium Based Fuel Cycle Options for PWRs” Proceedings of ICAPP ’10, 1891-1900. June 13-17, 2010.

[14] K.I. Bjork. “A BWR Fuel Assembly Design for Efficient Use of Plutonium in Thorium-Plutonium Fuel” Progress in Nuclear Energy, 65, 56-63. 2013.

[15] K.I. Bjork, V. Fhager, C. Demaziere. “Comparison of Thorium-Based Fuels with Different Fissile Components in Existing Boiling Water Reactors” Progress in Nuclear Energy, 53, 618-625. 2011.

[16] Yunlin Xu, T.J. Downar, H. Takahashi, U.S. Rohatgi. “Neutronics Design and Fuel Cycle Analysis of a High Conversion BWR with Pu-Th Fuel” ICAPP. Florida, 2002.

[17] P. Mac Donald, M.S. Kazimi. “Advanced Proliferation Resistant, Lower Cost, Uranium-Thorium Dioxide Fuels for Light Water Reactors” NERI Annual Report, INEEL/EXT-2000-01217. 2000.

[18] J.L. Francois, A. Nuñez-Carrera, G. Espinosa-Paredes, C. Martin-del-Campo. “Design of a Boiling Water Reactor Equilibrium Core Using Thorium-Uranium Fuel” Americas Nuclear Energy Sumposium 2004. Miami Beach, FL, 2004.

[19] E. Shwageraus, P. Hejzlar, M.S. Kazimi. “Use of Thorium for Transmutation of Plutonium and Minor Actinides in PWRs” Nucl. Tech., 147, 53-68. 2004.

[20] E. Shwageraus, P. Hejzlar, M.J. Driscoll, M.S. Kazimi. “Optimization of Micro-Heterogeneous Uranium-Thorium Dioxide PWR Fuels for Economics and Enhanced Proliferation Resistance”, MIT-NFC-TR-046, MIT, Nucl. Eng. Dep, 2002.

[21] K.I. Bjork, C.W. Lau, H. Nylen, U. Sandberg. “Study of Thorium-Plutonium Fuel for Possible Operating Cycle Extension in PWRs” Science and Technology of Nuclear Installations. 2013.

[22] H.R. Trellue, C.G. Bathke, P. Sadasivan. “Neutronics and Material Attractiveness for PWR Thorium Systems Using Monte Carlo Techniques” Progress in Nuclear Energy, 53, 698-707. 2011.

[23] H. Tsige-Tamirat. “Neutronics Assessment of the Use of Thorium Fuels in Current Pressurized Water Reactors” Progress in Nuclear Energy, 53, 717-721. 2011.

[24] E. Fridman, S. Kliem. “Pu Recycling in a full Th-MOX PWR Core. Part I: Steady State Analysis” Nucl. Eng. and Design, 241, 193-202. 2011.

[25] P.G. Boczar, G.R. Dyck, P.S.W. Chan, D.B. Buss. “Recent Advances in Thorium Fuel Cycles for CANDU Reactors” Thorium Fuel Utilization: Options and Trends, IAEA-TECDOC-1319, 104-122. IAEA, Vienna, 2002.

[26] R.K. Sinha, A. Kakodar. “Design and Development of the AHWR – the Indain Thorium Fuelled Innovative Nuclear Reactor” Nucl. Eng. and Design, 236, 683-700. 2006.

[27] S. Michalek, J. Hascik, G. Farkas. “MCNP5 Delayed Neutron Fraction (β_{eff}) Calculation in Training Reactor VR-1” Jour. of Elec. Eng., 59, 221-224, 2008.

[28] J.R. Lamarsh. “Introduction to Nuclear Reactor Theory” American Nuclear Society, Inc. LaGrange Park, Ill. 2002.

[29] “Callaway cycle 15 core operating limits report (Revision 1)” ULNRC-05335. U.S. Nuclear Regulatory Commission. 28 September 2006.

[30] “Inspection Procedure 61708: Isothermal and moderator temperature coefficient determinations” NRC Inspection Manual. 11 October 1985.

[31] J. Weisman. *Elements of Nuclear Reactor Design*. 2nd Ed. Robert E. Kriegler Publishing Company. Malabar, Florida. 1983.

[32] K. Hesketh, A. Worrall. “The Thorium Fuel Cycle: An independent assessment by the UK National Nuclear Laboratory” National Nuclear Laboratory Position Paper. 2010.

IV. THORIUM-BASED MIXED OXIDE FUEL IN A PRESSURIZED WATER REACTOR: A BURNUP ANALYSIS WITH MCNP

Lucas P. Tucker and Shoaib Usman[3]

Abstract

A three-dimensional MCNP model of a Westinghouse-type 17x17 PWR was used to assess the feasibility of enhancing the current fuel supply with a thorium-plutonium mixed oxide fuel (ThMOX). A conventional UO_2-fueled configuration was compared to a configuration which incorporated ThMOX fuel. The safety of the ThMOX configuration was compared to that of the UO_2 configuration at several time steps of interest within all three cycles (beginning of cycle, peak excess reactivity of cycle, and end of cycle) using the following metrics: axial and radial nuclear hot channel factors (F_Z^N and F_R^N), moderator and fuel temperature coefficients (MTC and FTC), delayed neutron fraction (β_{eff}), and shutdown margin (SDM). Additionally, the performance of the ThMOX configuration was assessed by tracking cycle lengths, the amount of plutonium destroyed, and fission product poison concentration.

The ThMOX configuration's F_Z^N (1.839 ± 0.951) was less favorable than that of the UO_2 configuration (1.515 ± 0.246), as was its F_R^N (3.820 ± 0.232 compared to 3.430 ± 0.066 for UO_2). The delayed neutron fraction was another problem area for the ThMOX configuration. It was lower than that of the UO_2 configuration, but the lowest β_{eff} occurred at the beginning of Cycle 3 (3.324E-03 ± 8.919E-07). The β_{eff} of the UO_2 configuration was 46% higher (6.177E-03 ± 1.510E-06) at this time step. Similarly, the ThMOX configuration's SDMs were less favorable than those of the UO_2 configuration, though even the lowest (3971 ± 43 pcm) remained well within the NRC prescribed limit of 1300 pcm. However, the MTC of the ThMOX configuration was more favorable for all time steps except the beginning of Cycle 3, and even then it was negative as required by the NRC (-2.325 ± 0.00098 pcm/^oF). The FTC results were also more favorable for the

---

[3] Correspondence to usmans@mst.edu, 225 Fulton Hall, 301 W. 14th Street Rolla, MO 65409.

ThMOX configuration. Its highest FTC value (-6.132 ± 0.00186 pcm/^{o}F at the peak of Cycle 1) was more negative than the lowest FTC of the UO_2 configuration (-4.391 ± 0.00156 pcm/^{o}F at the beginning of Cycle 2).

Overall, incorporating ThMOX fuel into the fuel supply for a conventional PWR seems feasible from a neutronics standpoint. However, a full thermal hydraulic analysis is required. Also, this analysis would benefit from a more detailed burnup simulation and optimization of the ThMOX fuel composition.

1. Introduction

Thorium represents a vast, largely untapped source of nuclear energy. Its abundance in the earth's crust is roughly three times greater than uranium [1]. Though ^{232}Th – the only naturally occurring isotope of thorium – is not fissile, it is fertile. After absorbing a neutron to become ^{233}Th and decaying to ^{233}Pa, it ultimately decays to ^{233}U [2]. Thorium-based fuels offer several potential advantages over uranium fuels: higher fissile conversion rate, higher thermal fission factor (η), lower capture-to-fission ratio, low actinide production, plutonium reduction, and chemical stability [3, 4, 5, 6].

Perhaps the most expedient scheme for exploiting the world's thorium resources is by incorporating it into the current light water reactor (LWR) fuel supply. As the reactor type with the greatest install base, the pressurized water reactor (PWR) warrants the greatest attention. Since it is fertile, a fissile isotope must be included with thorium if it is to be used in a conventional reactor. In this way, a thorium-plutonium mixed oxide (ThMOX) fuel can be used for the disposition of plutonium.

The concept of destroying plutonium in current-gen LWRs with ThMOX fuel has been researched by many – mostly with computer simulations. Throughout the literature studies can be found with a variety of fuel compositions, core configurations, burnup histories, design objectives, and modeling methodologies. Sometimes the focus is on safety characteristics: Mittag et al. focused on changes in coefficients of reactivity when one-third of the core was replaced with ThMOX [19], while Bjork et al. considered a wider variety of parameters, including control rod worths and decay heat for several fuel compositions [20]. Other times the focus is on performance: Trellue et al. analyzed the improvement in plutonium destruction ThMOX fuel provides over conventional MOX fuel for a one-third MOX core [21], Fridman and Kliem also looked at the plutonium destruction capability of ThMOX [22] and Bjork et al. and Weaver et al. considered improvements in cycle length [23, 24]. More exotic applications are receiving attention as well. Baldova et al. have considered ThMOX fuel for breeding ^{233}U [25]. Todosow et al. considered the impact ThMOX would have at the fuel cycle level rather than at the level of an individual reactor [26]. It is also worth noting that the analysis of ThMOX fuel has moved out of the realm of simulations and into experimentation [27]. However, none of these studies focus on the transition from a UO_2 fueled core to a one-third ThMOX core to a full ThMOX core.

The feasibility of the use of ThMOX fuel in a PWR was examined by Tucker, Alajo, and Usman for beginning of life (BOL) conditions [7]. A three-dimensional MCNP model of a Westinghouse-type 17x17 PWR was used to examine various possibilities for replacing one-third of the UO_2 assemblies with ThMOX assemblies. The excess reactivity, critical boron concentration, and centerline axial and radial flux profiles for several configurations and compositions of a one-third ThMOX core were compared to a 100% UO_2 core. A blanket-type arrangement of 5.5% PuO_2 by weight was determined to be the best candidate for further analysis. Therefore, this configuration was compared to a 100% UO_2 core using the following parameters: delayed neutron fraction (β_{eff}), temperature coefficient, shutdown margin (SDM), and axial and radial nuclear hot channel factors (F_Z^N and F_R^N). The one-third ThMOX core compared favorably, and a burnup analysis was recommended.

This work is a continuation of Tucker et al.'s BOL feasibility analysis [7]. Starting with the configuration that was identified as most favorable in the earlier study (one-third 5.5% PuO_2 in the blanket configuration), a three cycle burnup analysis was performed using MCNP [8]. After the end of the first and second cycles, the discarded UO_2 fuel was replaced with fresh ThMOX fuel. The third cycle was fueled entirely with ThMOX. The results of the ThMOX burnup analysis were compared to a similar analysis of an unmodified 100% UO_2 fueled core. Several characteristics of each configuration were monitored throughout the burnup analysis: excess reactivity (ρ_{ex}), critical boron concentration (CBC), cycle length, plutonium destruction, and fission product poison concentration. Additionally, the performance of the ThMOX configuration was evaluated against that of the UO_2 configuration by comparing delayed neutron fraction (β_{eff}), overall temperature coefficient, fuel temperature coefficient, shutdown margin, axial and radial nuclear hot channel factors. All of these characteristics and criteria were evaluated at the beginning and end of each cycle unless unnecessary (e.g. excess reactivity at end of cycle).

2. Description of Reactor Configurations

The beginning of cycle (BOC) 1 core configurations are based on the work performed for the BOL feasibility analysis. As seen in Figure 1a the 100% UO_2 core is composed of assemblies of three different fuel enrichments: 3.1% (Group 1), 2.6% (Group 2), and 2.1% (Group 3). For the ThMOX core, the 3.1% enriched fuel in Group 1 was replaced with 5.5% PuO_2 ThMOX as seen in Figure 1b. Replacing the 3.1% enriched UO_2 assemblies with ThMOX assemblies is consistent with the goal of destroying the maximum amount of plutonium. The BOL composition of the plutonium in the ThMOX fuel can be seen in Table 1.

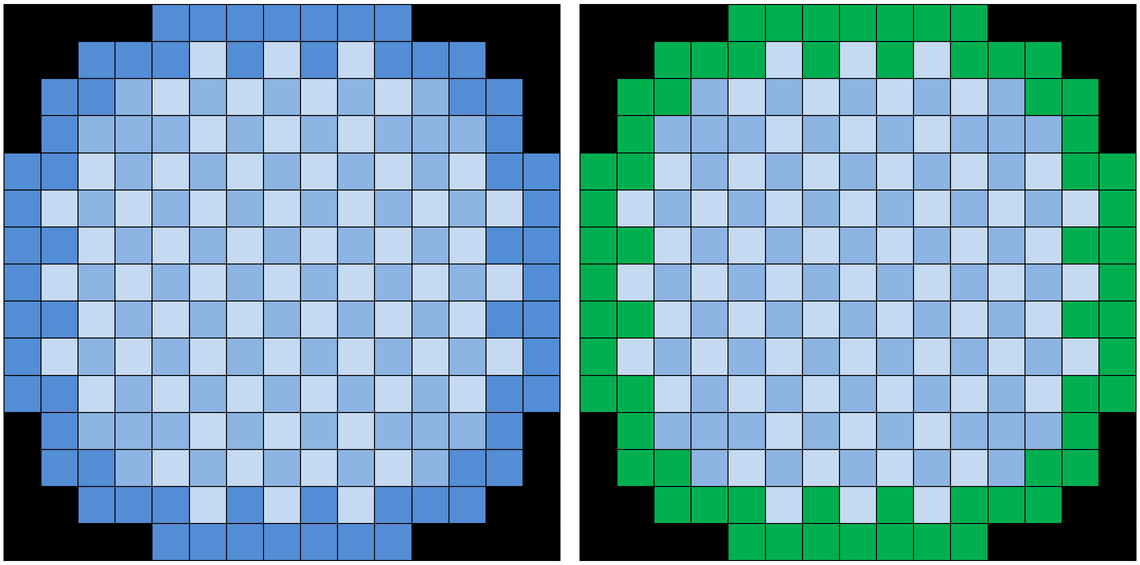

(a) (b)

Fig. 1. Beginning of Cycle 1 fuel configurations. (a) UO_2. (b) ThMOX. 3.1% enriched UO_2 in dark blue, 2.6% enriched UO_2, in medium blue, 2.1% enriched UO_2 in light blue, Th-MOX in green.

Table 1. Isotopic composition of plutonium used for ThMOX. Adapted from Shwageraus, Hejzlar, and Kazimi [9].

Isotope	Weight Percent
^{238}Pu	3.18
^{239}Pu	56.35
^{240}Pu	26.62
^{241}Pu	8.02
^{242}Pu	5.83

For Cycle 1, which is the BOL cycle, both cores were loaded with borosilicate glass tube burnable absorbers to compensate for the lack of fission product poisons. Burnable absorbers are located within fuel assembly guide tubes. The arrangement that was used for both cores can be seen in Figure 2. Burnable absorbers were not used for Cycles 2 or 3.

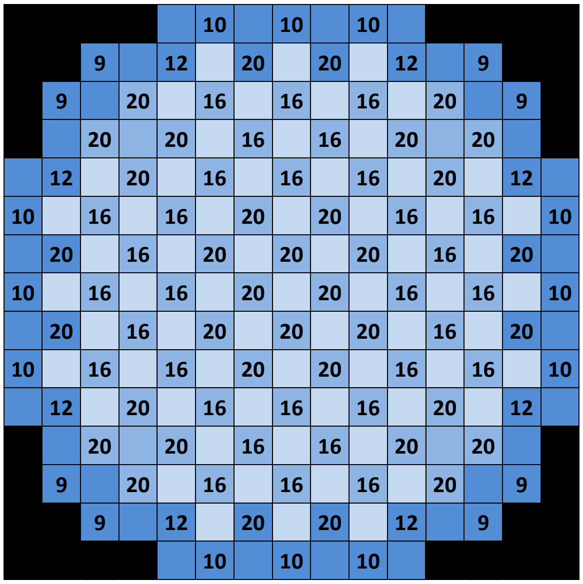

					10		10		10					
		9		12		20		20		12		9		
	9		20		16		16		16		20		9	
		20		20		16		16		20		20		
	12		20		16		16		16		20		12	
10		16		16		20		20		16		16		10
	20		16		20		20		20		16		20	
10		16		16		20		20		16		16		10
	20		16		20		20		20		16		20	
10		16		16		20		20		16		16		10
	12		20		16		16		16		20		12	
		20		20		16		16		20		20		
	9		20		16		16		16		20		9	
		9		12		20		20		12		9		
					10		10		10					

Fig. 2. Cycle 1 burnable absorber arrangement for both the UO_2 and the ThMOX cores. Assemblies with burnable absorber rods are indicated by the number of rods in the assembly.

Nearly all simulations were run with all control rods fully withdrawn. The exceptions were those simulations performed to calculate shutdown margin. Two types of control rods were used: full-length and part-length. Dimensions and composition of each control rod type can be found in Table 2, and the distribution of control assemblies can be seen in Figure 3.

Table 2. Attributes of full-length and part-length control assemblies in a PWR.

	Full-Length Control Assembly	Part-Length Control Assembly
Active length	360.68 cm	91.44 cm
Composition	80% Silver	80% Silver
	15% Indium	15% Indium
	5% Cadmium	5% Cadmium
Number in Core	53	8

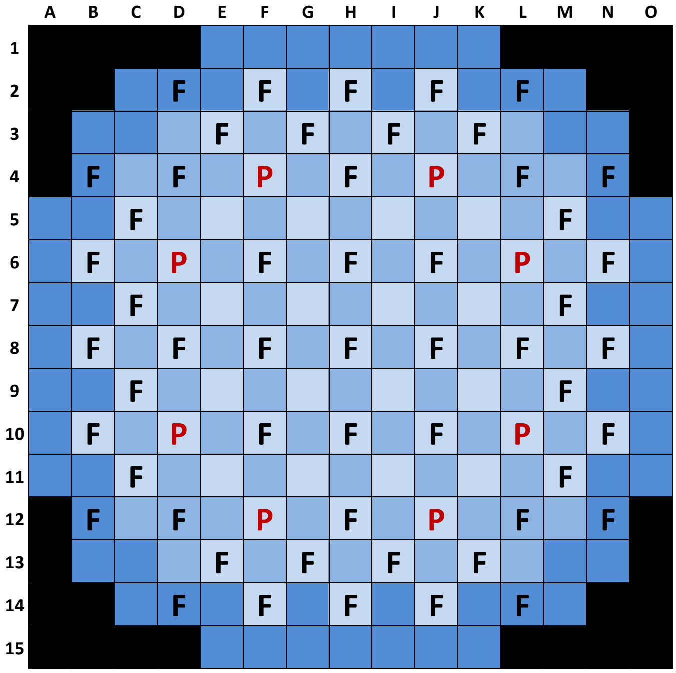

	A	B	C	D	E	F	G	H	I	J	K	L	M	N	O
1															
2				F		F		F		F		F			
3					F		F		F		F				
4		F		F		P		F		P		F		F	
5			F										F		
6		F		P		F		F		F		P		F	
7			F										F		
8		F		F		F		F		F		F		F	
9			F										F		
10		F		P		F		F		F		P		F	
11			F										F		
12		F		F		P		F		P		F		F	
13					F		F		F		F				
14				F		F		F		F		F			
15															

Fig. 3. PWR control assembly layout. Full-length control assemblies are marked with an "F". Part-length control assemblies are marked with a "P".

There are many possible configurations for PWRs – various enrichments, fuel assembly arrangements, burnable absorber and control assembly compositions and distributions, etc. The configuration selected for this work was chosen based on the information available to the authors regarding fuel assembly dimensions, material compositions, etc. The purpose of this work is to assess the feasibility of incorporating ThMOX fuel into the PWR fuel supply. While this work does suggest the feasibility of incorporating ThMOX fuel into the PWR fuel supply, further analysis and optimization as well as experimental validation would have to be performed before implementation of such a drastic change in the fuel cycle.

3. Burnup Procedure

The burnup analysis presented here was completed using MCNP6. The MCNP6 burnup capability is based on the utility developed for MCNPX [8]. First, a steady-state neutron transport calculation is performed to determine k_{eff}, the energy-dependent flux distribution and reaction rates, fission multiplicity (ν), and the recoverable energy per fission [10]. This information is passed to CINDER90 to perform depletion calculations and generate new number densities which correspond to the end of a prescribed time step [10]. The new number densities are passed back to MCNP for the next neutron transport calculation. This process is repeated for as many time steps as are requested by the user. It is important to take time steps small enough to ensure minimal change in flux shape, as large flux shape changes between time steps will produce unreliable results.

When setting up the BURN card, the user must specify which fission products MCNP should track. There are three tiers of fission products that can be tracked. There are twelve isotopes in Tier 1 [10]. Tier 2 asks MCNP to track all fission products for which there are neutron cross sections in the cross section directory [10]. Tier 3 contains all fission products for which CINDER90 has fission yield data [10]. For this work the Tier 2 fission products were used.

It is possible for CINDER90 to generate fission product isotopes for which cross section data does not exist in MCNP. Therefore, MCNP’s BURN card allows the user to provide a list of isotopes to be omitted from neutron transport calculations and from the output file [10]. Ultimately, 177 isotopes had to be omitted from this work. The inclusion of these isotopes could affect both the neutron transport characteristics of either reactor and the discharge activity of each material. However, the isotopes omitted had very low concentrations (on the order of 10^{-10} atom percent) with either short half-lives and/or small neutron cross sections.

A burnup run outputs an abundance of data. At the system level, MCNP reports the multiplication factor, the total flux, the average ν, the average Q, the total burnup, and the source strength. For each material tracked by the burnup calculation, values are returned for the fraction of the power produced and burnup in GWd/MTHM for each time step. It is also returns the mass and activity of each materials’ isotopes at each time step.

In this analysis, burnup calculations were performed for 31 materials, each of which corresponded to a fuel assembly location as seen in Figure 4. Using 31 materials made it possible to take advantage of a PWR’s one-eighth symmetry while accounting for differences in flux at each location. However, this forced burnup to be uniform across each assembly both axially and radially. Additionally, all burnup calculations were performed without boric acid in the coolant. This simplified the calculations and reduced run time, but it likely also reduced cycle length.

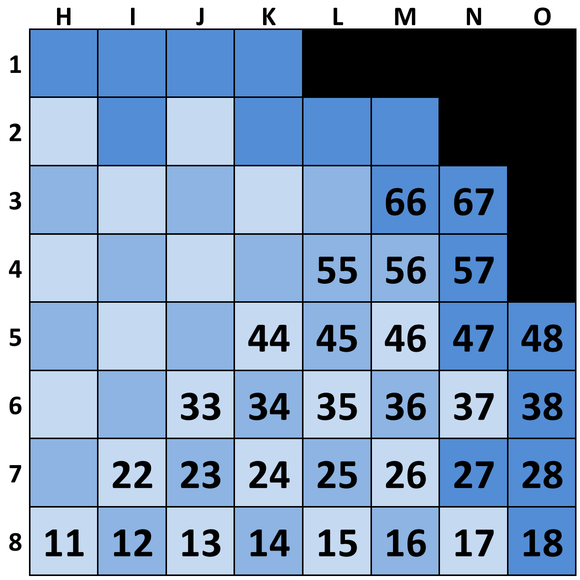

	H	I	J	K	L	M	N	O
1								
2								
3						66	67	
4					55	56	57	
5				44	45	46	47	48
6			33	34	35	36	37	38
7		22	23	24	25	26	27	28
8	11	12	13	14	15	16	17	18

Fig. 4. Map of materials used for burnup analysis

All simulations were performed with MNCP6 Version 1.0. The ENDF-VII cross section libraries were used (unless unavailable for a particular isotope). For most problems, ten million histories (500 active KCODE cycles of 20,000 histories) were sufficient to obtain a relative error of less than 10%. All burnup simulations were performed on a machine with an Intel Core i7 CPU and 32 GB of RAM.

4. Cycle Lengths

This analysis was run for three cycles. The goal for the ThMOX configuration was to destroy plutonium and match the performance of the UO_2 configuration – in that order. Shorter burnup steps were used at the beginning of each cycle as fission product poison equilibrium values are reached and, in the case of Cycle 1, as burnable absorber rods are consumed. Longer burnup steps (100 days each) were used once roughly linear burnup began. Shorter burnup steps (20 to 50 days) were used towards the end of each cycle in an attempt to capture the day k_{eff} reached unity within 100 pcm. After the end of Cycles 1 and 2 a thirty-day decay was performed to approximate a refueling shutdown. Following the decay step, Group 3 fuel assemblies were removed and replaced with Group 2 assemblies; Group 2 fuel assemblies were replaced with Group 1 fuel assemblies; and Group 1 assemblies were replaced with fresh fuel assemblies.

As can be seen in Figure 4, some assemblies have one-eighth symmetry (they are one of eight assemblies with identical neutronic and material characteristics, such as Assembly 67), while others (such as Assembly 18) have one-fourth symmetry, and Assembly 11 has no symmetry. Assembly 11 was not shuffled between cycles, but was instead replaced with fresh 2.1% enriched fuel at the beginning of each cycle. For all other assemblies, the following fuel shuffling procedure was used for both configurations before Cycles 2 and 3. First, the assemblies from each group were sorted by burnup in descending order. The one-eighth symmetry assembly with the lowest burnup in Group 2 was used to fill the two one-fourth symmetry assembly locations with the highest burnup in Group 3. The one-fourth symmetry assembly with the lowest burnup in Group 2 was used to fill the third lowest one-fourth symmetry assembly location in Group 3, and so on and so forth for the rest of the one-fourth symmetry assemblies from Group 2. The one-eighth symmetry assembly from Group 2 with the second lowest burnup was then used to fill the one-eighth symmetry assembly location with the highest burnup in Group 3. The one-eighth symmetry assembly from Group 2 with the third lowest burnup was then used to fill the one-eighth symmetry assembly location with the second highest burnup in Group 3, and so on and so forth for the remaining one-eighth symmetry assemblies in Group 2. The same procedure was used to shuffle assemblies from Group 1 to Group 2. A visualization of this procedure can be seen in Figure 5.

For Cycles 2 and 3 the plutonium content of the fresh ThMOX fuel was increased to match the BOC excess reactivity of the UO_2 configuration. The BOC critical boron concentration (CBC) was also determined. See Table 3 for each cycle's excess reactivity and CBC. A more detailed discussion of each cycle is found in Sections 4.1, 4.2, and 4.3.

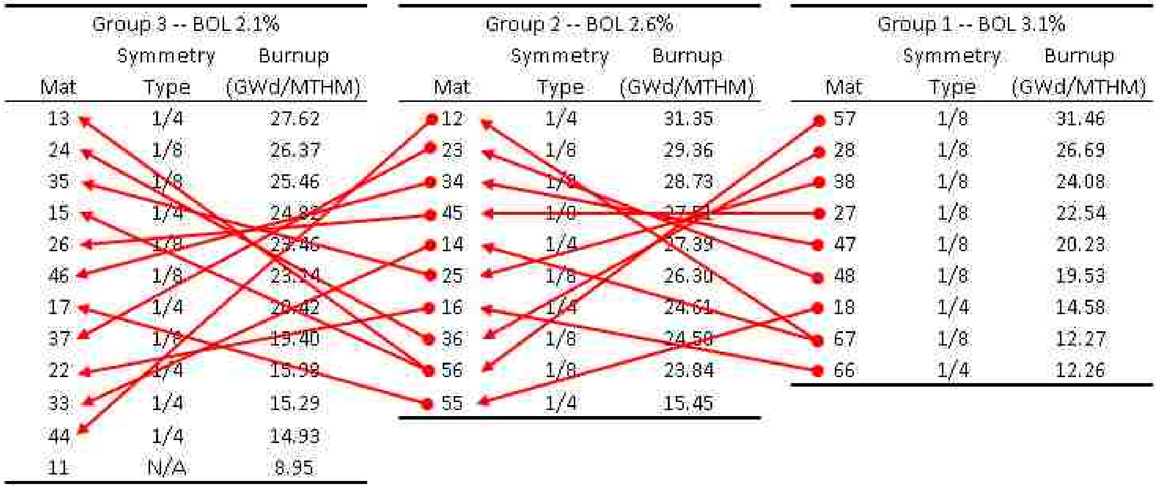

Fig. 5. Visualization of fuel shuffling procedure for the 100% UO_2 configuration from Cycle 1 to Cycle 2.

Table 3. Excess reactivity and critical boron concentration.

	UO_2		ThMOX	
	ρ_{ex} (% Δk/k)	CBC (ppm B)	ρ_{ex} (% Δk/k)	CBC (ppm B)
BOC 1	14.793 ± 0.019	1290 ± 7	14.183 ± 0.020	1322 ± 19
POC 1	19.109 ± 0.019	1690 ± 6	17.866 ± 0.020	1678 ± 18
BOC 2	12.507 ± 0.005	1156 ± 10	12.541 ± 0.022	3997 ± 14
BOC 3	16.069 ± 0.020	1540 ± 11	16.086 ± 0.023	8504 ± 21

4.1. Cycle 1

Both the 100% UO_2 and the ThMOX configurations began Cycle 1 composed entirely of fresh fuel (Figure 1) and with burnable absorbers (Figure 2). In Figure 6 each configuration's multiplication factor is plotted against cycle time. There is an initial drop in k_{eff} during the first ten days as fission product poisons (FPP) reach equilibrium followed by an upswing as the burnable absorbers are consumed until each configuration reaches its peak multiplication factor after forty days. This time step (40 days after the beginning of Cycle 1) will be referred to as peak of cycle (POC). The ThMOX curve closely follows the UO_2 curve, but with slightly less excess reactivity at BOC its cycle length is shorter. This is understandable as the fissile content of the ThMOX fuel is less than that of the UO_2 fuel it replaced.

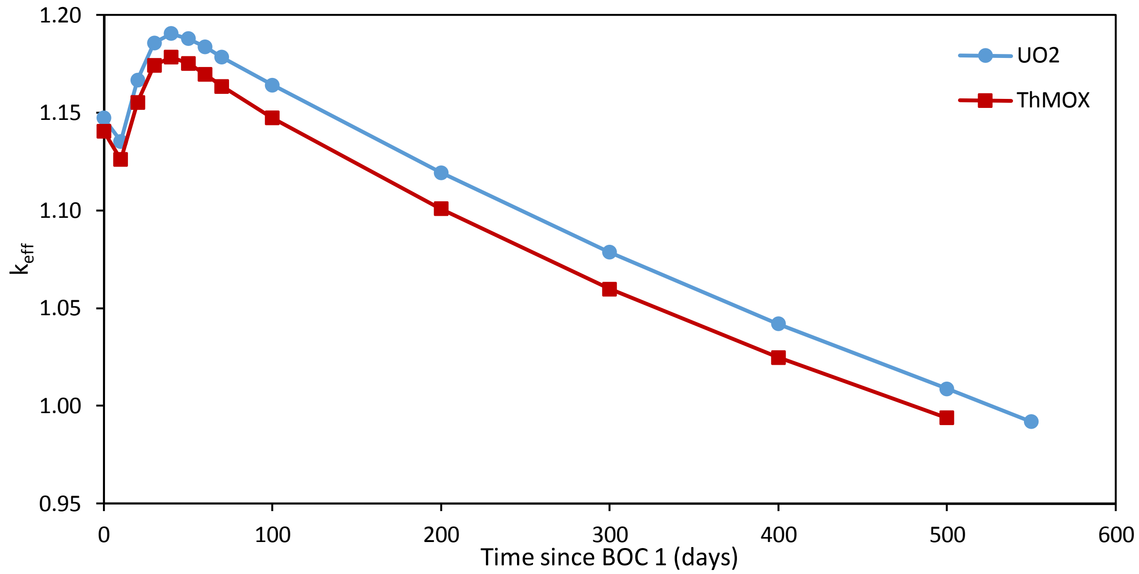

Fig. 6. Multiplication factor plotted against time for both core configurations for Cycle 1.

4.2. Cycle 2

The 100% UO_2 configuration began Cycle 2 with 64 fresh 3.1% enriched UO_2 assemblies (Group 1), 64 once-burned, 3.1% enriched UO_2 assemblies (Group 2); 64 once-burned, 2.6% enriched UO_2 assemblies (Group 3); and one fresh, 2.1% enriched UO_2 assembly at the center of the reactor (position H8). No burnable absorbers were used. The multiplication factor for the UO_2 configuration reached unity after two hundred days. The multiplication factor trend for both configurations are plotted in Figure 7.

At the beginning of Cycle 2 the plutonium content of the Group 1 fuel assemblies in the ThMOX configuration was increased from 5.5% PuO_2 to 15.8% PuO_2. This higher plutonium concentration was used to maximize plutonium destruction without exceeding the BOC excess reactivity of the UO_2 configuration. Group 2 assemblies contained once-burned, 5.5% ThMOX; Group 3 assemblies contained once-burned, 2.6% UO_2; and the center-most assembly (position H8) contained fresh, 2.1% UO_2. No burnable absorbers were used. The increase in plutonium concentration of the Group 1 fuel resulted in a 470 day cycle – 270 days longer than Cycle 2 for the UO2 configuration and only 30 days shorter than Cycle 1 for the ThMOX configuration. However, as seen in Table 3, the higher fissile content increases the BOC CBC substantially when compared to ThMOX Cycle 1,

UO_2 Cycle 1 or UO_2 Cycle 2. The increase in CBC made temperature coefficient and shutdown margin calculations vital. See Section 9 and Section 10 for those results.

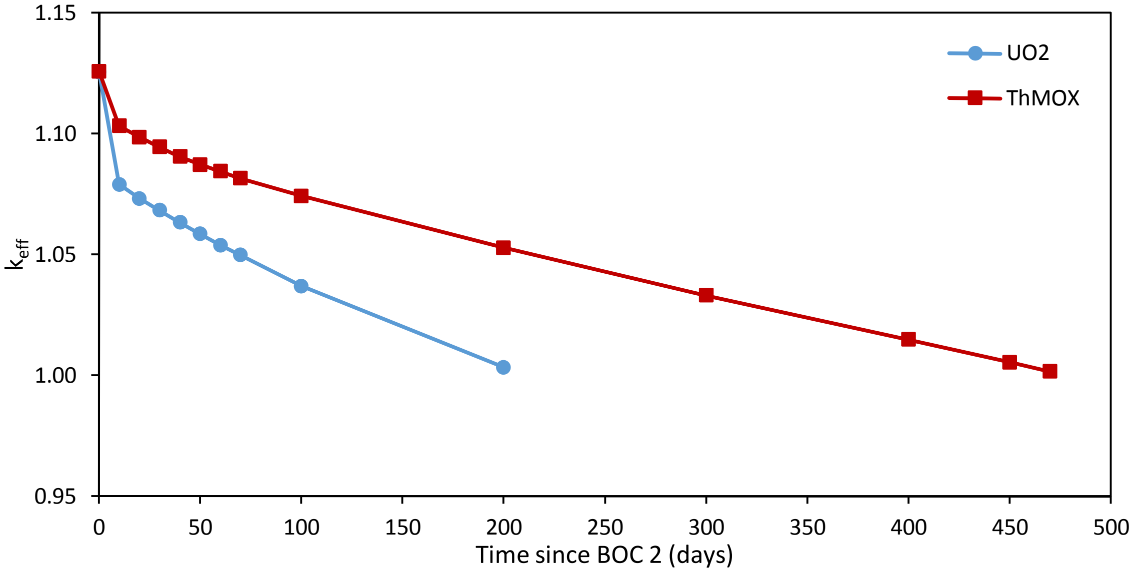

Fig. 7. Multiplication factor plotted against time for both core configurations for Cycle 2.

4.3. Cycle 3

The 100% UO_2 configuration began Cycle 3 with 64 fresh 3.1% enriched UO_2 assemblies (Group 1), 64 once-burned, 3.1% enriched UO_2 assemblies (Group 2); 64 twice-burned, 3.1% enriched UO_2 assemblies (Group 3); and one fresh, 2.1% enriched UO_2 assembly at the center of the reactor (position H8). No burnable absorbers were used. The cycle lasted 320 days. The multiplication factor trend for both configurations are plotted in Figure 8.

At the beginning of Cycle 3 the plutonium content of the Group 1 fuel assemblies in the ThMOX configuration was increased from 15.8% PuO_2 to 19.2% PuO_2. This was done to maximize plutonium destruction without exceeding the BOC excess reactivity of the UO_2 configuration. Group 2 assemblies contained once-burned, 15.8% ThMOX; Group 3 assemblies contained twice-burned, 5.5% PuO_2 ThMOX; and the center-most assembly (position H8) contained fresh, 2.1% UO_2. No burnable absorbers were used. The increase in plutonium concentration of the Group 1 fuel combined with the increase that had been made for Cycle 2 resulted in a 975 day cycle. It is unlikely that a commercial power reactor would run for 975 days given the host of non-neutronic problems such a long cycle would likely cause. However, such a run would destroy (or make unavailable) a substantial quantity of plutonium. See Section 5 for discussion of the changes in plutonium concentration for each cycle and fuel configuration. Additionally, as for the ThMOX Cycle 2 configuration, the higher fissile content increases the BOC CBC substantially. See Section 9 and Section 10 for a discussion of the impact on temperature coefficient and shutdown margin.

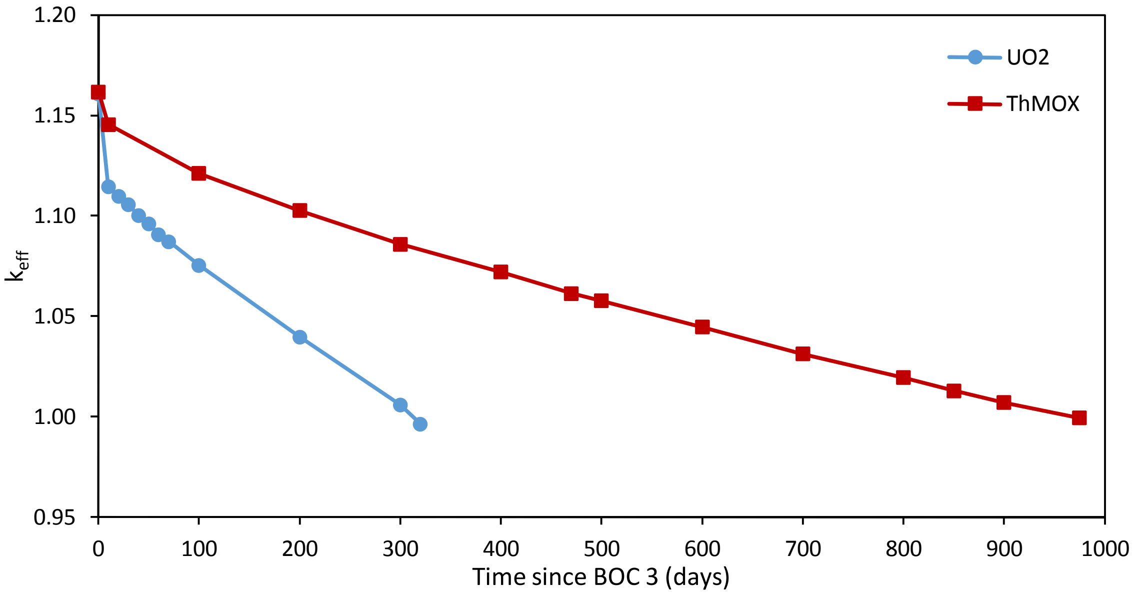

Fig. 8. Multiplication factor plotted against time for both core configurations for Cycle 3.

5. Plutonium Destruction

The purpose of this work was to assess the feasibility of using a ThMOX fuel in a conventional PWR for plutonium destruction. Therefore, it was vital to examine the amount of plutonium destroyed by the ThMOX fuel cycle. Table 4 provides the mass in kilograms of plutonium in the whole core at the beginning of each cycle for each configuration, while Table 5 provides the net change in plutonium mass. The change in plutonium mass during Cycles 1, 2, and 3 are plotted in Figures 9, 10, and 11, respectively.

Table 4. Total core plutonium mass in kilograms at the beginning of each cycle for both configurations.

	UO$_2$			ThMOX		
	^{239}Pu	^{240}Pu	^{241}Pu	^{239}Pu	^{240}Pu	^{241}Pu
Cycle 1	0	0	0	727	282	204
Cycle 2	279	105	52	3192	1394	976
Cycle 3	248	78	38	5083	2501	1717

Table 5. Net change in core plutonium mass (kg) for each configuration at the end of each cycle and totaled across all three cycles.

	UO$_2$			ThMOX		
	^{239}Pu	^{240}Pu	^{241}Pu	^{239}Pu	^{240}Pu	^{241}Pu
Cycle 1	397	146	70	-17	111	37
Cycle 2	102	42	22	-1094	-42	-99
Cycle 3	150	72	39	-2430	-307	-366
Total	649	260	131	-3541	-238	-427

During Cycle 1, the net loss of ^{239}Pu for the ThMOX configuration was only 17 kg (2.4% of BOC mass). Cycle 1 illustrates why increasing the concentration of plutonium in the fuel and the number of ThMOX assemblies in the core is necessary for efficient plutonium destruction. Two-thirds of the fuel assemblies in the ThMOX configuration were conventional UO$_2$ assemblies comprised mostly of ^{238}U. As the cycle progressed these assemblies produced almost enough plutonium to completely negate the loss of plutonium in the ThMOX assemblies, which comprised one-third of the core. To maximize plutonium destruction during Cycle 2 without exceeding the BOC excess reactivity of the UO$_2$ configuration, an additional one-third of the UO$_2$ assemblies were replaced with ThMOX assemblies and the amount of PuO$_2$ was increased from 5.5% to 15.8% as described in Section 4.2.

During Cycle 1, the net loss of ^{239}Pu for the ThMOX configuration was only 17 kg (2.4% of BOC mass). Cycle 1 illustrates why increasing the concentration of plutonium in the fuel and the number of ThMOX assemblies in the core is necessary for efficient plutonium destruction. Two-thirds of the fuel assemblies in the ThMOX configuration were conventional UO$_2$ assemblies comprised mostly of ^{238}U. As the cycle progressed these

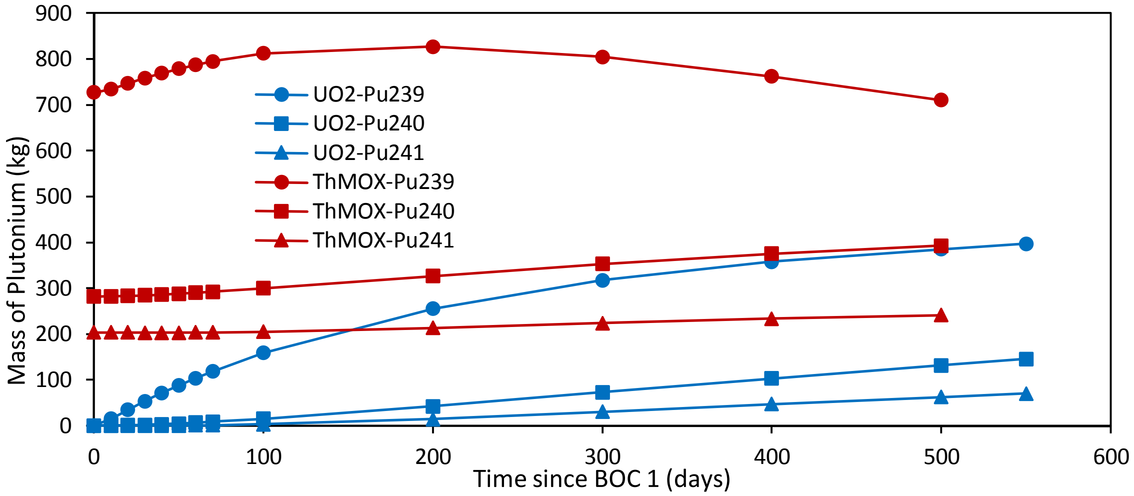

Fig. 9. Whole-core plutonium mass in kilograms during Cycle 1.

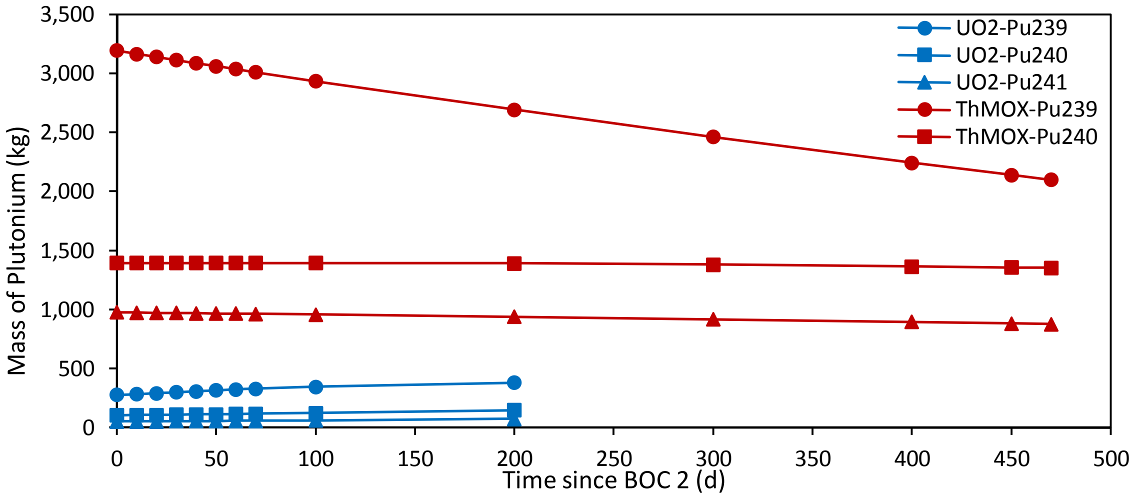

Fig. 10. Whole-core plutonium mass in kilograms during Cycle 2.

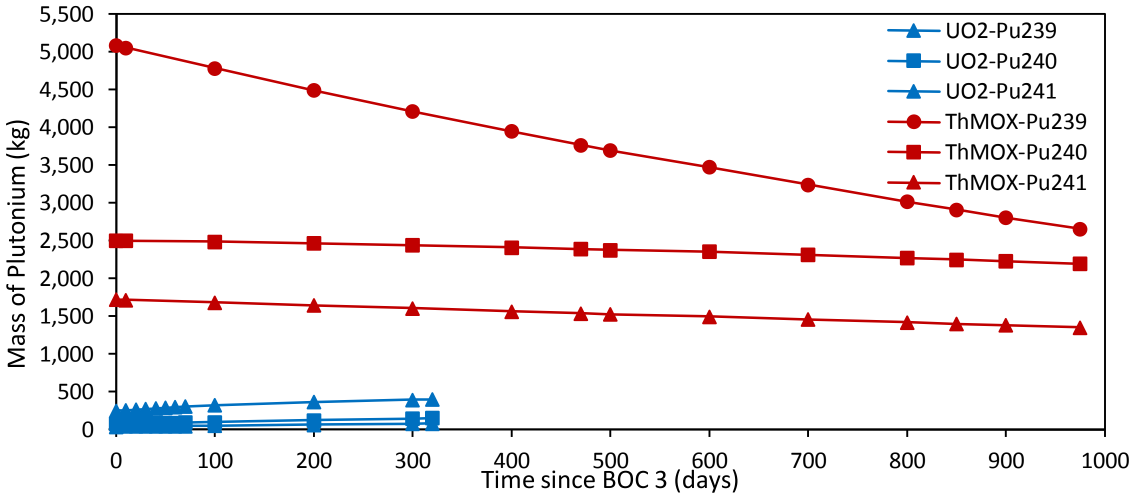

Fig. 11. Whole-core plutonium mass in kilograms during Cycle 3.

assemblies produced almost enough plutonium to completely negate the loss of plutonium in the ThMOX assemblies, which comprised one-third of the core. To maximize plutonium destruction during Cycle 2 without exceeding the BOC excess reactivity of the UO_2 configuration, an additional one-third of the UO_2 assemblies were replaced with ThMOX assemblies and the amount of PuO_2 was increased from 5.5% to 15.8% as described in Section 4.2.

With an additional 2,465 kg of ^{239}Pu present in the ThMOX configuration at BOC 2, the net loss of ^{239}Pu during Cycle 2 was a more substantial 1,094 kg (34% of BOC mass). For Cycle 3, the plutonium content of the fresh ThMOX fuel was further increased to 19.2% PuO_2 to maximize plutonium destruction while maintaining the UO2 configuration's BOC excess reactivity, and all but one UO_2 assembly was replaced with ThMOX. It is no surprise, therefore, that the net loss of ^{239}Pu increased to 2,430 kg (48% of BOC mass).

At the end of Cycle 3, the UO_2 configuration had produced 649 kg of ^{239}Pu, while the ThMOX configuration netted 3,541 kg of ^{239}Pu destroyed. However, the ^{239}Pu destroyed by the ThMOX configuration must be balanced with the 1,188 kg of ^{233}U it produced. In Figure 12, the cumulative production of ^{233}U is plotted.

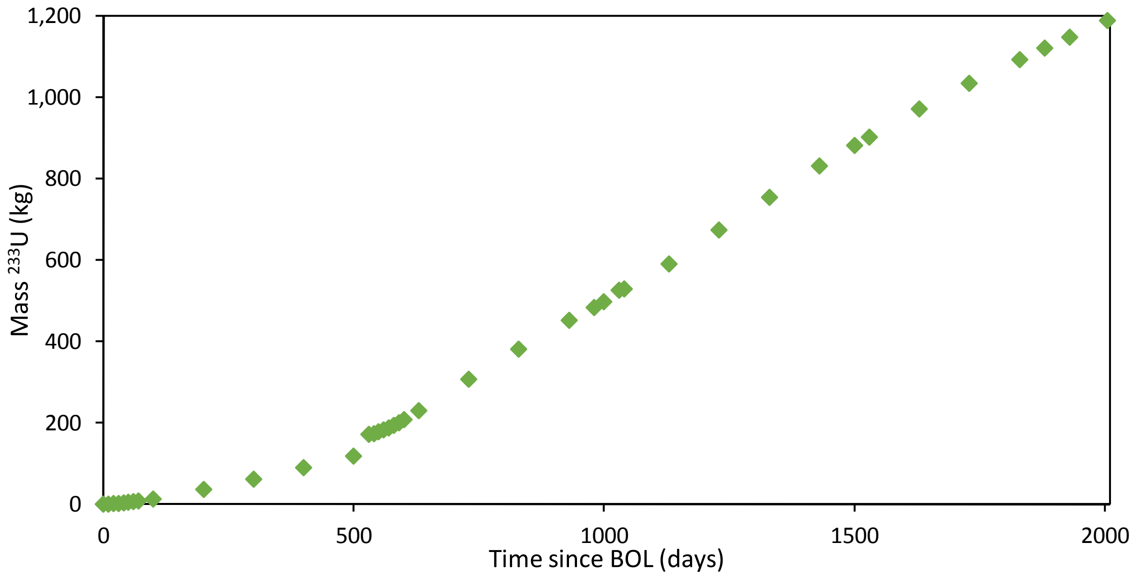

Fig. 12. Lifetime ^{233}U production of the ThMOX configuration.

Table 6. Total discharge activity of thrice-burned, Group 1 Assemblies at EOC 3.

		UO_2		ThMOX	
Material	No. of Assys	Total Activity (Ci)	Activity per Assy (Ci)	Total Activity (Ci)	Activity per Assy (Ci)
13	4	1.138E+08	2.845E+07	8.218E+07	2.055E+07
15	4	1.181E+08	2.953E+07	8.934E+07	2.234E+07
17	4	1.247E+08	3.117E+07	1.230E+08	3.074E+07
22	4	1.162E+08	2.904E+07	8.501E+07	2.125E+07
24	8	2.098E+08	2.623E+07	1.666E+08	2.082E+07
26	8	2.340E+08	2.926E+07	2.073E+08	2.591E+07
33	4	1.140E+08	2.851E+07	8.005E+07	2.001E+07
35	8	2.173E+08	2.717E+07	1.804E+08	2.255E+07
37	8	2.397E+08	2.996E+07	2.367E+08	2.958E+07
44	4	1.172E+08	2.929E+07	9.055E+07	2.264E+07
46	8	2.431E+08	3.039E+07	2.243E+08	2.804E+07

Of course, any fissile material remaining in a used fuel assembly would be well protected by the highly radioactive material with which it resides. Table 6 shows that the discharge activity of the thrice-burned fuel from the ThMOX configuration, while less than that of the UO_2 configuration, is sufficient to deter diversion.

6. Fission Product Poisons

In addition to monitoring fissile isotope mass, it is also prudent to monitor the buildup of fission product poisons (FPP). The FPP of greatest concern is ^{135}Xe; its lifetime mass in each configuration is shown in Figure 13. By Cycle 3 the equilibrium concentration of ^{135}Xe is much higher for the ThMOX configuration than the UO_2 configuration. Two factors contribute to this difference: first, the amount of fissile material is much higher in the ThMOX configuration; second, the fission yield of ^{135}Xe from ^{239}Pu (0.0105) is several times higher than that from ^{235}U (0.00237) [11]. The primary impact lies with an unplanned shutdown: potentially dozens of additional hours would be required to accommodate the decay of the additional ^{135}Xe present in the ThMOX configuration.

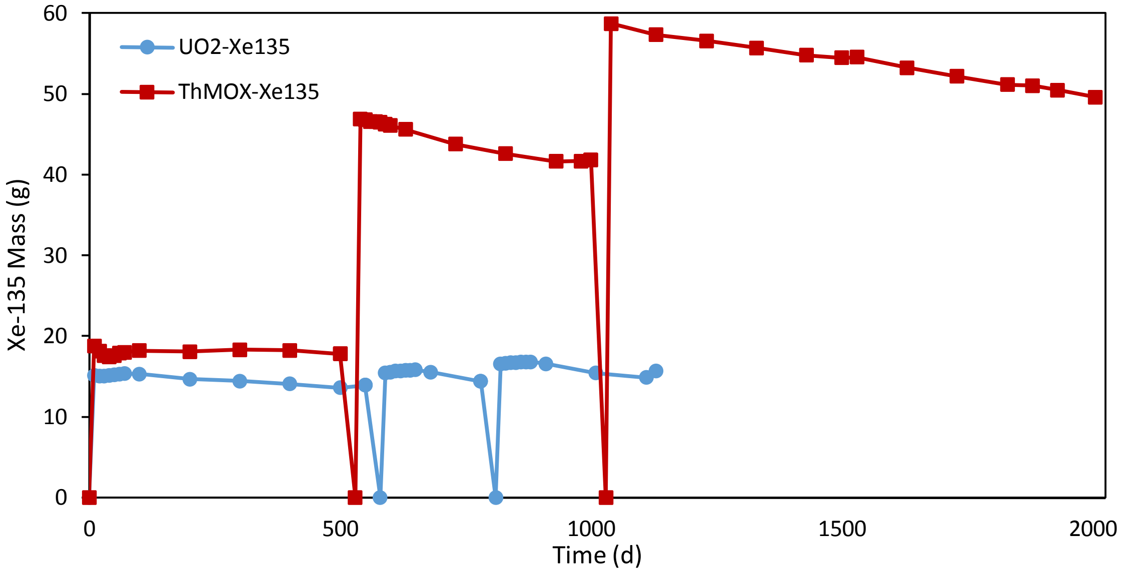

Fig. 13. Lifetime whole-core mass of ^{135}Xe for both the UO$_2$ and ThMOX configurations.

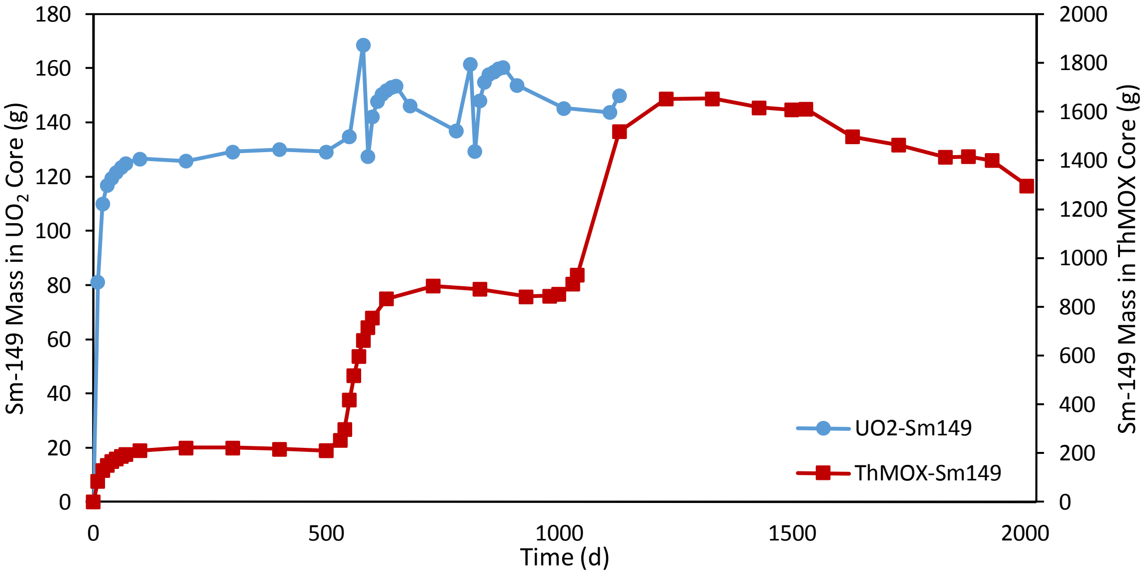

Fig. 14. Lifetime whole-core mass of ^{149}Sm for both the UO$_2$ and ThMOX configurations. The ThMOX configuration's ^{149}Sm concentration is plotted on the secondary axis.

The other FPP worth monitoring is ^{149}Sm. Its lifetime whole-core mass for each configuration is plotted in Figure 14. Much like ^{135}Xe, the equilibrium concentration of ^{149}Sm is much higher for the ThMOX configuration. However, the difference in ^{149}Sm concentration is caused solely by the difference in fissile content, as the fission yield from ^{239}Pu (0.0121) is virtually identical to that of ^{235}U (0.01071) [11]. The additional ^{149}Sm mass present in the ThMOX configuration has the potential to shorten the lifetime of the fuel. If an unplanned shutdown occurs and there is too little excess reactivity to overcome the negative reactivity represented by the mass of ^{149}Sm, the reactor must be refueled. With so much more ^{149}Sm present, a cycle-ending unplanned shutdown could occur earlier – reducing total burnup.

7. Nuclear Hot Channel Factors

There are strict regulatory requirements concerning flux and power distributions in power reactors. Likewise, to ensure that there is no risk of fuel melting, the fuel centerline temperature must be kept below the melting temperature of the fuel. This requirement is met by ensuring the critical heat flux is never reached. In order to find the critical heat flux, two hot channel factors are required: the nuclear axial hot channel factor ($\mathrm{F_Z^N}$) and the enthalpy rise hot channel factor ($\mathrm{F_{\Delta h}}$) as seen in Equation 1.

$$q_c'' = q_{av}''\, F_Z^N\, F_{\Delta h} \tag{1}$$

$\mathrm{F_Z^N}$ is defined as the ratio of the maximum heat flux in the hot channel to the average heat flux in the hot channel (see Equation 2).

$$F_Z^N = \frac{Estimated\ maximum\ heat\ flux\ in\ hot\ channel}{Mean\ heat\ flux\ in\ hot\ channel} \tag{2}$$

$\mathrm{F_{\Delta h}}$ is the enthalpy rise in the hottest channel over the enthalpy rise in the average channel [12]. $\mathrm{F_{\Delta h}}$ accounts for both the radial nuclear hot channel factor ($\mathrm{F_R^N}$) and the engineering enthalpy rise hot channel factor ($\mathrm{F_{\Delta h}^E}$):

$$F_{\Delta h} = F_R^N F_{\Delta h}^E \tag{3}$$

The radial nuclear hot channel factor ($\mathrm{F_R^N}$) is the mean heat flux in the hot channel over the mean heat flux in the average channel of the core (see Equation 4).

$$F_R^N = \frac{Mean\ heat\ flux\ in\ hot\ channel}{Mean\ heat\ flux\ in\ average\ channel\ of\ the\ core} \tag{4}$$

However, one would be required to perform a detailed thermal hydraulic analysis of the core to determine the engineering enthalpy rise hot channel factor which would include the core flow subfactor and core mixing subfactor. Additionally, there are fuel fabrication uncertainties associated with the enrichment, density and geometry of the fuel, all of which are accounted for in the engineering hot channel factor, $\mathrm{F_Q^E}$. In the absence of information regarding engineering enthalpy rise hot channel factor ($\mathrm{F_{\Delta h}^E}$) and the engineering hot channel factor ($\mathrm{F_Q^E}$), only nuclear hot channel factors can be compared to assess the relative safety of incorporating Th-MOX fuel into a PWR core. Though calculating the engineering enthalpy rise hot channel factor ($\mathrm{F_{\Delta h}^E}$) was outside the scope of this work, it was possible to estimate the axial and radial nuclear hot channel factors with assembly-level power generation data from the burnup runs and thermal neutron flux tallies performed after the burnup runs were completed.

As stated in Section 3, an MCNP burnup run outputs the fraction of the total power generated by each material. Since a different fuel material was assigned to each assembly necessary given the one-eighth symmetry of a PWR (as seen in Figure 4), the power fraction for each material could be multiplied by the total thermal reactor power (3,411 MW) and the symmetry of the assembly represented by that material (e.g. one-fourth for material 22, one-eighth for material 23) to determine the power produced by each assembly for each time step. Then, the assembly with the maximum thermal output was found. The power produced by this assembly was divided by the average power produced per assembly for its time step to generate a whole-core approximation of $\mathrm{F_R^N}$ as seen in Equation 5. The results of the calculations for each time step for both configurations are plotted in Figure 15. These results were also used to create a heat map of each time step's power distribution with each assembly color coded according to the maximum and minimum power producer across all time steps for each configuration. Examples of these plots are provided in Figure 16 at the time step with the highest $[F_R^N]_{core}$ for each configuration.

$$[F_R^N]_{core} = \frac{P_{max}}{P_{average}} \tag{5}$$

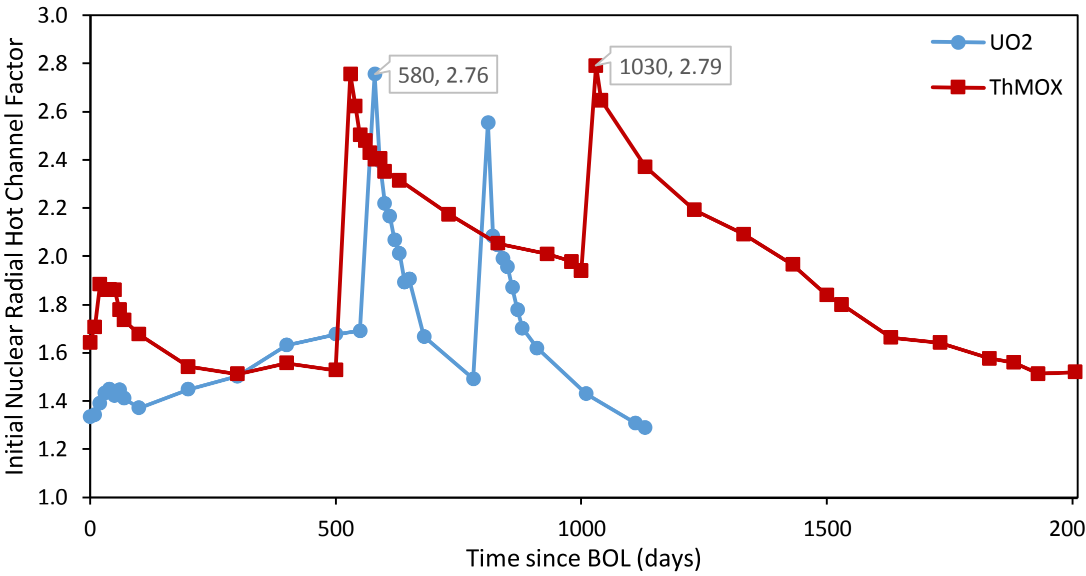

Fig. 15. Whole-core approximation of the nuclear radial hot channel factor at each time step for both the UO_2 and ThMOX configurations. The worst-case scenario for each configuration has been flagged.

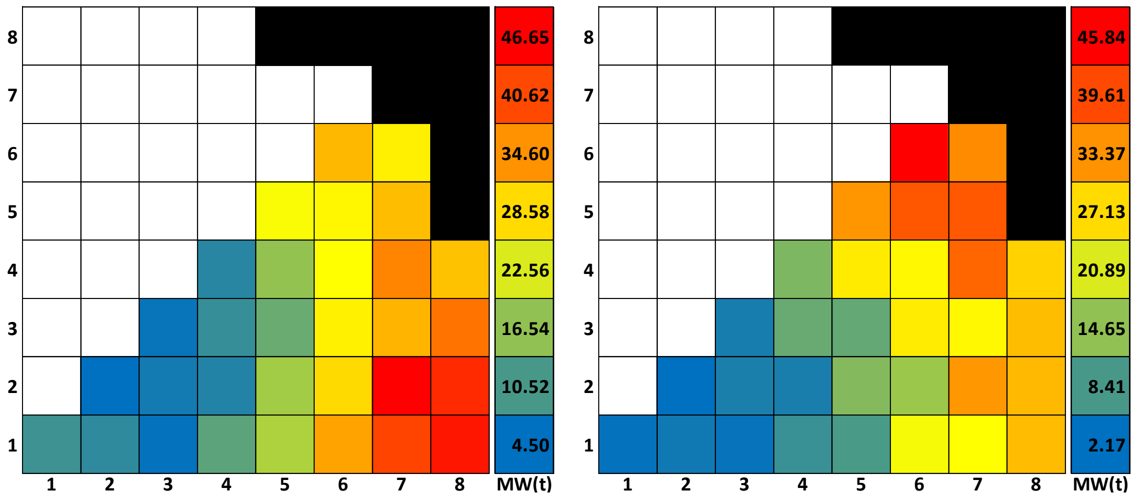

UO_2 BOC 2 ThMOX BOC 3

Fig. 16. Assembly-by-assembly power distribution for each configuration at the time step with the highest whole-core approximation of the radial nuclear hot channel factor. Colors are scaled from the lowest value across all three cycles to the highest value across all three cycles.

For the UO_2 configuration, the initial approximation for F_R^N peaks at the beginning of Cycle 2, while it peaks at the beginning of Cycle 3 for the ThMOX configuration. The highest power producing assemblies are Assembly 27 and Assembly 66, respectively. If the nuclear hot channel factors are acceptable for these assemblies at these time steps – the worst case scenarios – then it can be reasoned that they will be acceptable for all other assemblies at all other time steps. Therefore, each of these assemblies were examined in greater detail.

A pin-by-pin thermal neutron flux tally in seventeen vertical sections was performed on UO_2 BOC 2 Assembly 27 and ThMOX BOC 3 Assembly 66. Water-filled channels were ignored. Thermal neutron flux can be used to approximate heat flux in a thermal reactor because the rate of fission and hence energy production is directly related to the thermal neutron population. However, a portion of a thermal reactor's power is produced by fast fission (typically about 8%), which will introduce some error to the nuclear hot channel factor results presented here. The results of this analysis were used to generate seventeen flux maps of each configuration's hottest assembly. Then the results for each pin were summed across all seventeen vertical sections to reveal each configuration's hot channel. These plots are shown in Figure 17. For UO_2 BOC 2 the hot channel is located at (x = 135.3 cm, y = 16.5 cm). For ThMOX BOC 3 the hot channel is located at (x = 101.2 cm, y = 112.6 cm). In both cases the origin is in the center of the core at the bottom of the fuel.

To complete the approximation of the radial nuclear hot channel factor, the initial approximation for F_R^N is multiplied by the ratio of the total flux in the hot channel (ϕ_{HC}^{HA}) divided by the average channel flux in the hot assembly (ϕ_{ave}^{HA}). See Equation 6. The results of these calculations are presented in Table 3.

$$F_R^N \approx \frac{\phi_{HC}^{HA}}{\phi_{ave}^{HA}} [F_R^N]_{core} \tag{6}$$

The results from the thermal neutron flux tallies performed on each configuration's hot assembly were also used to calculate the axial nuclear hot channel factors. No additional simulations were required. In the hot channel, the flux from the vertical section with the highest flux ($\phi_{\text{max}}^{\text{HC}}$) was divided by the average flux in the hot channel ($\phi_{\text{ave}}^{\text{HC}}$) as seen in Equation 7. The results of these calculations are presented in Table 3.

$$F_Z^N \approx \frac{\phi_{max}^{HC}}{\phi_{ave}^{HC}} \tag{7}$$

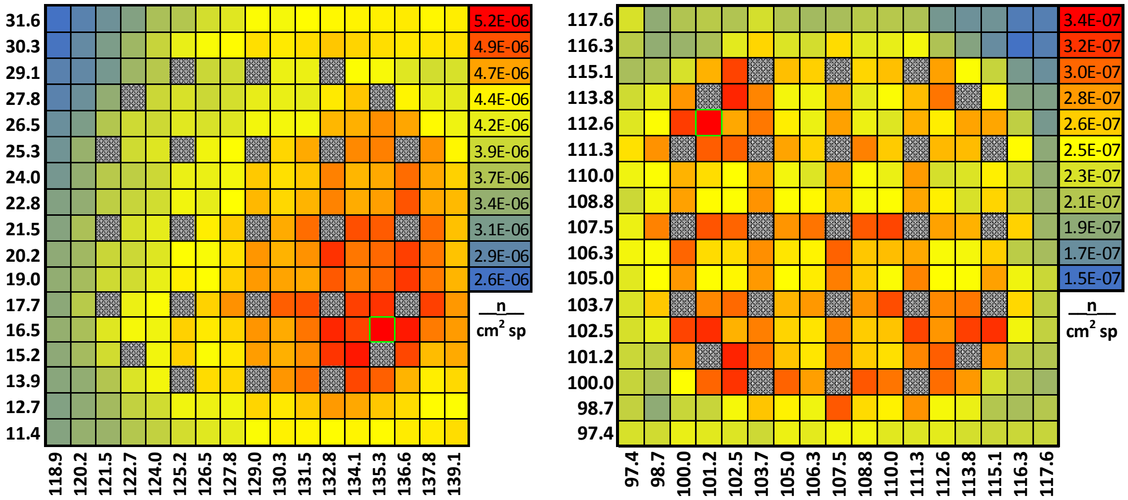

UO₂ BOC 2 Assembly 27 ThMOX BOC 3 Assembly 66

Fig. 17. Pin-by-pin thermal neutron flux distribution for each configuration's hottest assembly at the time step with the highest whole-core approximation of the nuclear radial hot channel factor. The hot channel is bordered in green. Non-fuel channels are shaded gray.

Table 7. Axial and radial nuclear hot channel factors at the time step with the highest whole-core approximation of the radial nuclear hot channel factor for each configuration.

	F_Z^N	F_R^N
UO_2 BOC 2	1.515 ± 0.246	3.430 ± 0.066
ThMOX BOC 3	1.839 ± 0.951	3.820 ± 0.232

For both the axial and the radial nuclear hot channel factors the ThMOX results are less favorable than the UO_2 results. The difference in F_R^N can be explained by the significant increase in plutonium content made for cycles 2 and 3, which increases the fraction of the power produced in the outer assemblies. Even with the 19.2% PuO_2 assemblies in the core the F_R^N of the worst-case scenario for the ThMOX configuration is only 11% worse than the F_R^N for the UO_2 configuration's worst-case scenario.

The 21% difference in F_Z^N can also be explained mostly by the increase in plutonium composition. There is no axial variation in fuel composition because of approximations necessary for the burnup simulations. However, flux shape changes axially with differences in leakage and power production. With more fuel added to the Group 1 assemblies in the ThMOX configuration (Assembly 66 included), more power will be produced on the core's periphery, and higher axial power peaking will occur. A 21% difference is still within the statistical uncertainty of the simulations, so further investigation might reveal a much smaller difference between each configuration's F_Z^N. In Figure 18, the values used to calculate F_Z^N are plotted for each configuration.

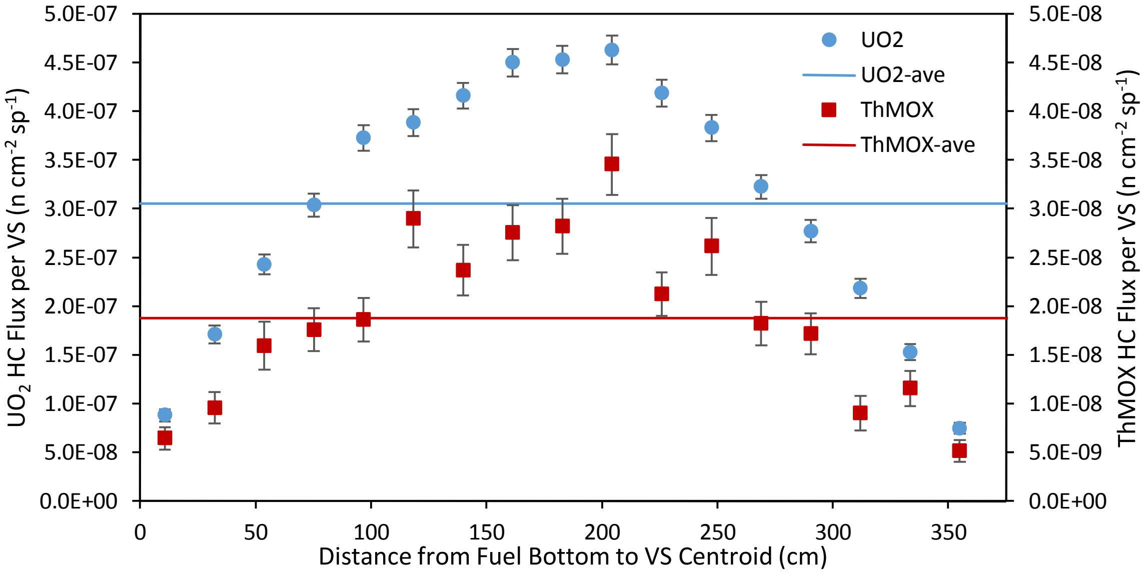

Fig. 18. Flux per vertical section (VS) for each configuration's hot channel (HC). Each configuration's average hot channel flux is also included as a horizontal line. These values were used to calculate the axial nuclear hot channel factor. The ThMOX configuration's values are plotted on the secondary axis.

8. Delayed Neutron Fraction

Since the delayed neutron fraction (β_{eff}) influences a reactor's controllability, β_{eff} is an important parameter to investigate. Two KCODE simulations are necessary to determine β_{eff} with MCNP. In the first simulation, both delayed neutrons and prompt neutrons are generated and tracked yielding the total multiplication factor (k). In the second simulation, only prompt neutrons were generated and tracked, yielding the prompt multiplication factor (k_p). Using the results of these two simulations the effective delayed neutron fraction could be approximated with Equation 8 [13]:

$$\beta_{eff} \cong 1 - \frac{k_p}{k} \tag{8}$$

KCODE simulations were performed at each time step of interest (BOC, POC, EOC) for both configurations. Results are presented in Table 7. At every time step the ThMOX configuration's β_{eff} is less than the UO_2 configuration's, with the greatest difference occurring at BOC 3. These results are not surprising as there is a great deal more plutonium in the ThMOX configuration, and the β_{eff} of ^{239}Pu (0.0021) is lower than that of ^{235}U (0.0065) [14]. Greater care will have to be taken during the operation of a reactor fueled with ThMOX as it is likely to be more difficult to control unless the lower β_{eff} of the ThMOX configuration is balanced by some other difference. For instance, positive reactivity would have to be added more slowly to ensure reactor safety margins are maintained.

Table 8. Delayed neutron fraction at times of interest for both configurations.

	UO_2	ThMOX
BOC 1	7.288E-03 ± 1.630E-06	4.325E-03 ± 1.274E-06
POC 1	6.607E-03 ± 1.456E-06	5.888E-03 ± 1.417E-06
EOC 1	5.105E-03 ± 2.881E-07	4.614E-03 ± 2.642E-07
BOC 2	6.320E-03 ± 3.985E-07	3.750E-03 ± 1.039E-06
EOC 2	5.327E-03 ± 1.507E-06	4.073E-03 ± 1.152E-06
BOC 3	6.177E-03 ± 1.510E-06	3.324E-03 ± 8.919E-07
EOC 3	4.457E-03 ± 1.226E-06	3.603E-03 ± 9.969E-07

9. Temperature Coefficients

Another important reactor safety parameter is the temperature coefficient (α_T), which quantifies the effects of temperature changes on reactivity. Equation 9 shows how the temperature coefficient is calculated [15].

$$\alpha_T = \frac{1}{k^2}\frac{dk}{dT} \tag{9}$$

Separate components such as the moderator and the fuel have their own temperature coefficients. This study considered the moderator temperature coefficient (MTC) and the fuel temperature coefficient (FTC).

Finding both of the temperature coefficients for one of the configurations at one of the time steps required three MCNP KCODE simulations. The first simulation was performed with operating temperature cross sections for moderator and fuel (600 K, typically the 71c ENDF-VII libraries). Water density was 0.711 g cm^{-3}, and the configuration's critical boron concentration was used. The second simulation used operating temperature (600 K) cross sections for the fuel, and room temperature cross sections and density (1 g cm^{-3}) for the moderator (the 70c ENDF-VII libraries at 293 K). Increasing the mass density of the moderator automatically increased the number density of boron in the moderator. Finally, a simulation was performed with room temperature fuel and room temperature moderator.

The MTC is calculated from the results of the first simulation (operating temperature moderator and operating temperature fuel) and the third simulation (room temperature moderator and room temperature fuel). The FTC is calculated from the results of the second simulation (room temperature moderator and operating temperature fuel) and the third simulation (room temperature moderator and room temperature fuel).

9.1. Moderator Temperature Coefficient

Each configuration's MTC results for all time steps of interest are presented in Table 9. Three of the MTC results are positive. Typically, a negative MTC is required by the Nuclear Regulatory Commission (NRC). However, at BOL the NRC does allow most plants to have a slightly positive MTC. For the Callaway Plant an MTC of up to 5 pcm/ºF is allowed [16]. Under this exception the positive MTC value for UO_2 BOC 1 is not only allowed, but expected. However, the positive MTC values both configurations exhibit at

POC 1 (40 days after BOC) do not meet the NRC's criteria for exception – namely, operating at less than 100% of rated thermal power (RTP).

Table 9. Moderator temperature coefficient at each time step of interest for both configurations.

	UO_2 (pcm/°F)	ThMOX (pcm/°F)
BOC 1	2.743 ± 0.00024	-6.004 ± 0.00052
POC 1	15.311 ± 0.00513	3.453 ± 0.00104
EOC 1	-25.409 ± 0.00440	-25.467 ± 0.00849
BOC 2	-15.208 ± 0.00553	-22.564 ± 0.00889
EOC 2	-32.487 ± 0.01078	-35.736 ± 0.01279
BOC 3	-4.992 ± 0.00183	-2.325 ± 0.00098
EOC 3	-30.324 ± 0.01007	-32.805 ± 0.01093

It should not be possible for either configuration to produce a positive MTC value at any point other than BOL. The buildup of FPP should prevent this; and before sufficient FPP concentration has been achieved the burnable absorbers should prevent it. The most likely cause for the positive MTC values at POC 1 is the omission of a power ramp at BOC. When real-world PWRs are brought online, control assemblies are slowly withdrawn over the course of several days, allowing the system to gradually warm up to operating temperature as it approaches full power. During the burnup simulation both configurations were run at 100% of RTP, which accelerated the burnout of the burnable absorber rods. Since the BAs burned out faster than designed, the systems were unable to maintain a negative MTC.

At all time steps except BOC 3, the MTC of the ThMOX configuration is lower than that of the UO_2 configuration. This indicates that even with the positive MTC values at POC 1, the ThMOX configuration should not be precluded from consideration. Furthermore, it is possible that the more favorable MTC values of the ThMOX configuration could ameliorate the controllability issues suggested by its lower delayed neutron fractions. However, since the favorability of the ThMOX configuration's MTC is lost after the fissile content is substantially increased for Cycle 3 the decision to increase fissile content – or, at the very least, the magnitude of the increase – should be reevaluated.

9.2. Fuel Temperature Coefficient

For various safety reasons NRC pays particular attention to the FTC [17]. These values are reported in Table 10 for both configurations at all time steps of interest. First, it is important to note that all values for both configurations are negative. Second, at every time step the FTC of the ThMOX configuration is more negative than that of the UO_2 configuration. This is likely caused by greater thermal conductivity of the ThMOX fuel. Initial experimental data for fuel designed by Thor Energy suggests as much [27]. At any rate, the improved FTC could further reduce the impact on controllability of the ThMOX configuration's lower β_{eff} values.

Table 10. Fuel temperature coefficient at each time step of interest for both configurations.

	UO_2 (pcm/^oF)	ThMOX (pcm/^oF)
BOC 1	-4.546 ± 0.00039	-6.499 ± 0.00056
POC 1	-4.486 ± 0.00152	-6.132 ± 0.00186
EOC 1	-5.443 ± 0.00093	-6.223 ± 0.00205
BOC 2	-4.391 ± 0.00156	-7.130 ± 0.00282
EOC 2	-4.478 ± 0.00144	-7.235 ± 0.00254
BOC 3	-4.530 ± 0.00169	-6.527 ± 0.00283
EOC 3	-5.534 ± 0.00181	-7.596 ± 0.00249

10. Shutdown Margin

A safety analysis of any reactor will invariably include determination of the control rod worth and shutdown margins. In order to comply with regulatory requirements, the shutdown margin the ThMOX configuration should be comparable to that of the UO_2 configuration and must be greater than 1300 pcm as prescribed by the NRC. A reactor core's reactivity is the algebraic sum of many contributing factors, and so its control rod worth (ρ_{rods}) depends on many factors as well. To calculate ρ_{rods} two MCNP simulations were necessary: one with all control assemblies (CA) fully inserted (k_{in}) according to Figure 3, and another with all CAs fully withdrawn (k_{out}). Then finding ρ_{rods} is simply a matter of subtracting k_{in} from k_{out} as in Equation 10:

$$\rho_{rods} = k_{out} - k_{in} \tag{10}$$

Shutdown margin (SDM) is defined by the NRC as the instantaneous amount of reactivity by which the reactor is subcritical – or would be subcritical from its present condition – assuming all control rods are fully inserted except the highest worth rod (HWR), which is fully withdrawn [18]. Shutdown margin can be represented algebraically by Equation 11:

$$SDM = \rho_{rods} - \rho_{HWR} \tag{11}$$

It is necessary, therefore, to determine which assembly is the HWR. To find the HWR with MCNP a KCODE simulation is performed with all assemblies except the CA of interest inserted ($\mathrm{k}_{\mathrm{out}}^{\mathrm{i}}$). From this, k_{in} is subtracted to find the worth of that rod ($\rho_{\mathrm{rod}}^{\mathrm{i}}$) as in Equation 12:

$$\rho_{rod}^{i} = k_{out}^{i} - k_{in} \tag{12}$$

Fortunately, one can capitalize on the symmetry of a PWR, omitting most CAs from the analysis. The only CAs considered for this work were those above Row 8 and to the right of Column H (inclusive) as defined in Figure 3. The results of these calculations for both configurations at the time steps of interest are collected in Table 11.

Table 11. Shutdown margin and highest worth rod at each time step of interest for both configurations.

	UO_2		ThMOX	
	HWR	SDM (pcm)	HWR	SDM (pcm)
BOC 1	J6	8804 ± 40	J6	8134 ± 47
POC 1	J6	8297 ± 40	J6	7559 ± 39
EOC 1	H8	6701 ± 33	L4	6827 ± 33
BOC 2	H2	4407 ± 40	N8	4281 ± 41
EOC 2	H2	5975 ± 35	H2	4314 ± 37
BOC 3	N4	7275 ± 41	N4	3971 ± 43
EOC 3	H2	6958 ± 34	H4	4608 ± 35

While the ThMOX configuration’s SDMs are lower than those of the UO_2 configuration for all time steps of interest, they all substantially exceed the NRC limit of 1,300 pcm [18].

11. Conclusions

It is feasible not only to incorporate ThMOX fuel into a conventional PWR, but also to replace the entire core with ThMOX assemblies. The work presented here supports this statement – with a few caveats.

The results produced for this work relied on comparing a conventional UO_2-fueled PWR configuration to a novel ThMOX configuration. At BOL the UO_2 configuration was stocked with 3.1%, 2.6%, and 2.1% enriched fuel, while in the ThMOX configuration the 3.1% UO_2 fuel was replaced 5.5% PuO_2 ThMOX fuel. Burnable absorbers were distributed throughout, and Ag-In-Cd CAs and soluble boron were the available control materials.

Both configurations were run through three cycles of burnup simulations while fresh fuel was added and used fuel was either shuffled or replaced. The fresh fuel incorporated into the UO_2 configuration for Cycles 2 and 3 was kept at 3.1% enrichment, resulting in cycle lengths of 550 days, 200 days, and 320 days, respectively. In an effort to destroy as much plutonium as safely possible with the ThMOX configuration, the plutonium content of the fresh fuel was increased to 15.8% PuO_2 for Cycle 2 and 19.2% PuO_2 for Cycle 3 to maximize plutonium destruction without exceeding the BOC excess reactivity of the UO_2 configuration. The increase in fissile content resulted in a substantially longer third cycle: from 500 days for Cycle 1 and 470 days for Cycle 2 to 975 days for Cycle 3.

The increase in the plutonium content of the ThMOX configuration’s fresh fuel, coupled with the shuffling out of used UO_2 fuel, created the necessary conditions for significant plutonium destruction. While Cycle 1 saw a net destruction of only 17 kg of ^{239}Pu, the ThMOX configuration destroyed 1,094 kg of ^{239}Pu during Cycle 2 and 2,430 kg during Cycle 3 for a total net destruction of 3,541 kg across all three cycles. This means the ThMOX configuration could destroy all of the ^{239}Pu produced by three cycles of operation (649 kg) for more than five UO_2-fueled PWRs. However, the 1,188 kg of fissile

^{233}U that were produced by the ThMOX configuration during three cycles of operation must not be forgotten. Of course, the highly radioactive fission products which accompany both the ^{233}U that was produced and the ^{239}Pu that was not destroyed would provide a significant deterrent for diversion.

The first notable caveat to the ThMOX configuration is the sizeable increase in fission product poison concentration. The masses of both ^{135}Xe and ^{149}Sm in the ThMOX configuration dramatically outpaced those in the UO_2 configuration. The increase in ^{135}Xe mass would increase the duration of an unplanned outage. And the increase in ^{149}Sm mass could increase the likelihood that an unplanned outage would force a refueling.

Axial and radial nuclear hot channel factor results are also less favorable for the ThMOX configuration. However, neither the 21% increase in F_N^Z nor the 11% increase in F_N^R preclude it from consideration. Furthermore, a thermal hydraulic analysis is required to fully understand the impact of the fuel change.

The delayed neutron fraction results are another area of concern. At all time steps of interest the ThMOX configuration's β_{eff} is lower than that of the UO_2 configuration. A lower β_{eff} could make the reactor more difficult to control. However, all fuel temperature coefficients for the ThMOX configuration are lower than those of the UO_2 configuration, and (with the exception of BOC 3) the ThMOX configuration's moderator temperature results are also more favorable. The more favorable temperature coefficients could ameliorate the impact of β_{eff} on the controllability of the ThMOX configuration, however, they also call into question the magnitude of the increase in plutonium content for Cycle 3.

And finally, though the ThMOX configuration's shutdown margins were lower than those of the UO_2 configuration, they were well above the NRC-required 1,300 pcm.

It is important to reiterate that all analyses presented here were performed without any thermal fluid considerations. However, because of the identical core and assembly geometry, the assumption that the two cores will exhibit similar thermal fluid behavior during normal and off-normal operating conditions makes these comparisons relevant. Nevertheless, it would be beneficial to couple a detailed thermal analysis with this study to provide comprehensive assessments of all safety parameters. Additionally, an optimization of the ThMOX configuration for plutonium destruction would be interesting. And an improvement to the burnup procedure to include more accurate modeling of the initial power ramp up would further refine the results.

References

[1] B.S. Van Gosen, V.S. Gillerman, T.J. Armbrustmacher. "Thorium Deposits of the United States—Energy Resources for the Future?" U.S. Geological Survey Circular 1336. 2009.

[2] E.M. Baum, H.D. Knox, T.R. Miller. "Nuclides and Isotopes: Chart of Nuclides, 16th Ed." Lockheed Martin Distribution Services. 2002.

[3] F. Sokolov, K. Fukuda, H.P. Nawada. "Thorium Fuel Cycle – Potential Benefits and Challenges" IAEA-TECDOC-1450. IAEA. Vienna. 2005.

[4] "Role of Thorium to Supplement Fuel Cycles of Future Nuclear Energy Systems" IAEA Nuclear Energy Series No. NF-T-2.4. IAEA. Vienna. 2012.

[5] S. Peggs, W. Horak, T. Roser, et al. "Thorium Energy Futures" Proceedings of IPAC2012. New Orleans. 2012.

[6] K. Hesketh, A. Worrall. "The Thorium Fuel Cycle: An independent assessment by the UK National Nuclear Laboratory" National Nuclear Laboratory Position Paper. 2010.

[7] L.P. Tucker, A. Alajo, S. Usman. "Thorium-based mixed oxide fuel in a pressurized water reactor: A beginning of life feasibility analysis with MCNP" Annals of Nuclear Energy, 76, 323-334. 2015.

[8] J.T. Goorley, M.R. James, T.E. Booth, et al. "Initial MCNP6 Release Overview MCNP6 Version 1.0" Los Alamos National Laboratory report, LA-UR-13-22934. 2013.

[9] E. Shwageraus, P. Hejzlar, M.S. Kazimi. "Use of Thorium for Transmutation of Plutonium and Minor Actinides in PWRs" Nucl. Tech., 147, 53-68. 2004.

[10] J.S. Hendricks, G.W. McKinney, M.L. Fensin, et al. "MCNPX 2.6.0 Extensions" Los Alamos National Laboratory report, LA-UR-08-2216. 2008.

[11] M.E. Meek, B.F. Rider. "Compilation of Fission Product Yields" General Electric Company Report NEDO-12154. 1972.

[12] J. Weisman. *Elements of Nuclear Reactor Design*. 2nd Ed. Robert E. Kriegler Publishing Company. Malabar, Florida. 1983.

[13] S. Michalek, J. Hascik, G. Farkas. "MCNP5 Delayed Neutron Fraction (β_{eff}) Calculation in Training Reactor VR-1" Jour. of Elec. Eng., 59, 221-224. 2008.

[14] J.R. Lamarsh, A.J. Baratta. *Introduction to Nuclear Engineering*. 3rd Ed. Prentice Hall, Inc. Upper Saddle River, New Jersey. 2001.

[15] J.R. Lamarsh. *Introduction to Nuclear Reactor Theory*. American Nuclear Society, Inc. LaGrange Park, Ill. 2002.

[16] "Callaway cycle 15 core operating limits report (Revision 1)" ULNRC-05335. U.S. Nuclear Regulatory Commission. 28 September 2006.

[17] "Inspection Procedure 61708: Isothermal and moderator temperature coefficient determinations" NRC Inspection Manual. 11 October 1985.

[18] Union Electric Company. "Callaway Plant Unit No. 1 Facility Operating License" Docket No. STN 50-483, U.S. Nuclear Regulatory Commission, License No. NPF-30, Amendment No. 120. 13 February 1998.

[19] S. Mittag, S. Kliem. "Burning plutonium and minimizing waste in existing PWRs" Annals of Nuclear Energy, 38, 98-102. 2011.

[20] K.I. Bjork, V. Fhager, C. Demaziere. "Comparison of thorium-based fuels with different fissile components in existing boiling water reactors" Progress in Nuclear Energy, 53, 618-625. 2011.

[21] H.R. Trellue, C.G. Bathke, P. Sadasivan. "Neutronics and material attractiveness for PWR thorium systems using monte carlo techniques" Progress in Nuclear Energy, 53, 698-707. 2011.

[22] E. Fridman, S. Kliem. "Pu recycling in a full Th-MOX PWR core. Part I: Steady state analysis" Nuclear Engineering and Design, 241, 193-202. 2011.

[23] K.I. Bjork, C.W. Lau, H. Nylen, U. Sandberg. "Study of thorium-plutonium fuel for possible operating cycle extension in PWRs" Science and Technology of Nuclear Installations. 2013.

[24] K.D. Weaver, J.S. Herring. "Performance of thorium-based mixed oxide fuels for the consumption of plutonium in current and advanced reactors" International Congress on Advanced Nuclear Power Plants 2002. Hollywood, FL. 2002.

[25] D. Baldova, E. Fridman, E. Shwageraus. “High Conversion Th-U233 fuel for current generation of PWRs: Part III – Fuel availability and utilization considerations” Annals of Nuclear Energy, 87, 517-526. 2016.

[26] M. Todosow, G. Raitses. “Thorium based fuel cycle options for PWRs” Proceedings of ICAPP ’10. San Diego. 13-17 June 2010.

[27] K.I. Bjork, S.S. Drera, J.F. Kelly, et al. “Commercial thorium fuel manufacture and irradiation: Testing (Th, Pu)O_2 and (Th, U)O_2 in the ‘Seven-Thirty’ program” Annals of Nuclear Energy, 75, 79-86. 2015.

SECTION

2. CONCLUSIONS

The primary objective of this work was to investigate the feasibility of incorporating a Th-Pu MOX fuel into the fuel supply of a conventional PWR for plutonium disposition. In pursuit of this objective, it was helpful to investigate the dead-time of two neutron detectors and identify the best candidate isotopes for online burnup analysis and spent fuel monitoring of MOX fuel.

Both non-paralyzing and paralyzing dead-time calculations were performed for the Portable Spectroscopic Fast Neutron Probe (N-Probe), which can be used for spent fuel interrogation. The dead-time for another neutron detector (^{3}He) was also calculated using measurements collected in a subcritical assembly. An MCNP model of the subcritical assembly experiment was developed for comparison. The calculations relied on a combination of the attenuation law and paralyzing and non-paralyzing dead-time models. The N-Probe contains an NE-213 liquid scintillator detector and a spherical ^{3}He detector. For the spherical ^{3}He fast neutron probe, non-paralyzing dead-time values were higher than paralyzing dead-time values, as expected. Average paralyzing dead-time was calculated to be 101.2 µs and non-paralyzing dead-time was calculated to be 254.8 µs for the N-Probe liquid scintillator detector. A Canberra ^{3}He neutron detector's dead-time was estimated using a combination of subcritical assembly measurements and MCNP simulations. The paralyzing dead-time was estimated to be 14.5 µs, and the non-paralyzing dead-time was estimated to be 16.4 µs for ^{3}He gas filled detector.

A multitude of fission products identified previously identified with ORIGEN ARP computer simulations were scrutinized for their suitability for burnup and spent fuel analysis. The best candidate isotopes were identified by investigating half-life, fission yield, branching ratios, production modes, thermal neutron absorption cross section, and fuel matrix diffusivity. ^{132}I and ^{97}Nb were identified as good isotope candidates for on-line burnup analysis. ^{132}I is also a good candidate for plutonium/uranium discrimination due to the large difference between its fission yields. Cesium isotopes appear to be the best choices for interim storage monitoring. For long-term storage monitoring ^{94}Nb is the most attractive candidate. It has a low diffusion rate of about 10 to 11 cm^2/s, an almost zero neutron absorption cross section (making it burnup history independent), and a gamma yield of 1.44E-09.

After investigating spent fuel monitoring techniques, the feasibility of utilizing ThMOX fuel in a pressurized water reactor was examined under steady-state, beginning of life conditions. With a three-dimensional MCNP model of a Westinghouse-type 17x17 PWR, many possibilities for replacing one-third of the UO_2 assemblies with ThMOX assemblies were considered. The excess reactivity, critical boron concentration, and centerline axial and radial flux profiles for several configurations and compositions of a one-third ThMOX core were compared to a 100% UO_2 core. A blanket-type arrangement of 5.5 wt% PuO_2 was determined to be the best candidate for further analysis. Therefore, this configuration was compared to a 100% UO_2 core using the following parameters: delayed neutron fraction, temperature coefficient, shutdown margin, and axial and radial nuclear hot channel factors.

Following the initial beginning of life analysis, the effect of burnup on the ThMOX configuration was compared to the UO_2 configuration. The safety of the ThMOX configuration was compared to that of the UO_2 configuration at several time steps of interest within each cycle (beginning of cycle, peak excess reactivity of cycle, and end of cycle) with the following metrics: axial and radial nuclear hot channel factors, moderator and fuel temperature coefficients, delayed neutron fraction, and shutdown margin. Additionally, the performance of the ThMOX configuration was assessed by tracking cycle lengths, the amount of plutonium destroyed, and fission product poison concentration. The ThMOX configuration's axial and radial nuclear hot channel factors, and delayed neutron fraction were less favorable than their UO_2 configuration counterparts at all time steps of interest. However, the moderator temperature coefficients, fuel temperature coefficients, and shutdown margins of the ThMOX configuration were more favorable at all time steps of interest. Overall, incorporating ThMOX fuel into the fuel supply for a conventional PWR seems feasible from a neutronics standpoint.

In the future, it would be beneficial to couple a detailed thermal analysis with this study to provide comprehensive assessments of all safety parameters. Additionally, an optimization of the ThMOX configuration for plutonium destruction would be interesting.

And an improvement to the burnup procedure to include more accurate modeling of the initial power ramp up would further refine the results.

VITA

Lucas Tucker was born in Louisville, Kentucky in 1987. He earned a B.S. in Nuclear Engineering from Missouri University of Science and Technology in May 2009, and an M.S. in Nuclear Engineering from the same school in July 2011. He was a U.S. Nuclear Regulatory Commission Fellow and a Missouri S&T Chancellor's Fellow. He interned at Los Alamos National Laboratory in 2012 and Oak Ridge National Laboratory in 2013. He has produced several journal articles and conference presentations. His teaching experience includes Introduction to Nuclear Engineering, Nuclear Radiation Measurements, and Reactor Laboratory I. He is a student member of the American Nuclear Society and Alpha Nu Sigma. In May 2016, he received his Ph.D. in Nuclear Engineering from Missouri University of Science and Technology.